Molecular relaxation of partially deuterated polyisoprene model melts studied by rheology and ^{1}H/^{2}H time domain NMR

Declaration

Hiermit erkläre ich, Jonas Keller, dass ich die vorliegende Doktorarbeit selbstständig im Rahmen der Betreuung durch Prof. Dr. Manfred Wilhelm verfasst habe und keine anderen als die von mir angegebenen Quellen und Hilfsmittel benutzt habe, die wörtlich oder inhaltlich übernommenen Stellen als solche kenntlich gemacht und die Satzung des Karlsruher Instituts für Technologie (KIT) zur Sicherung guter wissenschaftlicher Praxis in der gültigen Fassung beachtet habe.

_____   _____
Ort, Datum   Unterschrift

Zusammenfassung

In der vorliegenden Arbeit werden die molekularen und mechanischen Relaxationsprozesse von Modell-Homopolymerschmelzen untersucht. Hierfür werden definierte Systeme mit unterschiedlichen Topologien und Molekulargewichtsverteilungen aus Polyisopren (PI) und Polystyrol (PS) synthetisiert. Diese Systeme umfassen lineares monodisperses PI, lineares bidisperses PI, definierte PI-Kämme, monodisperse PS-Ringe und definierte PS-Pom-poms. Insbesondere werden sequentiell Deuterium markiertes lineares PI und ein Deuterium markierter PI-Kamm untersucht. Die genannten Modellsysteme werden mit mehreren Techniken charakterisiert, um Relaxationsprozesse in den Polymerschmelzen zu untersuchen. Hierfür wurden oszillatorische Scherrheologie, Fourier Transformations (FT) oszillatorische Scherrheologie, Breitband-dielektrische-Spektroskopie (BDS) und Doppelquanten-Kernspinresonanzspektroskopie (NMR) (in der Zeitdomäne, *time domain* TD) eingesetzt.

Bidispersen Homopolymerschmelzen werden mit oszillatorischer Scherrheologie und FT-oszillatorischer Scherrheologie charakterisiert. Weiterhin wird ein Modell zur Vorhersage der nichtlinearen Antwort von bidispersen Polymerschmelzen vorgestellt. Dafür wird der intrinsische Nichtlinearitätsparameter $^3Q_0(\omega)$ im *medium amplitude oscillatory shear* (MAOS)-Regime nach Fourier Transformation der Schubspannung betrachtet. Ein kürzlich vorgeschlagenes semi-empirisches Modell[1], das die nichtlineare Masterkurve von $^3Q_0(\omega)$ für alle monodispersen Homopolymere vorhersagt und nur von der Anzahl der Verschlaufungen (Z) und der Deborah-Zahl (De) abhängt, wird erweitert, um die nichtlineare Antwort von bidispersen Polymerschmelzen vorherzusagen. Die terminalen Relaxationszeiten für jede Komponente der bidispersen Polymerschmelze werden durch Anpassung von $G^*(\omega)$ mit Hilfe des Rolie-Double-Poly (RDP)-Modells ermittelt. Die beiden Relaxationszeiten für die langkettigen und kurzkettigen Komponenten definieren die Debora-Zahl für die jeweiligen Komponenten in der bidispersen Polymerschmelze. Das vorgeschlagene Modell steht in Übereinstimmung mit den experimentellen Ergebnissen der nichtlinearen Masterkurve $^3Q_0(\omega)$ von der synthetisierten bidispersen Polymerschmelzen. Das Modell wird darüber hinaus auf Kamm-Polymerschmelzen angewendet. Diese ersten Untersuchungen deuten auf die Anwendbarkeit des neu vorgeschlagenen Modells für bidisperse Schmelzen auf Kamm-Polymerschmelzen hin.

Partiell Deuterium markierte Polyisopren-Modellsysteme unterschiedlicher Topologien (linear und Kamm) werden synthetisiert und mittels Doppelquanten-NMR charakterisiert. Da NMR kernspezifisch ist, wird in dieser Untersuchung die Dynamik der jeweils markierten Polymersegmente mittels ^{1}H- und ^{2}H-NMR untersucht. Die experimentellen Ergebnisse an sequentiell markierten linearen Polymeren stehen im Einklang mit dem *tube*-Modell. Die Doppelquanten(DQ)-NMR Untersuchung des Kammes an den ^{1}H- und ^{2}H markierten Segmenten wird vorgestellt und mit der Relaxationszeit aus linearer Rheologie, FT-Rheologie und BDS verglichen.

Für einen Polyisoprenkamm werden die Zeitskalen der beiden Normalmoden, die der Rückgrat- und der Seitenkettenrelaxation entsprechen, unter Verwendung von BDS erhalten. Die Relaxationszeiten stimmen mit denen aus FT-Rheologie und linearer Rheologie überein.

Mit Hilfe einer *hyphenated* Messmethode, die TD-NMR und Rheologie kombiniert (Rheo-NMR), wird die Polymerisationskinetik von Poly(acrylsäure)-Hydrogelen untersucht. Hierfür wird ein T_1-Filter eingesetzt, der die Bestimmung der aktuellen Polymerkonzentration ermöglicht. Dadurch kann der mechanische Schermodul $|G^*|$ mit der Polymerkonzentration c korreliert werdem und ein universeller Zusammenhang in der Form $|G^*(c)| = |G^*_{\max}| \cdot (c/c_{\max})^n$ mit einem Wert von n im Bereich von 2 bis 2.5 gefunden werden.

Abstract

In the presented work, the molecular and mechanical relaxation processes of model homopolymer melts are investigated. To do so, defined topologies and molecular weight distributions of polyisoprene (PI) and polystyrene (PS) are synthesized. These systems include linear monodisperse PI, linear bidisperse PI, defined PI combs, monodisperse PS rings and defined PS pom-poms. In particular, sequentially deuteron labeled linear PI and a deuteron labeled PI comb are investigated. The named modelsystems are characterized by various techniques including oscillatory shear rheology, Fourier transform (FT) oscillatory shear rheology, broadband dielectric spectroscopy (BDS) and double quantum time domain nuclear magnetic resonance (DQ-TD-NMR) spectroscopy to monitor the relaxation processes in the polymer melts.

Bidisperse homopolymer melts are characterized with oscillatory shear rheology and FT oscillatory shear rheology, moreover, a semi-empirical model for the non-linear response is presented. Hereby, the intrinsic non-linearity parameter $^3Q_0(\omega)$ is obtained in the medium amplitude oscillatory shear (MAOS) regime by Fourier transformation of the stress response. A recently proposed semi-empirical model[1] that predicts the non-linear mastercurve of $^3Q_0(\omega)$ for all monodisperse homopolymers which is only dependent on the number of entanglements (Z) and the Deborah number (De) is extended to enable the prediction of bidisperse polymer melts. The terminal relaxation times for each components of the bidispese polymer melt is obtained by fitting $G^*(\omega)$ using the Rolie-Double-Poly (RDP) model. The two relaxation times for the long and short components define the Debora number for the respective components in the polymer melt. The proposed model is in agreement to the experimental results from the non-linear mastercurve $^3Q_0(\omega)$ of the synthesized bidisperse polymer melts. The model is further applied to comb polymer melts, and first investigations suggest the applicability of the newly proposed model for bidisperse melts to comb polymer melts.

Partially deuteron labeled (linear and comb) polyisoprene model systems are synthesized and characterized using DQ NMR. Since NMR is specific to a nucleus, this investigation probes the dynamics of respectively labeled polymer segments, by using ^{1}H-and ^{2}H-NMR. The experimental results on sequentially labeled linear polymers are in line with the tube model. The investigation of the comb is presented and compared to the relaxation time obtained linear rheology, FT-rheology and BDS.

For a polyisoprene comb the time scales for the two normalmodes corresponding to the backbone and the sidechain relaxation are obtained using BDS. The relaxation times are in full agreement with the relaxation time obtained by FT-rheology and linear rheology.

By using a hyphenated technique that combines TD-NMR and rheology (Rheo-NMR) the polymerization kinetics of poly(acrylic acid) hydrogels are investigated. In particular a T_1 filter that allows for

the monitoring of the current polymer concentration is applied. Consequently, the mechanical shear modulus $|G^*|$ is correlated to the polymer concentration c and a universal correlation in the form of $|G^*(c)| = |G^*_{\max}| \cdot (c/c_{\max})^n$ with values of n in the range of 2 to 2.5 are found.

Contents

Abbreviations

a	year
a	tube diameter
a_T	shift factor (rheology)
AAc	acrylic acid
BHT	butylated hydroxytoluene
B_0	magnetic field
BuLi	butyllithium
c	concentration
C1,C2	WLF-parameters
d	distance
δ	chemical shift (NMR)
δ	phase angle (rheology)
D	diffusion coefficient
Đ	dispersity
DC	decree of crosslinking
DQ	double quantum
DSC	differential scanning calorimetry
ϵ	dielectric modulus
E_a	Arrhenius activation energy
FT	Fourier transform
γ	strain (rheology)
γ	gyromagnetic ratio (NMR)
G	G-modulus
h	height
$\vec{h}$	end-to-end vector
η	viscosity

I_1	first harmonic intensity
I_3	third harmonic intensity
l	length
l_K	Kuhn length
$\vec{M}$	magnetization
MALLS	multi-angel LASER light scattering
MMA	methyl methacrylate
MQ	multi quantum
MSF	molecular stress function (rheology)
M_n	number average molecular weight
M_w	weight average molecular weight
M_e	entanglement molecular weight
NMR	nuclear magnetic resonance
N_k	number of Kuhn segments (per polymer chain)
ϕ	volume ratio
PI	polyisoprene
PS	polystyrene
P_n	degree of polymerization
PAAc	poly(acrylic acid)
RDP	Rolie-Double-Poly [-model]
^3Q	non-linearity parameter
$^3Q_0$	intrinsic non-linearity parameter

rf	radio frequency (NMR)
σ	standard deviation
σ	stress (rheology)
SEC	size exclusion chromatograph
T_1	longitudinal relaxation time (NMR)
T_2	transverse relaxation time (NMR)
$T_{1\rho}$	spin lock relaxation time (NMR)
T	temperature
T_{ref}	reference temperature
t	time
t	tonnes
τ	relaxation time
τ_0, τ_d	terminal relaxation time
τ_e	entanglement relaxation time
τ_R	Rouse relaxation time
τ_c	correlation time (NMR)
τ	time (NMR) [within the NMR dimension]
TGA	thermogravimetric analysis
THF	tetrahydrofuran
WLF	Williams-Landel-Ferry
ω	angular frequency
$\omega_L/(2\pi)$	Lamor frequency
Z	number of entanglements
ζ_0	monomeric friction coefficient

1 Introduction

Polymers have an enormous commercial relevance. They combine a high flexibility in mechanical properties, easy processability and cheap prices. In the following sections a brief and universal overview of polymer properties, applications and challenges in field of engineering are presented. For a deeper introduction into the science of polymers the reader is referred to 2 *Fundamentals* (p. 4).

Market of polymers

The world polymer production is $\geq$350 Mt/a[2], which makes it the most important material class by weight after wood, concrete and steel. Polymers are omnipresent in our daily lives. In everyday applications like plastic bags, plastic food packaging or plastic containers. Polymers are present in less apparent utilization like for textiles, which can be fully synthetic fibers or only partially synthetic fibers to enhance the properties of cotton. Additionally, polymers in plastics are often used in combination with other materials, enhancing their properties or improving their processability. In this way, wood particles can be mixed with resin and formed into particle boards that typically coated with paint, which both contains polymers. Steel and metals are often coated to change, *e.g.,* the optical properties or to enhance the corrosion protection. Concrete is mixed with charged polymers to change the flow properties of the raw concrete, enhancing its flow properties, and therefore reducing the encapsulated air after casting. The price of crude polymers is very low, starting at approximately 1 €/kg for polyolefins like polyethylene to several euros per kilogram for materials like polystyrene or polyurethanes.

One key advantage of polymers is their easy processability. Thermoplastic polymers, which are the major share by weight, can be easily be put into form by processes like fiber spinning, film blowing or injection molding. In general the extrusion and processing of polymer can be scaled very well, resulting in low labor cost and cheap products. Hereby, the crude material is normally transferred into a processable state by heating to temperature in the range of typically 200 °C.

Polymer on the molecular level

Polymer are divided into three big classes:

- Thermoplastics are solid at ambient temperatures and in a melt like state at elevated temperature, which enables the easygoing processing.

- Thermosets or resins (German: Duroplast) are plastics, that are cast from an monomeric or oligomeric mixture that is highly cross-linked, resulting in very durable polymer, that is often reinforced by fibers.

- Rubbers are slightly cross-linked materials, that have soft elastic properties. The crude polymer is in a melt like state at ambient temperature, and vulcanized at elevated temperatures, resulting in a form-stable elastic material.

The melt of thermoplastics and the crude material for rubbers are made of very thin and long molecules. The molecules that are the base material of polymer melts are chains that are highly entangled. The physical and mechanical properties are a result of the interaction of polymer chains on the molecular level. These interactions are manifold on the time scale and the length scale, making it a challenging field of research.

Outline

In this thesis, models systems are synthesized and employed to study the interplay of (macroscopic) mechanical properties with (molecular) dynamics. The following main research topics are addressed:

- The synthesis and molecular characterization of model systems

- How can non-linear mechanical melt properties be predicted?

  Does this enhance the understanding of the underlying relaxation processes?

- How do segmental chain dynamics, obtained by TD-NMR, correlate with the mechanical properties, obtained by rheological measurements?

  How does the concentration of the polymer relate to the mechanical modulus?

- Do the local dynamics in a polymerization reaction correlate with the macroscopic moduli, and if so, how can it be modeled?

The mentioned challenges are targeted by:

- Anionic synthesis of homopolymer model system with different topologies.

- Synthesis of deuteron labeled model system that are invisible in ^{1}H-NMR.

- Mechanical characterization of the model polymer melts by rheology in the linear and non-linear regime.

  The modeling of the mechanical characterization, allowing the prediction of the non-linear response.

- TD-NMR characterization of the polymer chain dynamics using partially deuterated polymer model systems.

  Comparing different parts of the polymer model systems to each other, which is possible due to the labeling.

- The *in situ* acquisition of TD-NMR and mechanical properties with a custom build Rheo-NMR setup of the polymerization of hydrogels, allowing for a correlation of the progress of polymerization with the mechanical properties, which removes the time component.

The interaction of the different topics of this work are presented in a graphical abstract in Figure 1.1.
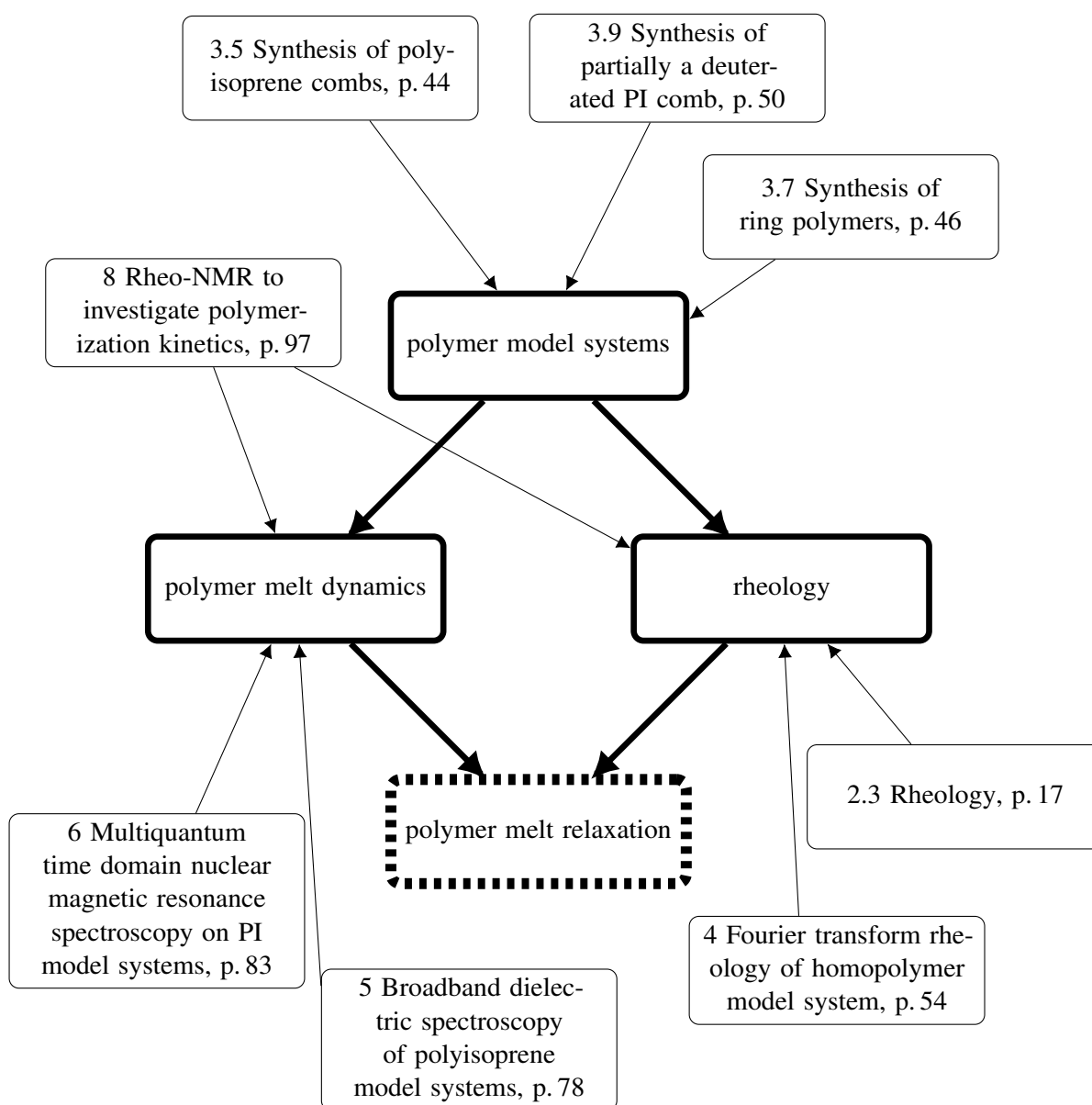
Figure 1.1. Graphical abstract that illustrates how *polymer model system* that are characterized in the field of *rheology* and *polymer melt dynamics* lead to an improved knowledge in the field of *polymer melt relaxation*. The respective chapters are linked to their respective topics.

2 Fundamentals

This chapter presents a overview of the methods and theories relevant to this thesis, which includes the synthesis, the modeling and the characterization of defined polymer systems. First, the general properties of polymers is summarized in *2.1 Fundamental properties of polymers*, followed by the description of the important synthesis methods employed in the current this thesis in *2.2 Living anionic polymerization*. Moreover, an introduction to rheology (of macromolecules) is given in *2.3 Rheology*. Since the findings of rheological measurements of polymer melts is a result of the polymer chain relaxation processes, these processes are elaborated in *2.4 Dynamics and rheological properties of polymer melts*. A method highly sensitive to local motions and restrictions of motions, *e.g.,* in polymer melts, is (time domain-)nuclear magnetic resonance relaxometry, which is covered in *2.5 Nuclear magnetic resonance (NMR) spectroscopy and relaxometry*.
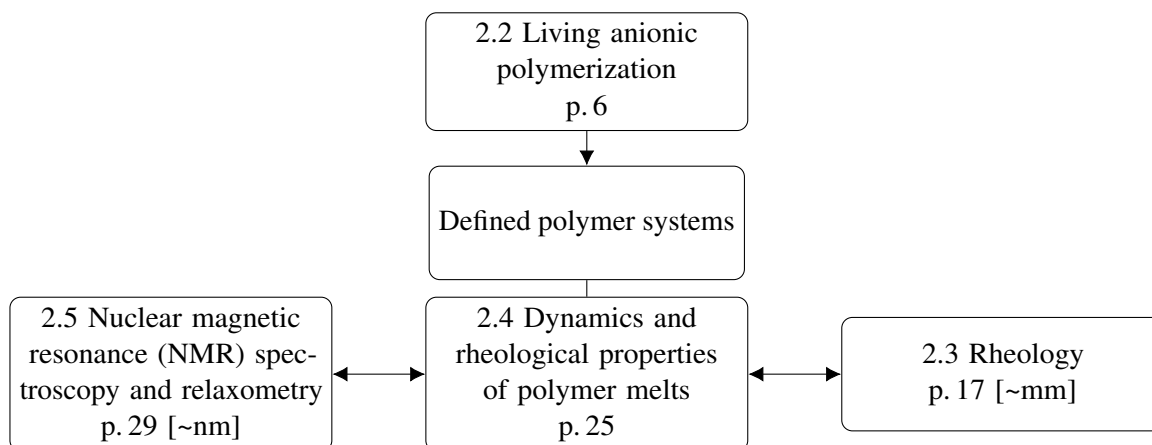
2.1 Fundamental properties of polymers

A hundred years ago, Hermann Staudinger introduced the concept of large molecules in 1920 [3], his ideas have laid the fundamentals of polymer science. Soon the term *macromolecule* was introduced by him in 1922.[4] Despite that his concept was first denied by his colleagues, further research proved the existence of macromolecules. As a result in 1953 Staudinger was rewarded with the Nobel price in chemistry for this work. Over the time, the term *polymer*, from the Greek words *poly* - many and *mer* - part, has been established instead of macromolecules. Today, polymers are of tremendous industrial importance with an annual production capacity of $\geq 350\,\mathrm{Mt/a}$ [2].

Polymers are large molecules, with covalent chemical bonds, with high molecular weights, at least one repeating unit that can be extracted from nature or synthesized artificially. Polymers are defined by their monomers, topology, average molecular weight (number of repeating units) and molecular weight distribution.[1] Many methods to characterize the average molecular weight have been established, with size exclusion chromatography (SEC) being the most employed one.[2]

$$M_{\mathrm{n}} = \frac{\sum_i n_i M_i}{\sum_i n_i},$$

(2.1)

$$M_{\mathrm{w}} = \frac{\sum_i n_i M_i^2}{\sum_i n_i M_i},$$

(2.2)

$$Đ = \frac{M_{\mathrm{w}}}{M_{\mathrm{n}}}$$

(2.3)

Two types of average molecular weights are important in the current thesis, the number-average molecular weight M_{n} (see Equation 2.1)[3] and the weight-average molecular weight M_{w} (see Equation 2.2).[4] Moreover, the dispersity $Đ$ (see Equation 2.3, old: polydispersity index PDI) characterizes the width of the molecular weight distribution.[5]

Polymers belong to the material class of *soft matter* with characteristic properties, *e.g.,* they possess diverse flow properties depending on the temperature, even without any 1st order phase transition in the case of amorphous polymers. For polymer melts these characteristics are discussed in 2.3 *Rheology*, p. 17. One of the most important features of amorphous soft matter is the *glass transition* temperature T_g, which is a 2nd order phase transition that representing a transition from a melt to a frozen melt (and keeping the amorphous state).

Solid properties and the G- and E-modulus are briefly outlined in 2.3 *Rheology*, as well.

---

[1] For the processing of polymers further parameters are relevant, e.g, morphology, additives, functionalizations and many more.

[2] For SEC a sample specific calibration is necessary. Many methods can be applied without a sample specific calibration, such as static light scattering (SLS) or SEC-MALLS (multi angle laser light scattering). The latter theoretically only requires the injected sample mass, the other required parameter (dn/dc) can be obtained using a (differential) refractive index detector. For further introductions the reader is referred to the literature [5].

[3] M_{n} is used as a synthesis parameter. The amount of polymer chain ends is reciprocally proportional to M_{n}.

[4] M_{w} is important in rheology, here the interplay of chains is important.

[5] The dispersity ranges from ≥ 1.01 for anionically polymerized samples[6], to about 2 for radical polymerizations and can exceed 100 controlled reactions with multiple catalysts and blends.

2.2 Living anionic polymerization

In 1956 M. Szwarc first introduced the concept of 'Living Polymers', with anions as active centers that can grow for an 'indefinite' amount of time, as long as they are provided with a sufficient amount of monomer/'food'. Once the polymerization starts *via* the employment of an initiator, the reaction is propagates by consuming monomers until the active center is 'killed' by forming a neutral species or less nucleophile species in the termination step.[6]

If the initiation is fast and quantitative, and all side-reactions are suppressed, very narrow and defined molecular weight distributions can be achieved, which can be described by a Poisson distribution in the ideal case.[8] This advantage makes the anionic synthesis a profound tool to synthesize highly defined polymer architectures including narrow molecular weight distributions, defined microstructure and precursors to special topologies.

The high technical standards of the synthetic parameters make the anionic synthesis rather costly in comparison to radical or coordinative polymerization. As a result the market share for anionic polymers is relatively small. Thermoplastic multiblock-co-polymers accounted to about 700 kt/a[9], oxyanionic polymers (such as polyethyleneoxid, polypropyleneoxid and co-polymers) to several million tons per year[9] and other anionically synthesized elastomers in the order of 1 Mt/a[10] in the year 2018.[7] These polymers stand in contrast to the previously mentioned $\geq$350 Mt/a for the total polymer production volume [2].

In the following the terms *living* polymerization, *living anionic* polymerization, *anionic* and *carb-anionic* polymerization are the used synonymously and refer to the special case of *living anionic* polymerization with propagating carbanioins.

2.2.1 Mechanism and kinetics

(Carb-)anionic polymerization, radical polymerization, controlled radical polymerization, cationic polymerization and coordinative polymerization, are belonging to the class of a *chain growth* polymerizations. In contrast to those, a *step growth* mechanism is found for polyadditions and polycondensations, which are not further elaborated and the reader is referred to the literature[11].

In order to obtain living reactive centers, all side reactions need to be suppressed, which limits the usable monomers, solvents and reaction environments. For very narrow distributions, the reactive centers need to be formed simultaneously, or at least in the order of the rate of propagation, which limits the available initiators.

The prerequisite for a solvent and the reaction environment is that it does not interfere with the strongly basic and nucleophilic anion. Traces of oxygen, water and other impurities need to be removed by applying high vacuum techniques with inert gas, so called Schlenk techniques.[12] Solvents have to be non-protic and not electrophilic. They possibly include alkenes, cyclohexane, benzene, toluene, ethylbenzene, and

---

[6]The words cited in ' ' (such as 'living', 'food', or 'killed') are taken from the original literature.[7]

[7]Solution polymerized elastomers are either polymerized using an anionic synthesis or coordinative polymerization. Both mechanisms show strong similarities as explained throughout the chapter.

tetrahydrofurane (THF). However, certain side reactions occur, *e.g.,* toluene can be deprotonated on a time frame of days, and THF can side-react, especially at $T > -50\,°C$, resulting in a ring opening or deprotonation at the alpha position.

Initiation

In the initiation step the reactive center is formed. Typically used (co-)initiators are lithium-alkyles, special charge transfer complexes or pure alkalimetals. Initiators are either commercially available or formed *in situ*.[13]

In case of lithium-alkyles, the reactant is in an equilibrium between agglomerates and single species, *e.g., sec*-butyllithium (*sec*-BuLi) forms mostly tetrameres in hydrocarbons, which are subject to a dynamic equilibrium with its active single species. This equilibrium is highly sensitive towards to the polarity of the solvent and Lewis bases (*e.g.,* ethers, like THF and crown ethers, or chelat complexes like *N,N,N',N'*-tetramethylethan-1,2-diamin). Figure 2.1 displays the initiation of styrene using *sec*-BuLi.
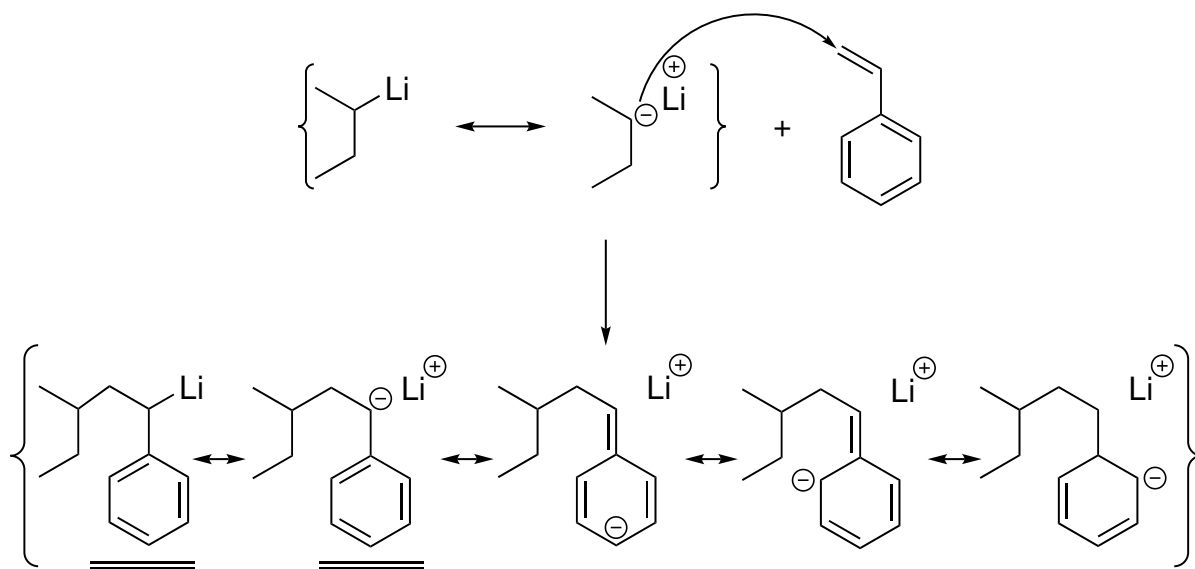
Figure 2.1. The initiation of styrene using *sec*-BuLi. In its active form the *sec*-BuLi can be described using two mesomeric forms. The carb-anion of the alkylgroup attacks the double bond of the styrene on the β-position. The resulting anion is stabilized throughout the phenylic ring, which is much more stable than the theoretical product stemming from an attack on the α-position. The important resonance structures of the initiated styrene-anion are underlined.

Sodium naphthalenide, as an example for alkali naphthalenide, can be employed as a co-initiator. This complex itself is not attached to the later polymer chain, but is a platform that stores an electron. In the first step the initiator is synthesized *in situ* by stirring sodium with naphthalene in a polar nonprotic solvent like THF. Once the residual sodium metal is separated, the co-initiator solution can be used either to immediately start the reaction as depicted in Figure 2.2 or to titrate the solvent to validate the absence of water. In the initiation step, the stored electron is transferred directly to a monomer forming a radical anion, which can recombine with the same species to a bi-anion. This type of initiator is employed, for the

synthesis of an α,ω-functionalized polymer chains or rings.[14, 15] Lithium, sodium and potassium can be used in this fashion. By employing a bi-anion the molecular weight is doubled compared to the usage of a monofuctional initator, such as *sec*-BuLi, with the same monomer. Moreover, a mirror-symmetric chain growths can be employed to polymerize symmetric triblock-co-polymers.
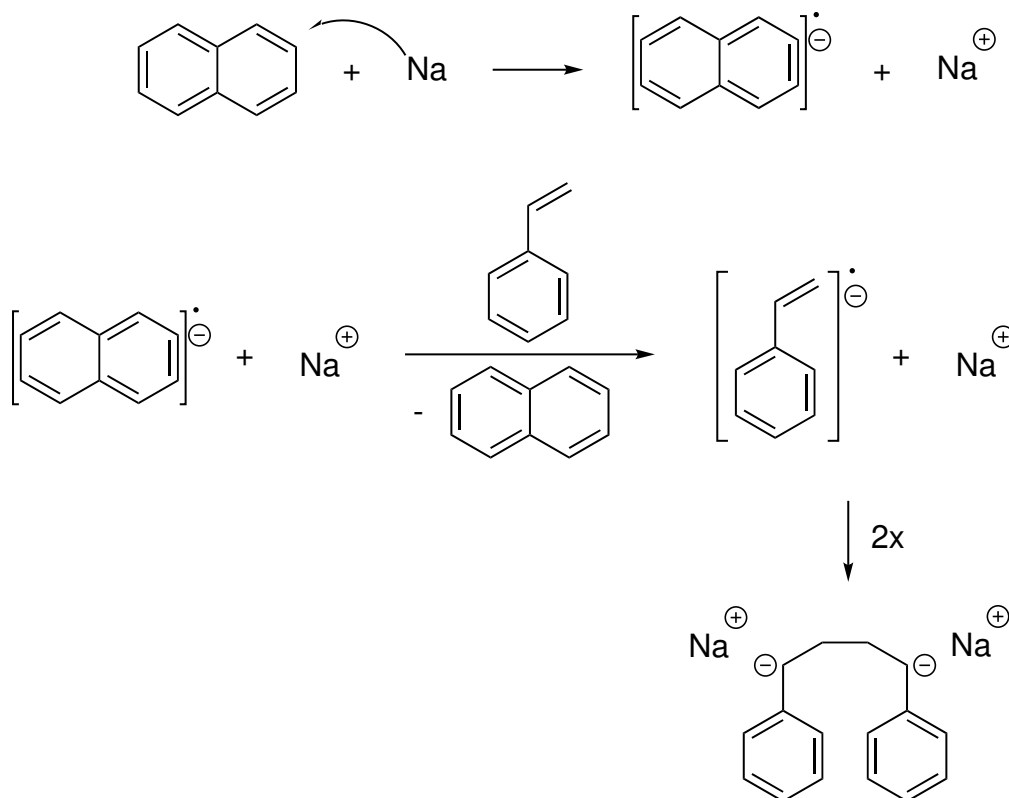
Figure 2.2. The initiation of styrene using the co-initiator sodium naphthalenide. In the first step, sodium naphthalenide is formed *in situ* using sodium and naphthalene in *e.g.,* THF. In the initiation step, an electron is transferred a styrene, forming an radical anion, while the naphthalene is reformed. Two units of the radical anion species can combine, forming a bi-anion. The resulting polymer will be mirror-symmetric.

In special cases, where the ceiling temperature[8] is above the reaction temperature, alkali metals can be directly used as a reactant. Since the electron transfer is a surface reaction, it is rather slow and highly influenced by the convection and diffusion towards the metal surface. After the reactive di-anions have been formed and the residual metal was removed, the propagation can be started by either reducing the temperature below the ceiling temperature or by adding monomers with a higher ceiling temperature. A mandatory requirement for the initiator is that its reactivity is high enough to initiate the polymerization (in the ideal case much faster than the propagation) and that the reactivity is mild enough to prevent side reactions. An example for a side reaction is the nucleophilic attack of *sec*-BuLi at the carbonyl group of methyl-(meth)acrylate. Its reactivity can be reduced by polymerizing a single step using diphenylethylene as a monomer/co-initiator. The resulting species employs the required conditions for anionic polymerization with meth acrylates.

---

[8]The ceiling temperature is the temperature, where the propagation reaction is in equilibrium with the depolymerization.

Propagation

In the propagation step monomers are continuously added/inserted in the active center. While the monomer is consumed, the degree of polymerization (P_n) grows linear in time. The mechanism is similar to the initiation using *sec*-BuLi. For every propagation reaction the P_n increases by one.

Depending on the polarity of the solvent and the counterion of the anion, the mechanism resembles either a *nucleophilic attack* (see Figure 2.3) of an nucleophile (anion) to an electrophile (double bond) or *coordinative polymerization* mechanism (refer Figure 2.4). Typical monomers are butadiene, isoprene, styrene (and derivates) and meth acrylate esters (such as methyl methacrylate, MMA).
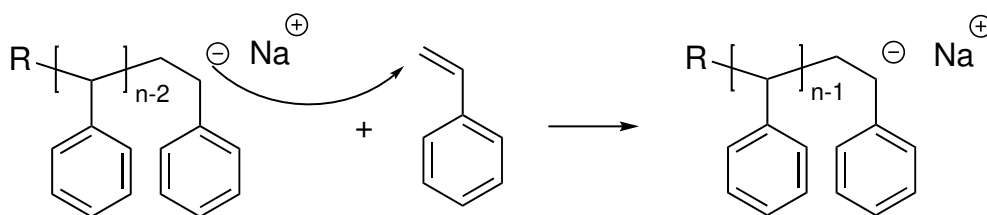
Figure 2.3. Propagation step of styrene in a polar solvent with sodium as a counter ion. The electron pair of the carb-anion attacks the alpha postion of the vinyl group of the styrene, resulting in an macroanion that is extended by one monomer unit.
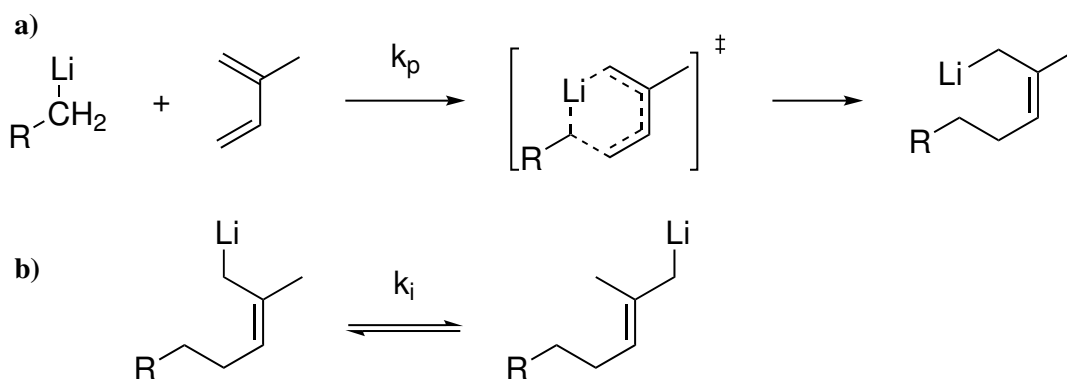
Figure 2.4. a) Propagation reaction of isoprene in an unpolar solvent (*e.g.,* cyclohexane) with lithium as a counter ion. The C-Li bond is a highly polarized σ-bond, where an additional isoprene can coordinate to. *Via* a cyclic six centered transition state, the new monomer unit is inserted into the propagating chain. Aggregates are neglected in this scheme. **b)** Simultaneous to the propagation reaction, an isomerization can occur, resulting in trans-1,4 polyisoprene. As a general rule, the rate of propagation k_p is four times bigger as the rate of isomerization k_i, which is confirmed by an approximate 1,4-cis content of 90 %.[16–18]

The propagation reaction continuously consumes monomer units until complete conversion is reached. Once no monomers are left the carbanioin stays active until it is terminated. As a result, upon further addition of monomer units, the propagation process can continue. Moreover, the active species can be used as a 'macro-initiator' for another type of monomer, resulting in block co-polymers, refer to section 2.2.4 *Block-co-polymers*, p. 13. However, not all transitions between monomer types are possible, due to strong differences in reactivities: A transition from styrene to isoprene or *vise versa* performs in an

sufficient manner. However, a transition from, *e.g.,* MMA to styrene is inhibited. The other way, styrene to MMA, is possible, by applying diphenyleethylene as a compatibilizer.

Termination

The termination step terminates the propagation process by 'killing' and therefore deactivating its active species.[7, 20] The polymerization process can be terminated by adding protic substances, such as methanol.[9] Besides proton donators, electrophiles such as dihalogenalkyles, epoxides and carbondioxide can be applied resulting in halogen-, alcohol and carbonic acid functionalized polymers, respectively (refer to Figure 2.5). Oxygen reacts with carb-anions as well, however in a rather ill defined manner, resulting in a multitude of functionalities and a bidisperse molecular weight distribution by partially coupling of the resulting radicals. The mechanisms are displayed in Figure 2.5. Small traces of oxygen are enough to have a fraction of the double molecular weight species, which is displayed in Figure 2.5. As a result degassed solvents are required as termination-agents to avoid this process.

In contrast to radical polymerizations, the active centers of carb-anionic polymerizations cannot react with each other, since both centers are nucleophile. The monomer/termination agents are the only electrophile species available.

---

[9]Water is typically not used, since it is not miscible with unpolar solvents.
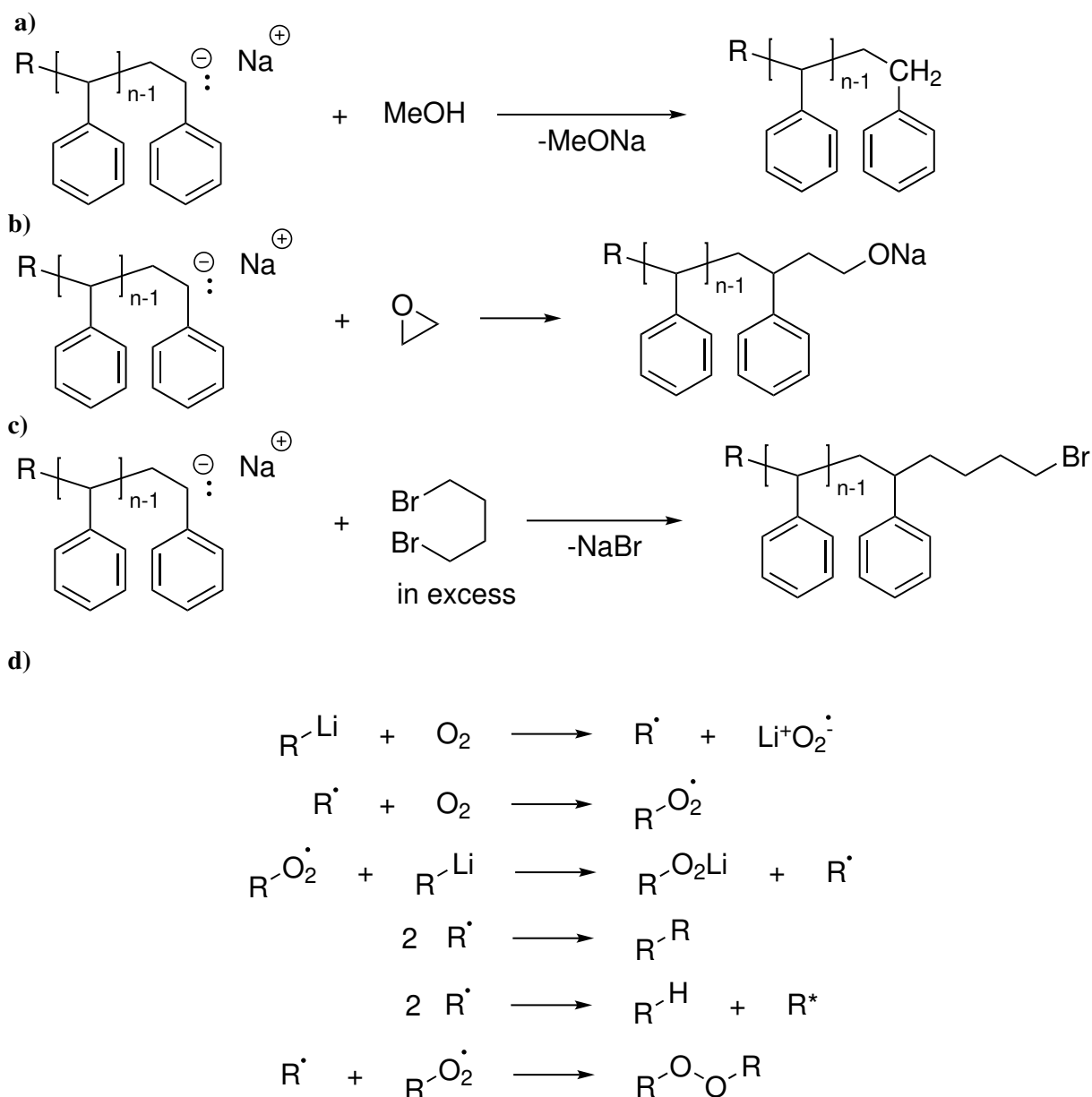
Figure 2.5. Possible termination reactions of carb-anions by taking the example of polystyrene with sodium as a counter ion or any polymer with lithium as a counterion. After the reaction with the termination agent the resulting species are either inert or functionalized, but unable to propagate further in a carb-anionic polymerization. The polymer chains (**R**) are not necessarily the same.

a) Termination step using methanol: The acidic proton is transferred to the (highly basic) carb-anionic center, resulting in an inert polymer, a so called 'H-terminated' polymer.

b) Termination step using ethylene oxide: The resulting anion is unable to polymerize in a carb-anionic manner, but can be employed for oxoanionic polymerization or other functionalization reactions.

c) Termination step using an excess of dibrom-butane: The carb-anion substitutes the bromine group. Since the regent is employed in excess the possibility of the second group reacting is negligible.

d) Termination process reaction with oxygen. In a first step an electron is transferred from the anion to the oxygen. The resulting species can react in a multitude of reactions, with a possibility small possibility to form to dimers, resulting in a fraction of species with double molecular weight. Herein, some of the most relevant termination reactions are listed, for additional cases the reader is referred to literature.[19] The **R*** symbolizes a polymer chain with a double bond.

2.2.2 Molecular weight distribution

In the ideal case, the anionic polymerization results in a Poisson distribution.[12] The Poisson distribution resembles a Gaussian distribution for sufficiently high degrees of polymerization. The ideally achievable narrowness of the distribution can be calculated as in Equation 2.4.[12]

$$\DJ \approx 1 + \frac{1}{P_n} \tag{2.4}$$

Since typical degrees of polymerization are $P_n \geq 100$, the theoretical dispersity is $\DJ < 1.01$.[10] Very narrow distributions have been reported literature, lower than 1.01, which is nevertheless a higher dispersity than a Poisson distribution.[6]

2.2.3 Accessible topologies, microstructures and tacticity

The key characteristics of anionic polymerization - monodisperse distributions and living (nucleophile) anions - can be used to target specific polymer topologies. Furthermore, the co-polymerization process can be fine tuned by adding, *e.g.,* randomizers to yield statistical copolymers. Moreover, the microstructure can be influenced, especially for 1,3 dienes. Anionic polymerization has little impact on the relative stereochemistry (tacticity) of the resulting polymer, resulting in dominantly atactic polymers, therefore, the tacticity is not discussed within this work.

2.2.4 Microstructues of polyisoprene

Polyisoprene has four micro-structues, which are present to different degrees in polyisoprene. In Figure 2.6 the different microstructures of polyisoprene are displayed. The 1,4 *cis*-structure is highly valued in tire industry. Therefore, special catalysts and expensive natural rubber (fully 1,4 *cis*-PI) are employed. The highest impact on the microstructure has the polarity of the solvent: In unpolar solvents the 1,4 *cis*-structure is favored, and in polar solvents the 3,4 structure is preferably formed.
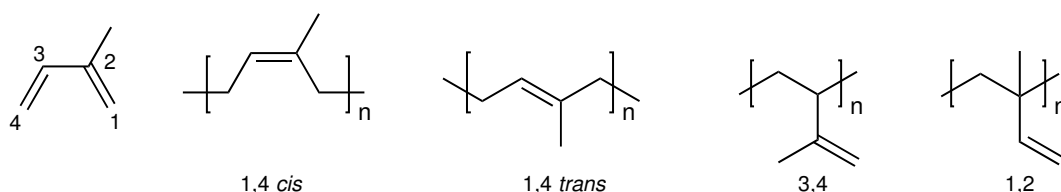
Figure 2.6. Microstructures of polyisoprene. First the numbering of the monomer, then from left to the right: 1,4 *cis*-polyisoprene, 1,4 *trans*-polyisoprene, 3,4-polyisoprene and 1,2-polyisoprene. Typically the 1,4 *cis*-structure is desired, since it shows superior elastic properties. Moreover, a pure 1,4 *cis*-polyisoprene, as found in natural rubber, can crystallize under large strain, which highly enhances its fatigue behavior.

---

[10]The typical characterization method for molar mass dispersity is size-exclusion-chromatography (SEC). This method has an intrinsic systematic line-broadening which lead to apparent broader distributions. The most narrow distribution observed with SEC in this thesis was 1.02.

Block-co-polymers

Anionic polymerization can yield block-co-polymers in a very straight-forward fashion. The mechanisms has already been shortly introduced in 2.2.1 *Propagation*, p. 9. Once initiated, the carb-anion consumes all monomer and is subsequently fed with the sequence of the desired monomers resulting in the respective block-co-polymer. This procedure is emphasized in Figure 2.7. Block-co polymers of PS-PI-PS, PS-PB-PS or their partially hydrogenated analogs are known as 'Kraton' or other brand names, and make up for most of carb-anionic polymers (a total of 700 kt/a[9]). They combine the elastic properties of the PI and the thermoplastic properties of PS, resulting in injection moldable thermoplastic elastomers.
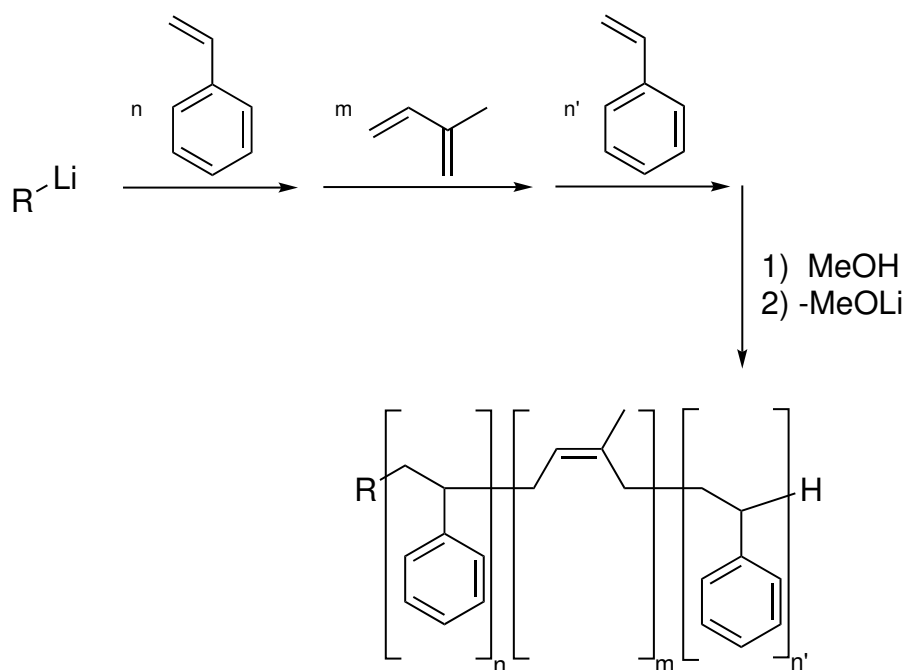
Figure 2.7. Synthesis scheme of a PS-PI-PS block-co-polymer by subsequent addition of styrene, isoprene and styrene.

Ring polymers

By using anionic synthesis and a bifunctional initator, *e.g.,* sodium and naphthalenide, monodisperse rings are accessible. For this specific synthesis, the dianion is terminated with a bifunctional linker such as α, α'-dibromo-para-xylene under extreme dilution (refer to Figure 2.8). The product is a mixture of rings, linear uncoupled analogs, linear chain condensation products and bigger rings. This mixture needs to be purified, *e.g.*, by fractional precipitation, in order to separate by molecular weight. Moreover, liquid chromatography under critical conditions, which separates different chemical structures independent from their molecular weight, has to be employed to quantitatively separate rings from linear chains.
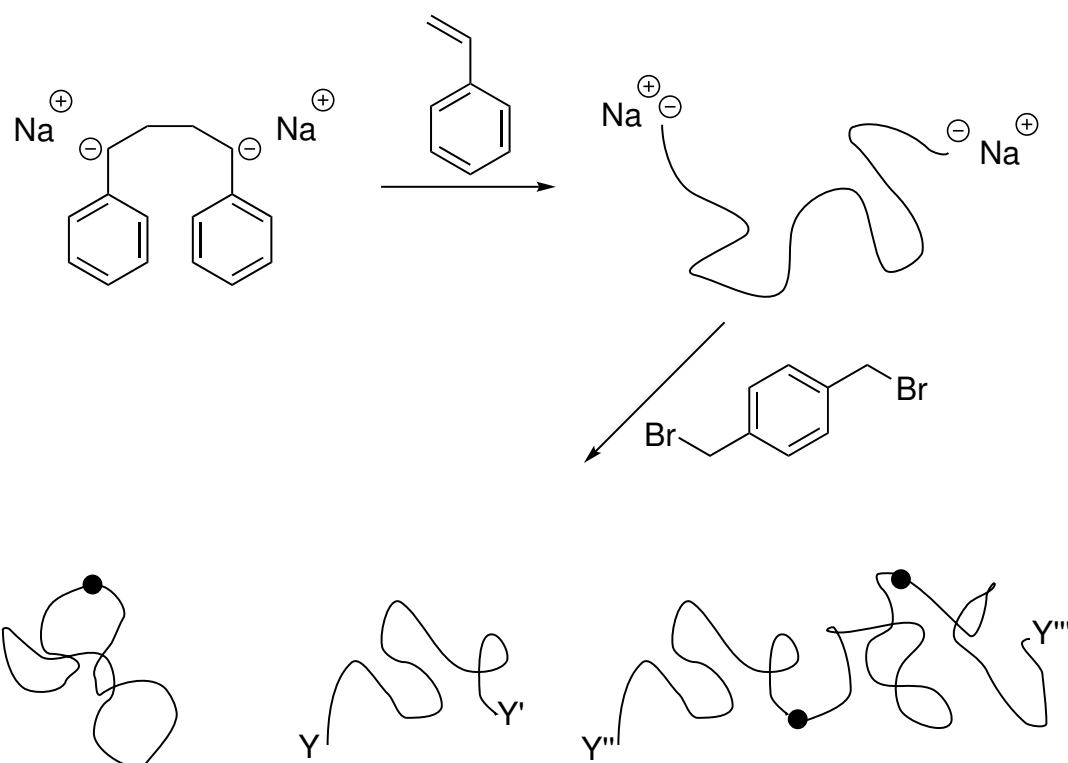
Figure 2.8. Polymer ring synthesis using a dianion and a bifunctional linker. The line represents the polymer chain, the black dot the linker and Y any side reaction adduct. The anions attack the electrophil groups in a statistical manner, resulting in rings, condensation products and linear analogs. The condensation products can form rings with multitutes of the molecular weight of the employed dianion. In order to reduce these side reactions the synthesis is performed under in extreme dilution. The resulting polymer mixture contains both rings, bigger rings/condenstaion products and a certain amount of linear chains due to unwanted termination reactions.

Comb polymers

Comb polymers can be synthesized according to three different approaches: *grafting onto*, *grafting from* and *grafting through*.[12] These methods are illustrated in Figure 2.9.

- grafting onto: A functionalized polymer is employed as a backbone. This backbone carries electrophil groups like epoxides, alkylchlorides or carbonyles.[12, 21] Living anions are generated independently. Upon mixing the functionalized backbone with the macroanions, the living anions attack the electrophil groups in a statistical manner, neglecting sterical hinderance.

- grafting from: A functionalized polymer is employed as a backbone in this approach as well. These functional groups serve as initiators, upon employing a co-initiator. These active species react in typical propagation steps. This method has minor importance for carb-anionic polymerization, because the required functional groups are not suitable to be employed in anionic synthesis themselves. Therefore, additional protection steps/groups have to be utilized.

- grafting through: co-polymerization of monomer and macromonomers. In a prior step, macromonomers are synthesized, by common anionic polymerization and post functionalization to introduce a double bone at the chain end. The macromonomers are co-polymerized with the monomer. The

distribution of the sidearms depends on the co-polymerization parameters, and it is in the best case a statistical distribution.[22] To tune the copolymerization parameters, randomizers such as organic potassium salts can be added.

a)

b)

c)
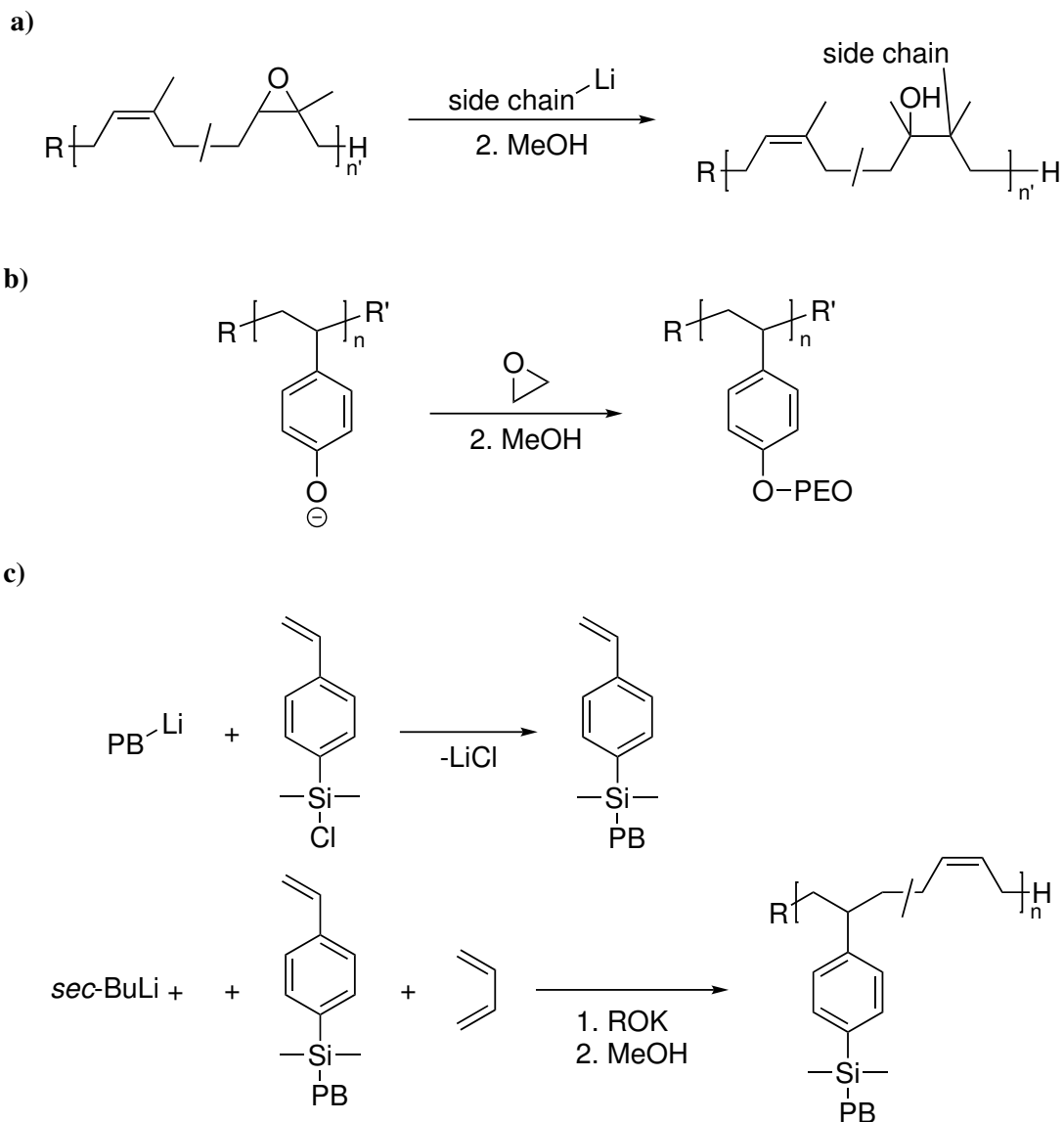
Figure 2.9. Different routes for the synthesis of comb polymers:
a) Grafting onto: A polymer backbone, with functional groups is employed. These electrophil groups are attacked by living anions resulting in a statistical distribution of the side-arms along the backbone.
b) Grafting from: This approach holds little importance for carbanioic polymerization, since it is difficult to yield new carb-anions without side reactions. Nevertheless, an example for oxoanionic polymerization is presented using a poly-phenolate.[23]
c) Grafting through: A co-polymerization of macro monomers. Additional regents are required to yield a mostly statistical co-polymer. For further detail the reader is referred to the literature.[22, 24] A polymerization of the pure macro monomer is challenging, due to its high ceiling temperature.

Star polymers and pom-pom polymers

Similar to comb polymers, star polymers and linked stars, so-called pom-poms can be synthesized. In order to yield a star polymer, an excess of living anions is subjected the reaction with a species with multiple electrophile groups. The result is a star polymer (refer to Figure 2.10). During the grafting process typical side reactions lead to terminated side chains.

A pom-pom (refer to Figure 2.11) is a polymer topology, which features two star polymers at their cores. The connecting unit is typically longer than the side arms of the pom. In general the reaction starts with an α, ω-functionalized polymer.[25] These functionalizations are further extended to be multiple electrophile groups and this chain is employed in the same manner as the star polymers, by adding living polymers to the α, ω-functionalized polymer. Few synthesis routes have been published to yield pom-poms using living techniques.[25]

Figure 2.10. Scheme of a star polymer. The side arms are equally long and are connected to a single linker molecule.

Figure 2.11. Scheme of a pom-pom polymer. Two star (poms) polymers are connected by a backbone (dotted line). The side arms are of equal length. Furthermore, the backbone is typically longer than the side arms.

2.3 Rheology

Rheology is the science of the flow and deformation of matter.[26, 27] The name is derived from the ancient greek ῥέω *rheo* or greek ῥεῖν *rhein* both meaning 'flow', while λόγος *logos* translates to 'the study of'.

By applying forces onto a body a deformation is induced. The investigation and detection of these deformations is subject to the science of rheology. Matter flows on many time and length scales and is visible our daily lives:

- The flow of air, namely wind, as the least viscous commonly known substance.

- Water and oil are both liquids, but they have a significant difference in viscosity.

- Dough is very viscous and has elastic contributions. It is very similar to polymer melts which is the main subject of this thesis.

- Steel is very hard and in most applications fully elastic.

- Stones and mountains are considered hard and not moving, yet they flow in the time range of geologic eras.

By characterizing the rheological properties of matter important parameters for processing and application can be derived. For rheology of polymer (melts), the properties such as glass transition temperature T_g and melt viscosity are highly correlated with the molecular properties, such as used monomers and molecular weight.

This chapter guides the reader through an introduction of rheology, with an emphasis on polymer melts. Therefore, the dynamics of polymer melts are introduced and subsequently related to the rheological properties. Finally, Fourier-transform rheology applied to oscillatory shear conditions is described as a tool to characterize non-linear fluids. For a more in-depth introduction, the reader is referred to literature.[26–30]

2.3.1 Introduction

There are two types of flow which can be differentiated during a deformation: *Shear* flow and *elongational* flow (refer to Figure 2.12)

In this work only homogeneous incompressible materials, such as homopolymer melts, are discussed, excluding multi-phase systems, such as polystyrene-*block*-polyisoprene-co-polymers.
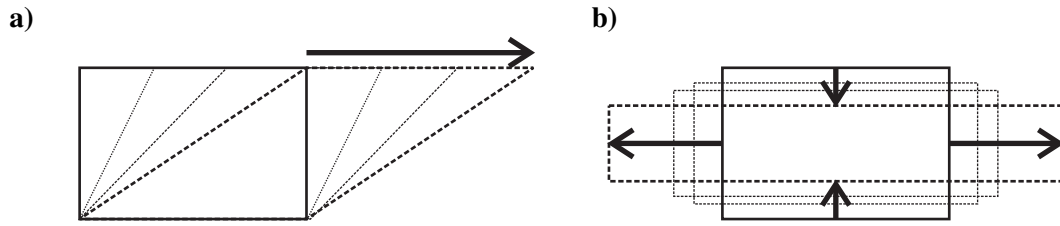
Figure 2.12. a) Illustration of shear flow. Adjacent (arbitrary) particles are moving past each other. The distance between the plates and the contact area at the plates remain constant.
b) Illustration of elongational flow. Adjacent (arbitrary) particles are moving towards or away from each other. The contact area and the length of the sample are changing. As the sample is practically incompressible, the Poisson ratio is $1/2$.

2.3.2 Shear rheology

In order to receive the underlying principles for shear rheology, a material is modeled with (arbitrary) particles flow past each other. This can be displayed in a layered structure (refer to Figure 2.13).
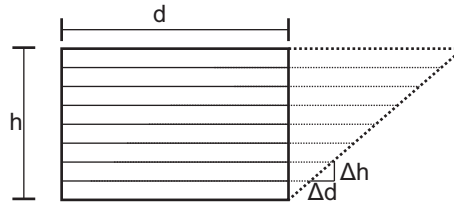
Figure 2.13. By applying a shear deformation the different (theoretical) layers are moving against each other. The total height of a sample is h and the displacement is d, the resulting strain is $d/h = \gamma$. The layers move against each other homogeneously, and therefore, every ratio of $(\Delta d)/(\Delta h)$ is the same and equals γ.

The relative deformation, the *shear amplitude*, is symbolized with γ and consequently, its time derivative, the *shear rate* is $\dot{\gamma} = d\gamma/dt$. The applied force per area is called *shear stress* with the symbol σ, see Equations 2.5, 2.7, and 2.6. For purely Newtonian fluids the proportionally coefficient of the deformation rate and the stress is the viscosity η:

$$\sigma_{viscous} = \eta \cdot \dot{\gamma} \tag{2.5}$$

For Hooke's springs (ideal solids) the proportionally factor between the stress and the deformation is the G-modulus G:

$$\sigma_{elastic} = G \cdot \gamma \tag{2.6}$$

Real substances contain viscous and elastic properties, the total stress can be split up into their individual contributions:

$$\sigma = \sigma_{viscous} + \sigma_{elastic} \tag{2.7}$$

by combining Equation 2.5, 2.6 and 2.7, the stress is displayed as a function of shear rate and deformation with their respective factors:

$$\sigma = \sigma_{viscous} + \sigma_{elastic} = \eta \cdot \dot{\gamma} + G \cdot \gamma \tag{2.8}$$

18

The most simple realizations for the combination of viscosity and elasticity are:

Maxwell Model: A dashpot and a spring in series. For long times this system relaxes fully. This is often applied to polymer melts, towards the flow regime.

Voigt Model: A dashpot and a spring in parallel. For long times this systems retains a stress. This is often applied to elastomers/rubbers/network-structures.

The viscosity and the G-modulus are related in Equation 2.9, assuming both quantities are complex scalars under sinusoidal excitation.

$$G = i\omega\eta \tag{2.9}$$

With ω being angular frequency and i being the imaginary unit ($i^2 = -1$). To indicate that the G-modulus is a complex number it is often written as G^* with its respective contributions of the storage modulus G' and the loss modulus G''. Similarly the viscosity can be described under oscillatory conditions as a complex number and has two components the non-dissipative part of the viscosity η' and the dissipative part η'':

$$G^*(\omega) = G'(\omega) + iG''(\omega) \tag{2.10}$$

$$\eta^* = \eta' - i\eta'' \tag{2.11}$$

In oscillatory shear rheology a time t dependent strain is applied, which is commonly a sine:

$$\gamma(t) = \gamma_0 \cdot \sin(\omega_1 \cdot t) \tag{2.12}$$

$$\dot{\gamma}(t) = \gamma_0\omega_i \cdot \cos(\omega_1 \cdot t) \tag{2.13}$$

Different responses are displayed in a time independent plot, the so called Lissajous figure in Figure 2.14. Applying an oscillatory strain, a oscillating response is observed for linear systems:

$$\sigma(t) = \sigma_0 \cdot \sin(\omega_1 t + \delta) \tag{2.14}$$

which includes a phase angle that is 0° for solids, 90° for liquids and in between these values for viscoelastic materials.

By combining Equations 2.10, 2.12, 2.13, and 2.14, Equation 2.15 and Equation 2.16 are obtained.

$$\sigma(t) = \gamma_0[G'(\omega_1)\sin(\omega_1 t) + G''(\omega_1)\cos(\omega_1 t)] \tag{2.15}$$

$$\tan(\delta) = G''/G' \tag{2.16}$$
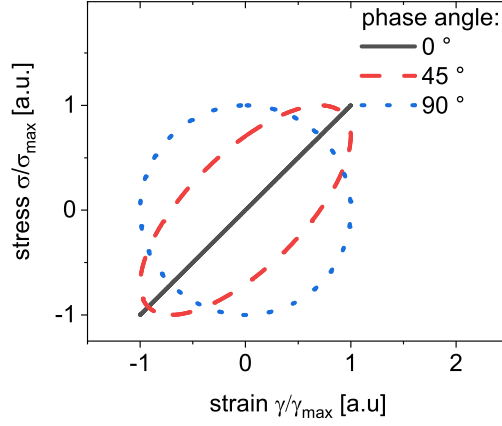
Figure 2.14. Stress-strain relationship for different phase angles in a Lissajous plot, which is commonly used in rheology and especially in non-linear rheology such as [31]. This form of presentation eliminates the time component by correlating the stress and strain for each time step. For linear responses, the results are ellipsoid with the circle being the limit towards 90°, which implies a full viscous response. Moreover, the line being the limit towards 0°, which implies a full elastic response. Any phase angle in between, such as 45°, relates to a visco-elastic response.

Frequency dependent G-moduli can be represented by maxwell modes, assuming (multiple) Maxwell models:

$$
\begin{aligned}
G'(\omega) &= \sum_{i=1}^{N} \frac{G_i \cdot (\omega \tau_i)^2}{1 + (\omega \tau_i)^2} \\
G''(\omega) &= \sum_{i=1}^{N} \frac{G_i \cdot (\omega \tau_i)^2}{1 + (\omega \tau_i)}
\end{aligned}
\tag{2.17}
$$

with τ_i being the respective relaxation times. In general the relaxation time is the mean time for a system/autorelaxation function to relax to $1/e$ of its initial value.

2.3.3 Oscillatory shear rheology on polymers

Until now the G-modulus and viscosity have been described without considering the effect of temperature. From daily live observation, one can expect the temperature dependency of these observables. Therefore, G^* depends on the angular frequency and the temperature. For polymer melts, the temperature difference between two measurement, can be expressed in a shift in frequency by in a shift factor (a_T) with respect to the relaxation time as in Equation 2.18.

$$
\tau_i(T) = a_T(T)\tau_i(T_0)
\tag{2.18}
$$

where τ_i is any unspecified relaxation time within polymer science. This phenomena is called the *time temperature superposition - TTS*.[26] This tool allows to cover a very broad range of frequencies, which are typically not accessible due to the experimental limitations of instruments. Two important models

20

describe the temperature influence on polymers: the Arrhenius dependency (refer to Equation 2.19) and the WLF (named after Williams, Landel and Ferry) equation [32] (refer to Equation 2.20).[11]

$$a_T(T) = \exp\left[\frac{E_a}{R} \cdot \left(\frac{1}{T} - \frac{1}{T_0}\right)\right] \tag{2.19}$$

$$a_T(T) = \exp\left[\frac{-C_1 \cdot (T - T_0)}{C_2 + T - T_0}\right] \tag{2.20}$$

A frequency dependent G-modulus is plotted in Figure 2.15, in the presented graph the TTS was applied to yield a wider dynamic range.
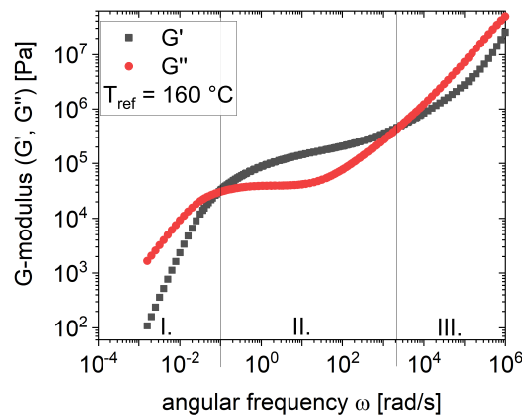
Figure 2.15. Example of a master-curve for the G-modulus of a monodisperse polystyrene sample with a molucular weight of $M_n = 330$ kg/mol, which is an amorphous (non-crystalline) polymer. The dynamic range covers 9 decades. Moreover, the graph is organized in 3 different frequency ranges. They are typically named (left to right): *flow regime*, *rubber regime/rubber plateau* and *transition zone*. The forth regime, the *glassy regime*, requires additional experimental effort, such as swapping to different geometries.

In the graph three zones are highlighted in which characteristic processes are dominant. Details on these processes are discussed in chapter 2.4 *Dynamics and rheological properties of polymer melts*, p. 25.

I. flow regime: The polymer chain relaxation is faster than the excitation, therefore, the polymer shows little storage capacities and the viscous behavior is dominant.

II. rubber plateau: The oscillatory excitation is faster than the relaxation process of the polymers, leading to a quasi network though entanglements of the polymer chains. The quasi network is similar to rubbers, in which the network is covalently cross-linked. Therefore, rubbers do not have a flow regime.

III. transition zone: This regime is less important for this work and is not discussed.

IV. glassy state: Below the T_g the polymer exhibits a high modulus, where most of the chain movements are 'frozen'.

---

[11]Please note that the Trios software (TA Instruments) fits the temperature dependency of the shift factors with a WLF fit, where $C1$(as in Equation 2.20) equals $-c1$ in the software.

Introduction into Fourier-transform rheology

So far only linear rheology was discussed, within these limits, the G-modulus is strain independent and only frequency dependent. However, for stronger deformations, this no longer applies as displayed in Figure 2.16, where at high amplitudes the G-modulus deviates. For high deformations the polymers orient
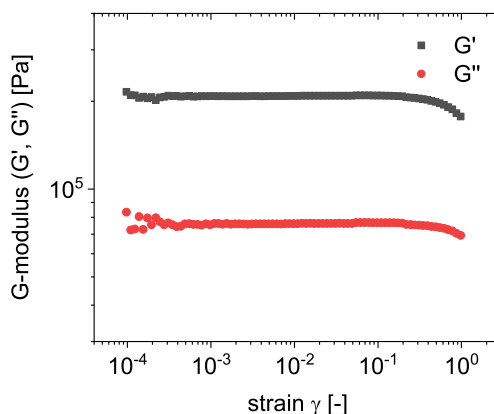
Figure 2.16. Dynamic frequency sweep of a monodisperse polystyrene with a $M_n = 330\,\mathrm{kg/mol}\;@T = 200\,°C$. For very little amplitudes one can notice the reduced sensitivity/higher noise. Up to $\gamma_0 \approx 0.1$ the G-modulus remains constant, but decreases afterwards.

and disentangle in the melt, resulting in a different response. The linear responses are observed in the **s**mall **a**mplitude **o**scillatory **s**hear *SAOS* (experiment) and small non-linear deviations are characterizable in the **m**edium **a**mplitude **o**scillatory **s**hear (MAOS). Large deformations in the **l**arge **a**mplitude **o**scillatory shear (LAOS) regime show dominant non-linear responses. The MAOS regime is the most important one to this work, since it is well suited for Fourier-transform rheology. Depending on the literature MAOS can be defined as a part of LAOS, bordering SAOS[33] or an independent regime between SAOS and LAOS[34].

The Fourier-transformation is a (complex) transformation of a certain dimension (*e.g.,* time) into its reciprocal dimension (*e.g.,* frequency), refer to Equation 2.21. Herein, all examples are a transformation from time $t\,[s]$ to the counter part the angular frequency $\omega\,[rad/s]$ (and *vise versa*), which is transformed into the frequency $\nu\,[Hz]$ by $2\pi\nu = \omega$.

$$f(t) \xleftrightarrow{\mathrm{FT}} \mathcal{F}(\omega_i) = \frac{1}{2\pi} \int_{-\infty}^{+\infty} f(t)\exp(-i\omega_i t)dt \tag{2.21}$$

with f being the original time dependent raw data and $\mathcal{F}$ being the respective Fourier-transformed spectrum. Fourier-transformations are very common in characterization methods in chemistry, for example in infrared spectroscopy (FT-IR), FT-nuclear magnetic resonance and X-ray scattering.

From hereon, the focus lies on the evaluation of rheological data, where a defined (sinusoidal) strain is applied and the stress response is obtained.

By applying a stress as a (perfect) sine, a sinusoidal response is obtained for linear systems which can be described as Equation 2.15. The Fourier-transformed stress signal yields a delta function with the excitation frequency as characteristic frequency. But for non-linear systems higher harmonic frequencies are observable, which implies that the response is no longer a (pure) sine, but still periodic.

For Newtonian fluids, the viscosity is not dependent on the strain rate (linear material):

$$\eta(\dot{\gamma}) = \eta_0 \tag{2.22}$$

For non-Newtonian fluids the non-linear deviation can be described using a Taylor-series:

$$\eta(\dot{\gamma}) = \eta_0 + \sum_{n=1} c_n \dot{\gamma}^{2n} \tag{2.23}$$

Odd terms are zero for systems relevant in this thesis, since they are isotropic melts/bodies.[12] With the simplification of the deformation using the complex notation $\exp(i(\omega t + \delta)) = \cos(\omega t + \delta) + i\sin(\omega t + \delta)$ and combining Equations 2.9, 2.8 and 2.23, one receives Equation 2.26 and Equation 2.29.

$$\gamma(t) = \gamma_0 \cdot \exp(i\omega_1 t) \tag{2.24}$$

$$\dot{\gamma}(t) = i\gamma_0 \omega_i \cdot \exp(i\omega_1 t) \tag{2.25}$$

$$\sigma(\dot{\gamma}) = (\eta_0 + c_1 \dot{\gamma}^2 ...) \tag{2.26}$$

$$\sigma(t) = (\eta_0 + \sum_{n=1} c_n \dot{\gamma}^{2n})\dot{\gamma} \tag{2.27}$$

$$\sigma(t) = (\eta_0 + c_1 i^2 \omega^2 \gamma_0^2 \exp(i2\omega t)...) \cdot i\omega\gamma_0 \exp(i\omega t) \tag{2.28}$$

$$\sigma(t) = \eta_0 \cdot i\omega\gamma_0 \exp(i\omega t) + c_1 i^3 \omega^3 \gamma_0^3 \exp(i3\omega t)... \tag{2.29}$$

The Equation 2.29 can be split into two components after neglecting higher terms:

$$\sigma(t) = \underbrace{\eta_0 \cdot i\omega\gamma_0 \exp(i\omega t)}_{} + \underbrace{c_1 i^3 \omega^3 \gamma_0^3 exp(i3\omega t)}_{} \tag{2.30}$$

$$= \quad\quad I_1 \quad\quad + \quad\quad I_3 \tag{2.31}$$

$$I_1 = \eta_0 \cdot i\omega\gamma_0 \exp(i\omega t) \tag{2.32}$$

$$I_3 = c_1 i^3 \omega^3 \gamma_0^3 \exp(i3\omega t) \tag{2.33}$$

where I_1 and I_3 are the intensities of the 1st and 3rd higher harmonic frequency. Equation 2.32 and Equation 2.32 exhibit a proportionality of the 1st and 3rd harmonic intensities of:

$$I_1 \propto \omega\gamma_0$$
$$I_3 \propto \omega^3 \gamma_0^3 \tag{2.34}$$

---

[12]Even harmonics are observable in anisotropic systems, *e.g.,* elongational rheology or crack propagation in a fatigue measurement.

The signal of the 3rd harmonic frequency can be normalized to the 1st harmonic, in order to compensate for the resulting modulus loss for high shear rates and to increase the reproducibility. This parameter is called $I_{3/1} = I_3/I_1$. Following Equation 2.34, $I_{3/1}$ has a quadratic dependence on γ, refer to Equation 2.35, which is visualized in Figure 2.17.

$$I_{3/1} \propto \gamma_0^2 \tag{2.35}$$

A strain independent non-linearity parameter $^3Q(\omega, \gamma_0)$ and the intrinsic non-linearity parameter $^3Q_0(\omega)$ has been introduced by Hyun $et\ al.$[34]:

$$^3Q(\omega, \gamma_0) \equiv \frac{I_{3/1}}{\gamma_0^2} \tag{2.36}$$

$$^3Q_0(\omega) \equiv \lim_{\gamma_0 \to 0} {}^3Q(\omega, \gamma_0) \tag{2.37}$$

$$^3Q_0(\omega) \equiv \lim_{\gamma_0 \to 0} \frac{I_{3/1}}{\gamma_0^2} \tag{2.38}$$
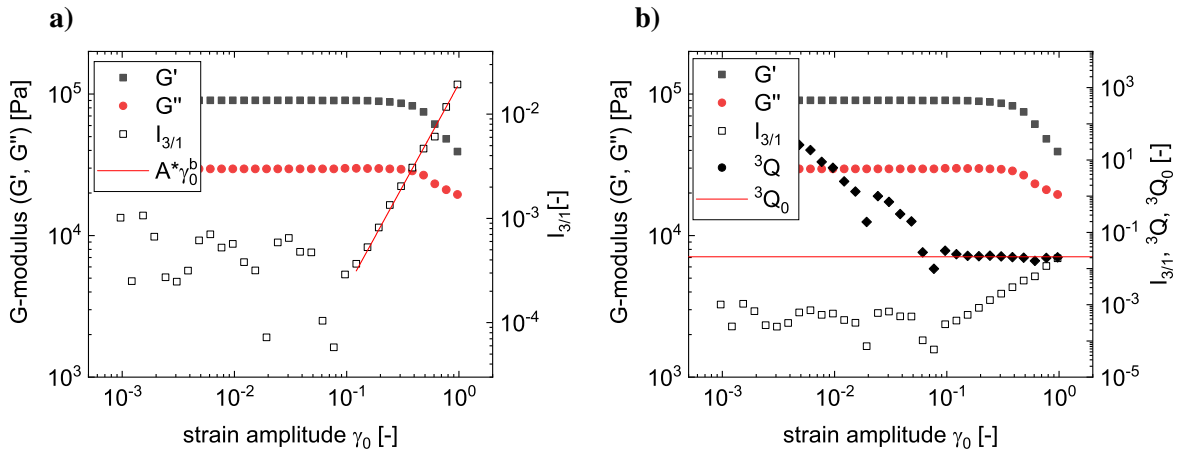
Figure 2.17. Dynamic strain sweep of a PI melt. **a)** The non-liniarity parameter $I_{3/1}$ and G-modulus as a function of γ_0 for a bidisperse PI in the flow regime. In the MAOS regime ($\gamma_0 = 10\,\%$ to $100\,\%$) a power law is observable with an exponent of $b = 1.96$ which is close to the expected value of 2 (refer to Equation 2.35). **b)** The intrinsic non-linearity parameter ^3Q as a function of γ_0, here a plateau is observable for $^3Q_0 = 0.021$.

Since ^3Q theoretically is a plateau, therefore, an extrapolation is mathematically not necessary and ^3Q equals to the value of the plateau, as displayed in Figure 2.17. Practically this plateau does not cover the full range of shear amplitudes. For small amplitudes the sensitivity of the rheometer is the limiting factor, and for high amplitudes, the sample is pressed out of the geometry gap and the theoretical limit for $I_{3/1}$ is approached, which are discussed $e.g.$, in [35].[13]

---

[13]The limit of $I_{3/1} = 1/3$ is the limit of a rectangular shaped response.

2.4 Dynamics and rheological properties of polymer melts

In the current section, the focus is on polymer relaxation processes on a molecular level. In contrast 2.3 *Rheology* does not consider any molecular properties. The rheological response is a result of the interactions of the polymer chains, which are long molecular, in the molten state. After giving a basic description of polymers in melt, the most important relaxation mechanisms are introduced. For the sake of simplicity, monodisperse systems are assumed.

A polymer chain has a certain molecular weight, as introduced in Equation 2.1. Since it is a molecule, the orbitals, the bond length and its own volume limit its possible conformations. A length scale is introduced, which equals a quasi element which would be freely adjustable. This is called *Kuhn length* l_K.[36] Consequently, a chain consist of N_K Kuhn elements ($N_K = l_{total}/l_K$, with l_{total} being the total length of a chain, also called *contour length*). Assuming that there is no self volume and no interaction between chain parts, the chain conformation can be approximated with a Gaussian-walk with a fixed step length. This conformation is realized in a so-called θ-solvent or within a polymer melt.

The mean end-to-end distances h are defined in Equation 2.39 and Equation 2.40.[36]

$$< \vec{h} > = \vec{0} \tag{2.39}$$

$$< \vec{h}^2 > = N_K \cdot l_K^2 \tag{2.40}$$

$$\sqrt{< \vec{h}^2 >} = \sqrt{N_K} \cdot l_K \tag{2.41}$$

$< \vec{h} >$ is not a suitable parameter to characterize a mean end to end vector, since the choice of the start and end of the vector is arbitrary (and the conformation is random), therefore, the sum is zero. Therefore, the squared mean value is used.

Table 2.1. Table of relevant length scales. [36]
*): please note that two definitions for the contour length exist. The first one sums up the path along all covalent bonds. The second one is the length is of a maximal stretched polymer chain, while assuming physical reasonable angles of the covalent bonds. The second definition results in shorter contour lengths.

symbol	name	approx. dimensions	equations
M_0	monomer length	$\lesssim 1\,\mathrm{nm}$	
l_K	Kuhn length	$\approx 1\,\mathrm{nm}$	
l_e	length between entanglements	$\approx 10\,\mathrm{nm}$	M_e/M_0
a	tube diameter	$\gtrsim 1\,\mathrm{nm}$	
l_{tube}	tube length	$\approx 100\,\mathrm{nm}$	
$l_{contour}$	contour length[*)]	$\approx 100\,\mathrm{nm}$	M_n/M_0
$|\vec{h}|$	end to end vector	$\approx 10\,\mathrm{nm}$	

2.4.1 Relaxation modes

The following section describes the local motions and relaxation processes in a well entangled polymer melt on different time and length scales.

Tube reptation

As introduced earlier (in 2.4 *Dynamics and rheological properties of polymer melts*, p. 25), the conformation of a polymer chain in melt can be approximated with an Gaussian-coil. The free volume of this coil is filled with other polymer chains. This model leads to contact points between chains, which restrict the motion of the chain in focus. In the tube model these sidewise restriction form a quasi tube (refer to Figure 2.18), in which the motion along the tube is unrestricted. In contrast to that, the movement perpendicular to the tube is fully restricted. The chain is longer than the tube, since it is wrinkled. The diameter of this tube is called tube diameter a and is much smaller than the length of the tube, but bigger than a Kuhn length l_K.[36]
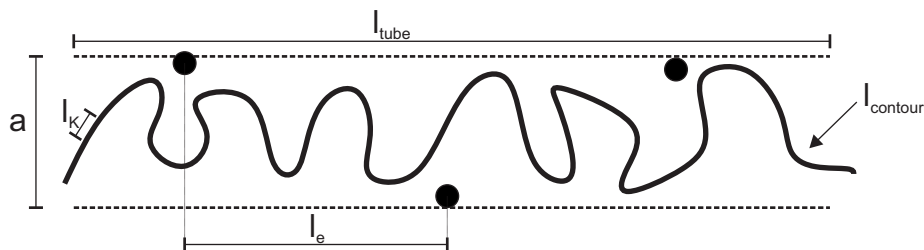
Figure 2.18. Linear projection of a polymer chain in a 'tube'. The chain is restricted by neighbor chains, confining it in its tube. The chain is wrinkled with a total length of $l_{contour}$. The tube confinements are illustrated by the parallel dotted lines, its length is l_{tube}. The black dots indicate entanglement points perpendicular to the paper-plane, the distance between two entanglements is l_e. The approximate Kuhn length l_K is added as well. In this model it is assumed, that the confinements are fixed, while the chain is mobile within the tube.

The tube model assumes that a chain is confined in a restrictive tube as in Figure 2.18. This restrictions are set by other chains, which are assumed to be fixed in a first approximation (for a second approximation, refer to 2.4.1 *Double reptation*, p. 27). It is demonstrated within this section, that the relaxation time is proportional to the chain length to the third power.

The chain can move unhindered along the tube in a statistical manner (back and forth movement is allowed!). This diffusion has a mean displacement $\vec{d}$ of

$$\sqrt{<\vec{d^2}>} = \sqrt{n \cdot 2Dt} \tag{2.42}$$

$$n = 1 \tag{2.43}$$

where D is the diffusion coefficient, t is the time and n is the dimensionality. By realigning this equation Equation 2.44 is obtained.

$$\tau_d \propto L_{tube}^2 \tag{2.44}$$

Where τ_d is the time t that the chain need to leave its tube (with the condition $\sqrt{<\vec{d^2}>} = l_{tube}$). Moreover, the diffusion is driven by thermal energy $k_b T$ and the velocity restricted by friction that is quantified by the friction coefficient ζ. The ζ is the degree of polymerization P_n times the monomeric friction coefficient ζ_0 and related to the diffusion coefficient shown in Equation 2.45 and Equation 2.46.[36]

$$\zeta = \zeta_0 \cdot P_n = \zeta_0 \cdot M_n/M_0 \tag{2.45}$$

$$D = \frac{k_b T}{N_k \zeta_0} \propto M_n^{-1} \tag{2.46}$$

Since the tube length is proportional to the degree of polymerization $L_{tube} \propto P_n$, the longest relaxation time has scaling exponent to P_n of the third power:

$$\eta \propto \tau_d \propto P_n^3 \propto M_n^3 \tag{2.47}$$

Contour length fluctuations

The contour length or primitive path is the modeled length of the observed polymer. However, practically this length is changing with time, by wrinkling the chain in the dynamic tube. This effect is know as *contour length fluctuations* or *primitive path fluctuations*. For further details, the reader is referred to the literature.[26]

Double reptation

In the tube model it is assumed that the tube of the chain on the paper plane has fixed restrictions. In a more detailed model, these 'restrictions' are chains confined in their own tube, which is simplified as being orthogonal to the paper plane, as referred to in Figure 2.18. The 'restriction' of the tube in the paper plane is disentangled if a chain, which acts as a restriction, diffuses out of this entanglement. This effect is called *double reptation*.[26] For non-monodispese systems, this process is even more important, since the relaxation of a long chain is stronger influenced by the relaxation of small chains .[14]

Segmental relaxation

The relaxation was described for a full chain. A chain consists of many (Kuhn) segments, and has many segments between entanglements. Their relaxation is described in the current paragraphs:
The relaxation time of the smallest (theoretical) segment - the *Kuhn segment* - is named τ_s and is defined as in Equation 2.48 and Equation 2.49.

$$\tau_s = \frac{l_K^2 \zeta_s}{3\pi^2 k_B T} \tag{2.48}$$

$$\zeta_s = l_K/l_{monomer}\zeta_0 \tag{2.49}$$

---

[14]The long chain fraction is dominating the longest relaxation time/zero-shear viscosity of the system.

Consequently, the relaxation time for a distance of in between two entanglements (τ_e) is given in Equation 2.50.

$$\tau_\mathrm{e} = \tau_s \cdot N_\mathrm{e}^2 \tag{2.50}$$

with N_e (also symbolized with Z) as the number of segments between two entanglements.

Rouse relaxation

The Rouse model describes the relaxation of free (unentangled) chains(-segments).[36, 37] In summary, it relates the different possible modes of a polymer chain to a relaxation process. For details the reader is referred to literature [36, 38, 39]. The longest Rouse relaxation time is given by Equation 2.51

$$\tau_R = N_k^2 \tau_s \tag{2.51}$$

with N_k as the number of Kuhn segments.

2.5 Nuclear magnetic resonance (NMR) spectroscopy and relaxometry

This section is an introduction into nuclear magnetic resonance (NMR), where the focus lies on NMR-relaxometry.[15] For further elaborations the reader is referred to literature such as the book of Blümich [40], which is suitable for beginners or from Schmidt-Rohr and Spiess [41], which requires foreknowledge. Electromagnetic waves in the radio frequency range interact with the magnetic momentum of nuclei - this phenomena is call nuclear magnetic resonance.

Many isotopes possess a quantum mechanical spin or angular momentum $I \neq 0$, more precisely all nuclei with an uneven number of protons and/or an uneven number of neutrons. An overview of the important nuclei is presented in Table 2.2. In the most relevant and most simple case of Hydrogen[16] (^{1}H), also referred to as *proton* or *protium*, the spin equals to $I = 1/2$. The spins quantize into $2I + 1$ discrete energy levels in an external magnetic field $\vec{B}_0$, with their respective Eigenvalues $E = m_I \hbar \gamma B_0$. In the case of ^{1}H, these Eigenvalues (m_I) equal to $m_I = \pm 1/2$. Relevant to this work is the NMR spectroscopy on protons and deuterons. Moreover, as a side effect, the T_1 reducing phenomenon exhibited by the free electrons in radicals and oxygen is observed within this work, too.

Table 2.2. Examples of relevant NMR nuclei and their natural abundance, spin and γ [40, 42].

nuclei	natural abundance [%]	spin I	gyromagnetic ratio γ [10^8 rad s^{-1} T^{-1}]
^{1}H	99.99	1/2	2.675
^{2}H	0.01	1	0.411
^{13}C	1.07	1/2	0.673
^{15}N	0.36	1/2	1.913
^{19}F	100.00	1/2	2.517
^{29}Si	1.07	1/2	0.532
^{31}P	100.00	1/2	1.083
e^- a)	-	1/2	1 760

a) for comparison, the electron, which is obviously no nuclei, yet the electron spin resonance is driven by the very same principles as NMR spectroscopy. This technique only works for unpaired electrons, such as stable radicals.

The interactions in a spin system can be described using a Hamiltonian $\hat{H}$ as a sum of its respective interactions [43]:

$$\hat{H} = \hat{H}_Z + \hat{H}_{\text{rf}} + \hat{H}_Q + \hat{H}_D + \hat{H}_\delta + \hat{H}_J \tag{2.52}$$

---

[15]Characterizations in the frequency domain are referred to as NMR-spectroscopy, while the term NMR relaxometry is employed when analyzing in the time domain. This difference is not distinct, and both fields can be combined.

[16]In nature hydrogen consists of 2 isotopes. While *protium* (^{1}H) makes up for the majority, *deuterium* (^{2}H) has little natural abundance. To circumvent confusion, the term hydrogen is hereon avoided and the precise synonyms are being used. More details on natural abundances in Table 2.2.

with $\hat{H}_Z$, $\hat{H}_{\text{rf}}$, $\hat{H}_Q$, $\hat{H}_D$, $\hat{H}_\delta$ and $\hat{H}_J$ representing the Hamiltonians of their respective interactions, namely Zeeman Interaction, radio frequency pulses, quadrupolar interaction, dipolar interaction, chemical shift interaction and J-coupling. These interactions are specified in their corresponding sub-chapters. The Hamiltonians $\hat{H}$ are normalized to $\hbar$ (reduced Planck constant) as it is 'convenient and common in the NMR literature' [41].

2.5.1 Zeeman interaction

The Zeeman Hamiltonian $\hat{H}_Z$ is defined as in Equation 2.53, with the static magnetic field $\vec{B}_0$, the gyromagnetic ratio γ and the spin vector operator fraction parallel to the z-axis $\hat{I}_z$.[41, 43]

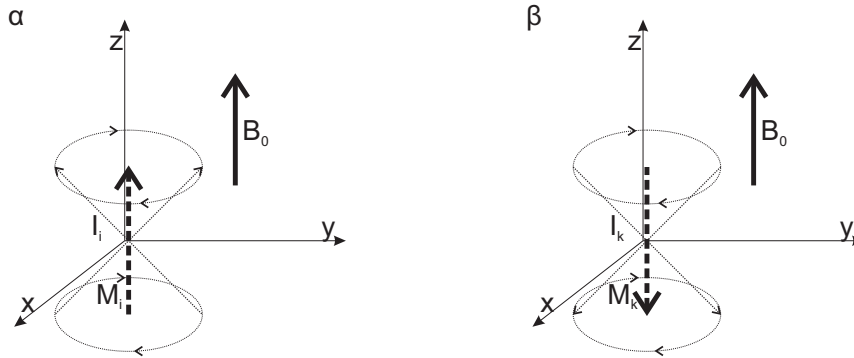$$\hat{H}_Z = -\gamma \hat{I}_z B_0 \tag{2.53}$$

Figure 2.19. Two possible states of nuclei, α and β, with $I = 1/2$. The spin precesses around $\vec{B}_0$. $\vec{M}_i$ is the resulting magnetization of a single spin. The antiparallel state β has a smaller resulting magnetic moment compared to α. The spins are not localized, which is illustrated by two vectors.

NMR, in general, deals with the interaction of spins in an external magnetic field $\vec{B}_0$. In this field the spins $\vec{I}$ can be aligned as depicted in Figure 2.19. The alignment of the resulting magnetization of the ensemble is discussed later. The spins precess parallel or antiparallel to $\vec{B}_0$. When put into a $\vec{B}_0$ field, both states are no longer degenerate. This phenomenon is referred to as the Zeeman-effect. The spins precess with a characteristic *Lamor* frequency[17] (ω_L) which depends on the amplitude of the magnetic field[18] B_0 and the respective gyromagnetic ratio γ of the nuclei, refer to Equation 2.54.

$$\omega_L = \gamma B_0 \tag{2.54}$$

The energy difference (ΔE) between to states is given by Equation 2.55.

$$\Delta E = h\nu = \hbar\omega_L = \hbar\gamma B_0. \tag{2.55}$$

---

[17]Values for $\omega_L/(2\pi)$ range between $\sim 10\,\text{MHz}$ and $1200\,\text{MHz}$ [Bruker2019] for protons in typical spectrometers ($B_0 = 0.2\,\text{T}$ to $28\,\text{T}$). For different nuclei with a lower γ proportionally lower.

[18]Absolute values of vectors are displayed as their analogs without the vector arrow, *e.g.,* $B_0 = |\vec{B}_0|$.

The energy difference between the states lead to a difference in population, which can be described in the equilibrium state with the Boltzmann distribution:

$$\frac{N_{+1/2}}{N_{-1/2}} = \exp(\frac{-\Delta E}{k_B T}) \approx 1 - \frac{\Delta E}{k_B T} = 1 - \frac{\hbar \omega_L}{k_B T} \tag{2.56}$$

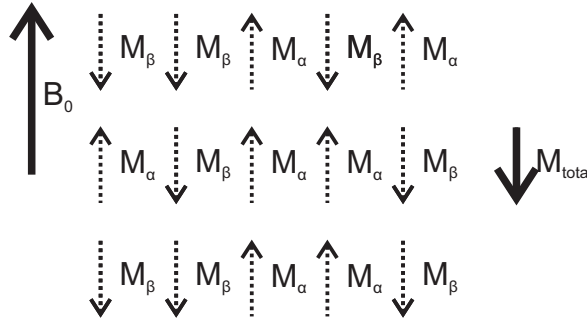Herein T is the absolute temperature, k_B is the Boltzmann constant and $N_{+1/2}/N_{-1/2}$ is the population ratio[19].

Figure 2.20. The population of the α and β states are described with the Boltzmann distribution. Since the energy difference is low, the difference in population is minuscule. The resulting magnetization is $\vec{M_{total}} = \vec{M}$.

The difference in population leads to a net magnetization $\vec{M} = \vec{M_{total}}$ antiparallel to $\vec{B}_0$ as illustrated in Figure 2.20. Instead of using a static Cartesian coordinate system with $\vec{x}, \vec{y}$ and $\vec{z} \parallel \vec{B}_0$, a rotating coordinate system with $\vec{x}', \vec{y}'$ and $\vec{z}' = \vec{z} \parallel \vec{B}_0$ is utilized, where the rotation of the system occurs around the z-axis with an angular frequency ω_L (see Figure 2.21).
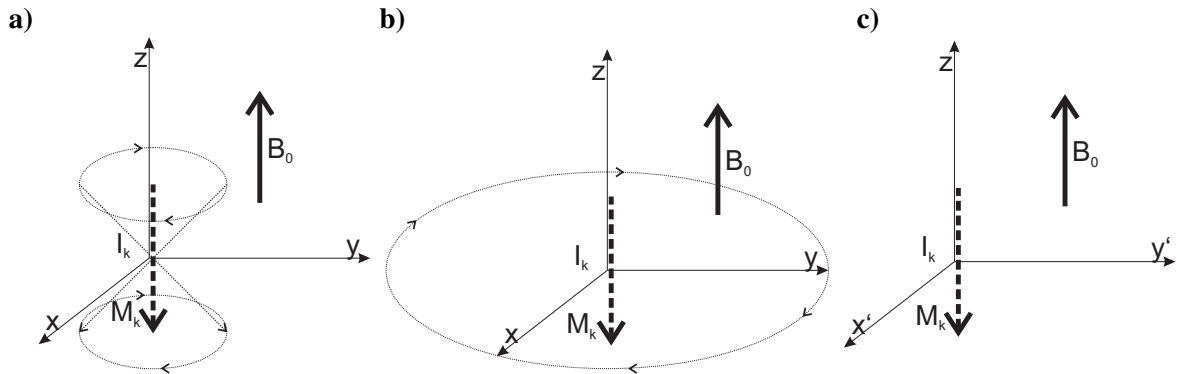
Figure 2.21. The rotating coordinate system is introduced.
a) The rotation of the spins occurs around $\vec{z}$ axis with ω_L.
b) The x,y-plane rotates with ω_L around $\vec{z}$ resulting in a static spin in this rotating frame.
c) These rotating axis are named $\vec{x'}$ and $\vec{y'}$.

---

[19]In this thesis a 20 MHz spectrometer was used. Consequently, the lower energy state has an excess population of $(N_{-1/2} - N_{+1/2})/(N_{-1/2} + N_{+1/2}) = 1.59$ ppm.

2.5.2 Radio frequency pulse

The radio frequency pulse (rf) Hamiltonian $\hat{H}_{rf}$ is defined as in Equation 2.57, with γ as the gyromagnetic ratio, $\hat{I}_{x,y}$ as spin vector operator and the oscillating electromagnetic field (rf pulse) $\vec{B}_1$ presented.[43]

$$\hat{H}_{\text{rf}} = -\gamma \hat{I}_{x,y} \vec{B}_1 \tag{2.57}$$

An applied electromagnetic wave can be used manipulate the spin system. If a nuclei is irradiated with a wave which equals its Lamor frequency

$$\omega_{\text{rf}} = \omega_L, \tag{2.58}$$

resonance occurs. In typical experiments the rf pulses are very short (*e.g.,* 1 µs *to* 20 µs) and therefore their frequency distributions cover a broad range, which is sufficient to excite all targeted nuclei.[20] To illustrate the interaction between the rf-pulse and the spins, the rotating coordinate system is being used as introduced in the last sub section. Since this coordinate system rotates with ω_L and Equation 2.58 applies, the rf pulse can be described as a quasi static magnetic field in this coordinate system.[21] The rf pulse can be applied from any position which is a linear combination of $\vec{x}'$ and $\vec{y}'$.[22] When an rf pulse is applied to the spins, the net magnetization $\vec{M}$ rotates along the axis of the applied $\vec{B}_1$ field.[23] This phenomenon is known as *Rabi cycle* (German: *Rabi-Oszillation*). This rotation increases the proportion of $\vec{M}$ in the x-y plane, which reaches its maximum after 90°. The rf-pulse is illustrated in Figure 2.22. While the magnetization is rotating with ω_L around $\vec{z}$, the magnetization is rotating towards the x,y-plane with ω_1.
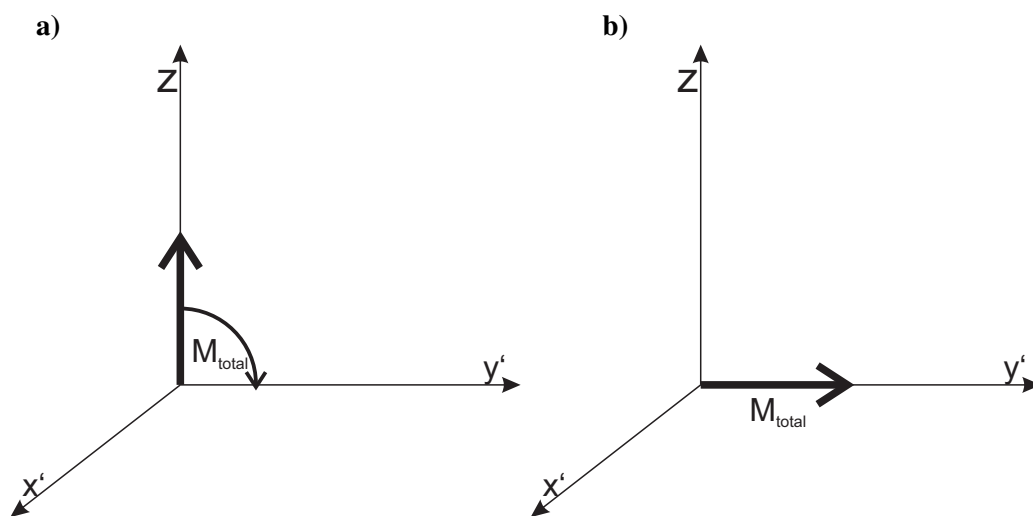
Figure 2.22. Illustration of a 90° rf-pulse in the rotating frame. **a)** The rotation is around $\vec{y'}$, therefore, it is called a 90°-y pulse. **b)** The magnetization is fully in the x,y-plane more precisely fully on the $\vec{x'}$ axis.

---

[20] this is true for ^{1}H and ^{2}H; for ^{19}F the excitation can be heterogeneous.

[21] In the lab coordinate system it is still an oscillating wave.

[22] While $\vec{x}' \perp \vec{y}'$, the position of $\vec{x}'$ is arbitrary.

[23] A full rotation along the $\vec{B}_1$ takes ≥ 10 µs for instruments used in this work, therefore, its resulting frequency of the turning of the spins is $\omega_1/(2\pi) \leq 100$ kHz. Note that this is the rotation along the $\vec{B}_1$ field and the spins still precess around $\vec{B}_0$ with ω_L.

Multiple pulses with variable evolution times in between can be applied from different positions in the x-y plane. This allows the possibility for a tremendous amount off different experiments of the same sample in the same instrument.

After or in between pulses, the spins undergo evolution processes due to different interactions. The relevant interactions are explained in the following subsections 2.5.3 to 2.5.6. An illustration of the evolution/dephasing is shown in Figure 2.23.
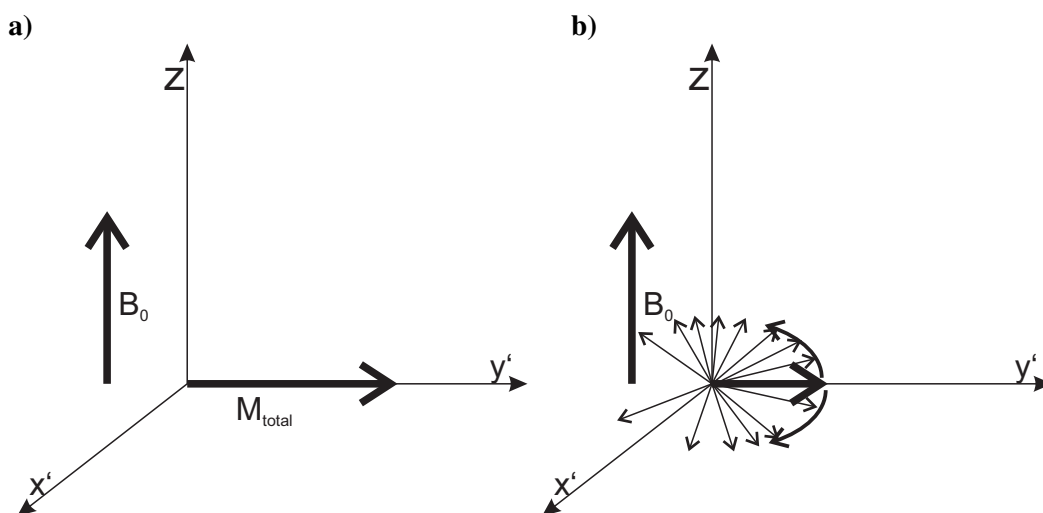

Figure 2.23. a) After a rf-pulse as in Figure 2.22, the magnetization is rotated in to the x,y-plane. **b)** The dephasing of the magnetization $\vec{M}_i$ of the spins after a certain evolution time. While the dephasing progresses the absolute value of $\sum_i \vec{M}_i = \vec{M}$ decreases.

2.5.3 Dipolar coupling

The dipole-dipole interaction Hamiltonian $\hat{H}_D$ as in Equation 2.60, with $\gamma_{i,j}$ as the gyromagnetic ratio(s) ($\gamma_i = \gamma_j$ for homonuclear dipolar coupling), $\hat{I}_{i,j}$ as spin vector operators and $\mathbf{D}$ as the coupling tensor. The trace (German: *Spur*) of $\mathbf{D}$ is zero, therefore, this interaction averages to zero for fast tumbling molecules such as isotropic liquid and solutions.[43]

$$\hat{H}_D = -\frac{\mu\gamma_i\gamma_j}{4\pi}\hat{I}_i\mathbf{D}\hat{I}_j \tag{2.59}$$

$$= -\frac{\mu\hbar\gamma_i\gamma_j}{4\pi r^3} \cdot \left[\frac{1}{2}(3\cos^2(\theta)-1)\right](3\hat{I}_{z,i}\hat{I}_{z,j} - \hat{I}_i\hat{I}_j) \tag{2.60}$$

$$\frac{1}{3}Sp\{\mathbf{D}\} = 0 \tag{2.61}$$

As explained in 2.5 *Nuclear magnetic resonance (NMR) spectroscopy and relaxometry*, p. 29, NMR-relevant nuclei exhibit a spin. This spin results in a magnetic dipole and/or a quadruple. Herein this

section, the focus lies on dipole-dipole interactions the *dipolar coupling*. The spins are indexed by i and j. To describe an ensemble of spins, the sum of all permutations with $i \geq j$ has to be made.

The coupling frequency ω_D depends on the gyromagnetic ratios γ_i, γ_j, the distance between the 2 spins $r_{i,j}$ and the angle θ between $\vec{B}_0$ and $\vec{r_{i,j}}$[41]:

$$\omega_D/(2\pi) = \frac{\mu_0}{4\pi}\hbar\frac{\gamma_i\gamma_j}{r_{i,j}^3} \cdot \frac{1}{2}(3\cos^2(\theta) - 1) \tag{2.62}$$

With the values for ^{1}H and theoretical distance of 1 Å the resulting frequency is given by Equation 2.63.[41]

$$\omega_D/(2\pi) = 122\,\text{kHz} \cdot \frac{1}{2}(3\cos^2(\theta) - 1) \tag{2.63}$$

Other distances can be obtained by dividing this value by the 3$^{\text{rd}}$ power of the relative distance, *e.g.,* 1.8 Å:

$$\omega_D/(2\pi) = \frac{122\,\text{kHz}}{(1.8\,\text{Å}/\text{Å})^3} \cdot \frac{1}{2}(3\cos^2(\theta) - 1) = 20.9\,\text{kHz} \cdot \frac{1}{2}(3\cos^2(\theta) - 1) \tag{2.64}$$

The frequency value of 20.9 kHz denotes the maximum coupling frequency between protons, assuming that 1.8 Å is the minimum distance between protons in a molecule. The dipolar coupling in a static system can positive or negative, depending on the second factor $\frac{1}{2}(3cos^2(\theta) - 1)$.

In real system, even in some solids, the angle θ fluctuates, resulting in dipolar couplings being averaged over the experimental time frame. The reduced rest coupling is called residual dipolar coupling D_{res}. If one averages the term $\frac{1}{2}(3cos^2(\theta) - 1)$ by integrating over all possible θ and the respective probability of a specific θ assuming a spherical surface, the D_{res} is averaged to 0 kHz. Therefore, no dipolar coupling is observed in systems that have fast isotropically tumbling molecules, such as solutions.

2.5.4 Quadopolar interaction

The quadrupolar coupling Hamiltonian $\hat{H}_Q$ is defined as in Equation 2.66, with the quadrupolar moment tensor $\mathbf{Q}$, the spin vector operators $\hat{\vec{I}}_{i,j}$, elemental charge e, the total spin I, the reduced Planck' constant $\hbar$, the quadrupolar moment Q and the field gradient V[41, 43].

$$\hat{H}_Q = \frac{eQ}{2I(2I - 1)\hbar}\hat{\vec{I}}_i\mathbf{Q}\hat{\vec{I}}_j \tag{2.65}$$

$$= \frac{eQV}{2I(2I - 1)\hbar}\frac{1}{2}(3\hat{I}_{z,i}\hat{I}_{z,j} - \hat{I}_i\hat{I}_j) \tag{2.66}$$

$$\frac{1}{3}Sp\{\mathbf{Q}\} = 0 \tag{2.67}$$

Nuclei with a spin $I \geq 1$ are subject to an electric field tensor and therefore exhibit a quadrupolar moment Q. The respective Hamiltonian has already been shown in Equation 2.66. For nuclei with a spin of $I = 1/2$ like protium this interaction is zero. In a solid (without averaging) the quadrupolar interaction frequency for deuterons is $\omega_{Q,{}^2\text{H}}/(2\pi) \approx 130\,\text{kHz}$ and therefore stronger than the dipolar interaction. Fast

motion like tumbling of small molecules or spinning of chemical groups pre-averages the interaction to a certain extent. Deuteron ^{2}H NMR spectroscopy in a liquid like (deuterated) chloroform can be performed in a similar fashion to ^{1}H NMR spectroscopy, but the peaks are broadened by a significant extend. In case of other nuclei such ash ^{14}N, the interaction is stronger than the rf-pulse and therefore not possible to record. For further information about this interaction, the reader is referred to the literature[41, 43].

2.5.5 Chemical shift

The chemical shift Hamiltonian $\hat{H}_\delta$ is defined as in Equation 2.68, with the gyromagnetic ratio γ, the spin vector operator $\vec{\hat{I}}$, the shielding tensor $\hat{\sigma}$, the magnetic field $\vec{B}_0$ and δ' as the trace of the shielding tensor δ.[41, 43]

$$\hat{H}_\delta = \gamma \vec{\hat{I}} \hat{\vec{\delta}} \vec{B}_0 \tag{2.68}$$

$$\frac{1}{3} Sp\{\delta\} = \delta' \tag{2.69}$$

The nuclei in atom and molecules are influenced by their electron shell. In case of protium this interaction is mostly an anti-parallel magnetic field, which is induced by the influence of a magnetic field on electrons in theirs orbitals. This induced field is in good approximation proportional to the electron density around the monitored nuclei. Electron withdrawing or pushing groups influence the shielding strength. Therefore, the resulting magnetic field for each (type of) nuclei is different (refer to Equation 2.70). While in liquids the averaged isotropic chemical shift is observed, the chemical shift in solids is anisotropic. Equation 2.70 describes the relationship between the external magnetic field and the resulting magnetic field.

$$B_{0,i} = (1 + \delta_i) \cdot B_{0,ref} \tag{2.70}$$

with the B_0 field for an indiviual nuclei $B_{0,i}$, the proportionality factor δ_i (which is called *chemical shift*) and the B_0 field strength for the reference substance (Tetramethylsilane for ^{1}H) $B_{0,ref}$. By combining equations 2.54 and 2.70, different Lamor frequencies for each type of nuclei as shown in Equation 2.71 are found.

$$\omega_{L,i} = (1 + \delta_i) \cdot \omega_{L,ref} \tag{2.71}$$

This interaction is proportional to the external magnetic field:

$$\delta_i \propto B_0 \tag{2.72}$$

To compensate for different fields in different spectrometers the chemical shift is typically normalized to the reference frequency (refer to Equation 2.73), as such the chemical shift can be derived from Equation 2.70.

$$\delta_i = \frac{B_{0,i} - B_{0,ref}}{B_{0,ref}} = \frac{\omega_{L,i} - \omega_{L,ref}}{\omega_{L,ref}} \tag{2.73}$$

Different δ_i can be recorded in the most simple experiment including a 30° or 90° pulse, followed by acquisition of the resulting impulse response/free inductive decay. The chemical shift is a very important observable for structure analysis and is widely used in structure analysis or reaction control. The interaction is averaged over the experiment, therefore, fast moving/flipping molecules like cyclohexane show a uniform, so called *isochrone*, shifts. Functional groups that undergo a flip or chemical reaction, like proton/proton-exchange in acid groups, are subject to line broadening. Practically the chemical shift is obtained after Fourier-transformation of the FID. The resulting Fourier transformed spectrum shows peaks at the designated frequencies, which is typically normalized to ω_L as in Equation 2.73.

Since the chemical shift is mostly related to the electron shell, the difference in chemical shifts for protons and deuterons is small.

2.5.6 J-Coupling

The J-coulpling Hamiltonian $\hat{H}_J$ is defined as in Equation 2.75, with $\hat{\vec{I}}_i$ and $\hat{\vec{I}}_j$ are the spin vecor operators and **J** is the J-coupling tensor. The trace is J, this implies for fast motions the absolute value for J is retained.[41, 43]

$$\hat{H}_J = \hat{\vec{I}}_i \mathbf{J} \hat{\vec{I}}_j \tag{2.74}$$

$$= -2\pi J(\hat{\vec{I}}_i \cdot \hat{\vec{I}}_j) \tag{2.75}$$

$$\frac{1}{3} Sp\{\mathbf{J}\} = J \tag{2.76}$$

J-coupling is an interaction through chemical bonds of two not isochrone nuclei. The range is in first approximation limited to the next not isochrone nuclei. Typical couping strenghts are about 120 Hz for ^{13}C satellites and 10 Hz for proton proton interaction. This interaction allows for a deep insight into the neighbor atoms of protons in liquid NMR measurements.

2.5.7 Relaxometry and NMR relaxation

Until now, the interaction between spins were described, including their respective interaction frequencies. The interactions can be described with their respective frequencies, however, experiments are done in the time domain.

In 1948, [44] N. Bloembergen, E. M. Purcell, and R. Pound explained the relaxation rates in the z-direction (*longitudinal relaxation*, T_1-*relaxation*) and the x-y plane (*transverse relaxation*, T_2-*relaxation*), which is known as the BBP-theory. The T_1-rate is the relaxation time that is required to reach the equilibrium state as described 2.5.1 *Zeeman interaction*, p. 30. The T_2-rate is the relaxation time in which spin-spin interaction reduce the observed magnetization $|\vec{M}_{x,y}|$. The theory introduces the correlation time τ_c of small fluctuations in the magnetic field. The relations are presented in Equations 2.77 and 2.78. For completeness, Equation 2.79 presents the relaxation time in systems with spin lock, which is the relaxation in a rotating magnetic field.[43]

$$1/T_1 = \frac{4}{15r^6}(\frac{\mu_0}{4\pi})^2\gamma^4\hbar^2 I(I+1) \cdot \frac{3}{2}\left[1\frac{\tau_c}{1+\omega_L^2\tau_c^2} + 4\frac{\tau_c}{1+4\omega_L^2\tau_c^2}\right] \tag{2.77}$$

$$1/T_2 = \frac{4}{15r^6}(\frac{\mu_0}{4\pi})^2\gamma^4\hbar^2 I(I+1) \cdot \frac{3}{2}\left[6\underbrace{\frac{\tau_c}{1+0\cdot\tau_c^2}}_{\omega=0} + 5\frac{\tau_c}{1+\omega_L^2\tau_c^2} + 4\frac{\tau_c}{1+4\omega_L^2\tau_c^2}\right] \tag{2.78}$$

$$1/T_{1\rho} = \frac{4}{15r^6}(\frac{\mu_0}{4\pi})^2\gamma^4\hbar^2 I(I+1) \cdot \frac{3}{2}\left[6\frac{\tau_c}{1+\omega_{lock}^2\tau_c^2} + 5\frac{\tau_c}{1+\omega_L^2\tau_c^2} + 4\frac{\tau_c}{1+4\omega_L^2\tau_c^2}\right] \tag{2.79}$$

To observe a system in equilibrium a recycle delay between two experiments of $rd = 5 \cdot T_1$, which amounts to $> 99\,\%$ relaxation, is typically employed.

To acquire T_2 and $T_{1\rho}$, XY-16 and CPMG (Carr–Purcell–Meiboom–Gill)-pulse trains can be used, respectively.[45–47]

2.5.8 Multiquantum coherence

The current section deals with multiquantum coherence, which is not observable with a single pulse, in contrast to single quantum transitions. In this section, the problem is reduced to a two spin system, but the applied reasoning can be expanded to a multi spin system.

2.5 *Nuclear magnetic resonance (NMR) spectroscopy and relaxometry*, p. 29, describes that a single proton in an external magnetic field can have two spin states, namely α and β. The only possible transition is back an forth between these two state, a single quantum (SQ) transition. The current state can be detected with, e.g., a 90° pulse.

In the case of $n = 2$ coupled nuclei, the spin state of nuclei i is affected by the spin state of nuclei j. The possible transitions are displayed in Figure 2.24.
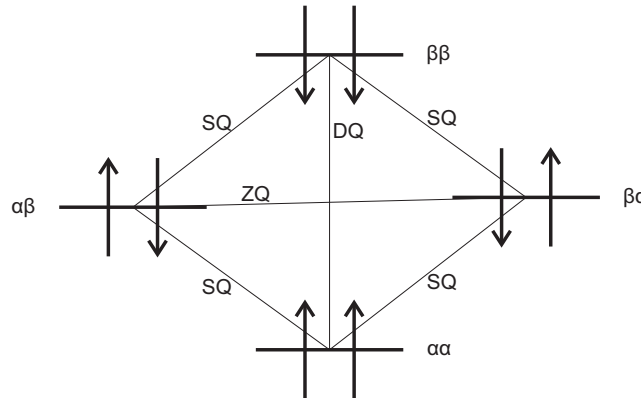

Figure 2.24. A two spin system with its possible transitions. The two spins states are not degenerated and named i and j. The possible transitions are 4 permutations of single quantum (SQ) transition, double quantum (DQ) transition or zero quantum (ZQ) transition.[48]

For the most common transition, the SQ transition, magnetization is generated in the x,y-plane. In case both spins change their state simultaneously, either a zero quantum (ZQ) transition (for $I_i + I_j = 0$) or

double quantum (DQ) transitions (for $|I_i + I_j| = 1$) is induced. In contrast to SQ, DQ and ZQ transition do not result in magnetization in the x,y plane and therefore, are not directly observable. Nevertheless, the DQ transition is observable in an indirect way: First, a single quantum process is required. Second, an evolution period is applied, which allows for the coupling between the spins. And third, the generation of the DQ-coherence with a second pulse is required.

Typically a train of pulses is used to compensate for different perturbations. A common sequence is the Baum Pines (BP) sequence, which consists of 24 pulses, not counting the detection pulse. The sequence is elaborated in Figure 2.25.[49–54]
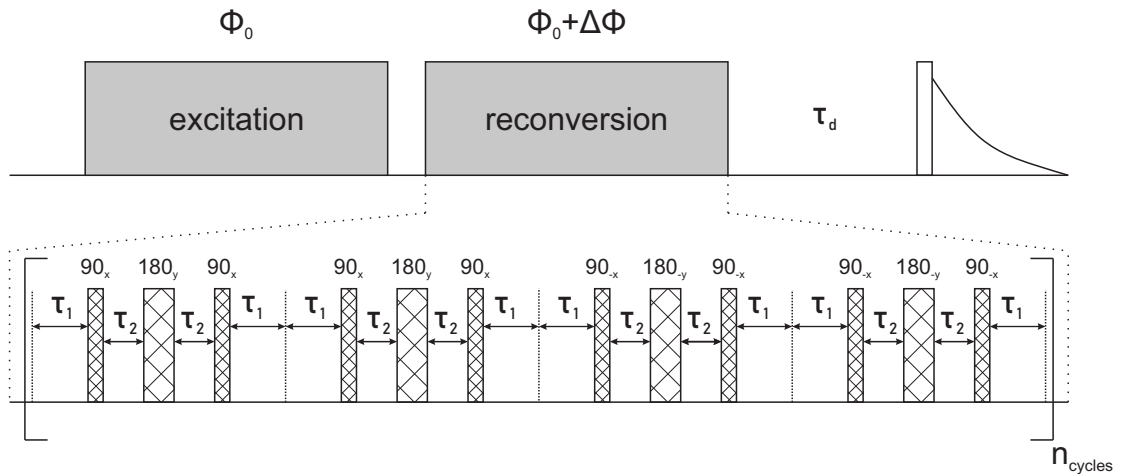

Figure 2.25. Modified Baum Pines sequence. The experiment allows for the quantification of the double quantum coherence. The reference and the double-quantum contributions are evolving in a way, that their signals are orthogonal in the FID. The acquisition of the respective contributions can be quantified with an FID with the correct phase. The sequence can be applied with $n \geq 1$ cycles. The DQ-mixing time τ_{DQ} can be varied by choosing different times between the pulses, which are τ_1 and τ_2. The relation is as follows: $\tau_1 = \tau_{DQ}/24 - \tau_{90}/2$ and $\tau_2 = \tau_{DQ}/12 - 3 \cdot \tau_{90}/2$, where τ_{90} is the length of a 90° pulse. Double quantum selection is performed using a four-step phase cycle for the carrier phase (Φ_0) of the reconversion period ($\Delta\Phi = \{0°, 90°, 180°, 270°\}$) while inverting the receiver phase for alternating scans.[51]

2.6 Chemistry of protons and deuterons

Hydrogen has two relevant isotopes in nature, protium and deuterium. In first approximation different isotopes show no difference in chemical reaction, since chemical reactions involve interactions of the electron shells, and the weight of the nuclei are of minor importance.

In a more detailed inspection, one find small differences in reactivity between different isotopes. On the one hand, there are differences in the mass and the vibration modes, and on the other hand, tunneling processes are of significant relevance for many chemical processes. The differences result in different reaction speeds for protons and deuterium, and slightly different chemical bond length. As a result, the chemical shifts of protons and deuterium are very similar, yet there is a deviation, which is more pronounced in systems, where the hydrogen is close to a double bond.

Concerning synthesis, deuterium can be enriched. There are two processes of importance: electrolysis and the Gridler (hydrogen) sulfide (GS) process. Practically, the residual water of electrolysis processes is used as an ingredient for the GS-process. The GS process is elaborated in Figure 2.26.[55] The price for 1 kg of D_2O is approximately 500 € (year 2020).
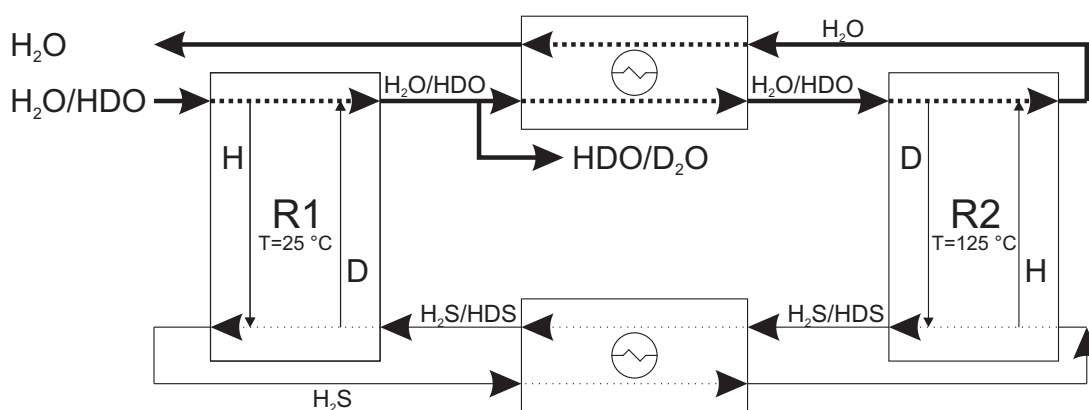

Figure 2.26. Scheme for deuterium enrichment using the Gridler sulfide (GS) process. The process features two reactors. The first reactor (R1) is cold (25 °C). It contains enriched HDS and transfers deuterium to water, which enriches the water and depletes the hydrogen sulfide. In a second reactor (R2) which at elevated temperatures (125 °C), hydrogen sulfide is enriched with deuterium and water is depleted. Enriched water can be drained after the first reactor. ⊖ represents a heat exchanger, the thick line symbolize the water flow, and the thin line the hydrogen sulfide flow. Scheme adapted from [55].

Typically protonated and deuterated substances mix well with each other. Only in systems where the mixing entropy is very low, phase separation can be observed (for example PS-block-(per-deuterated)-PS, for molecular weights much above 1 000 000 g/mol)).[56]

3 Anionic polymerization, synthesis of deuterated isoprene and polymer purification

3.1 Overview of the synthetic methods

The current chapter deals with the synthetic methods which have been applied in this work. While details on specific steps such as the monomer purification and the full characterization are presented in 11 *Appendix*, p. 114, the current chapter gives the important key features of the monomer and polymer synthesis. A theoretical introduction to anionic synthesis is found in 2.2 *Living anionic polymerization* p. 6 and represents the basis for the following chapter. In Figure 3.1, an overview on the intertwinement of the respective synthesis and purification methods is presented.

The focus is of this thesis is the characterization of well defined polymer model systems. On the one hand, the topology is defined, and on the other hand, polymer model systems have been isotopically labeled with deuterium.
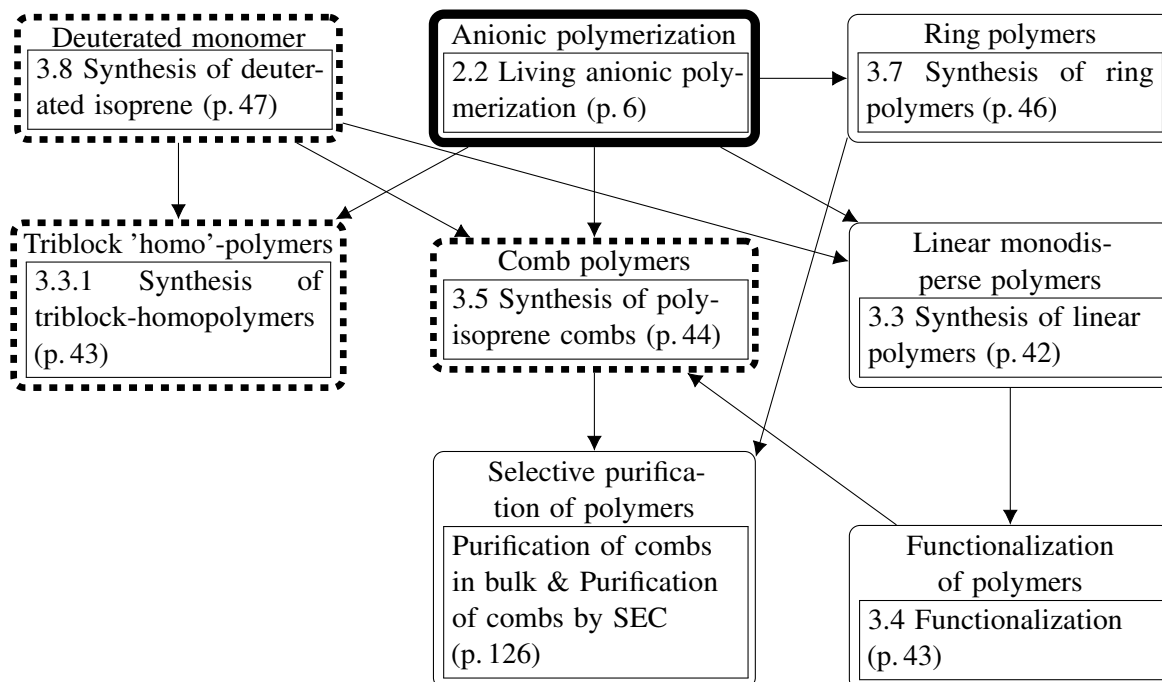

Figure 3.1. Summary of the different synthesis methods that have been applied in the current work and how they are interlinked. Moreover, the references to the respective sections are included. *Anionic polymerization* is highlighted as the theoretical background, the sections with the dashed lines are highlighted to emphasize the deuteron labeled model systems.

3.2 Anionic synthesis - equipment and preparations

This section visualizes the relevant tools and preparation in anionic synthesis. Anionic synthesis is highly sensitive towards traces of moisture, oxygen and other impurities. To eliminate these side reactions and resulting termination, these traces have to be removed, which is elaborated within this section.

For a successful synthesis suitable flasks and a vacuum-line with inert-gas is required. While in principle any multi-necked flask can be used as long as it stays attached to the manifold, it has been proven convenient to have dis-attachable *Schlenk*-flasks. The flask displayed in Figure 3.2 allows for a closed (inert) environment.
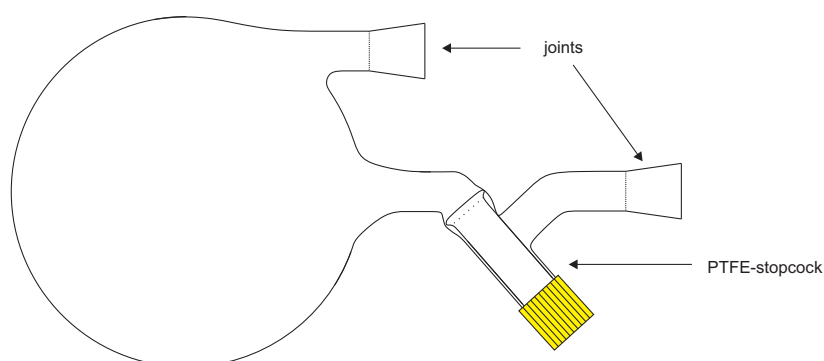

Figure 3.2. Scheme of a typical Schlenk-flask used in this thesis. The material is boro-silica glass with a PTFE stopcock. A typical volume is 250 mL, which allows for a good compromise between polymerization quantity and stirrability.

To successfully prepare an experiment in a Schlenk-flask, the impurities have to be removed using a Schlenk-line such as shown Figure 3.3. Grease free PTFE stopcocks have the advantage, that they do not loose grease over time and stay leak free for longer, which greatly increases the manageability. The flask is attached to the Schlenk-line with grease. Subsequently, the preparation of the flask includes commonly three cycles of heating under vacuum followed by flushing with inert gas. For pressures of approximately 10^{-3} mbar the mean free path length is above 1 cm, which implies that the likelihood that a gas molecule in a bottleneck hits the glass wall is higher than hitting a different glass molecule. In an environment like this, common fluid mechanics cannot predict the gas molecule flow, therefore, a manometer does not necessary display the pressure within the flask, meaning they are not necessary in an thermodynamic equilibrium (not considering temperature). The flushing with inert gas can drag impurities like moisture along, circumventing this problem.

Many polymers have a very strong adhesion to glass, which is only partially dissoluble using solvents. In order to maximize cleanness of the used flasks, oxidizing all organic remains in the flask at 500 °C is recommended. Moreover, preheating the glassware above 100 °C highly reduces the moisture intake.

Transferring chemicals from one container to the other was conducted with one of the following methods:

- The most secure method, in terms of purity, is distilling either the solvent, the monomer or the termination agent between two flask, preferably without using the Schlenk-line, but a short connector. The disadvantage is the amount which was distilled, has to be determined.

- Another very secure procedure is the connection between joints and then transferring the solvent through gravity or over-/under-pressure. This method allows for a good quantification of the amount
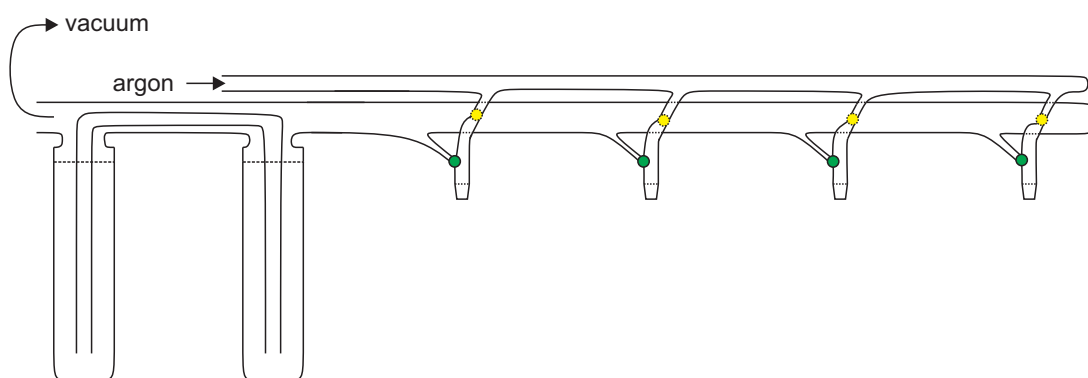
Figure 3.3. Scheme of a simplified Schlenk-line. The material is boro-silica glass with PTFE stopcocks and glass joints as connection points. The thicker line is the vacuum line, the thinner line is attached to the argon supply. The vacuum is powered by an oil pump with can technically generate pressures by specification down to 10^{-3} mbar. Between pump and Schlenk-line two cooling traps are installed, cooled with liquid nitrogen. A manometer displays the pressure. ☀ symbolized the argon-valves and ● symbolizes the vacuum valves.

used and is rather unsusceptible towards leakage. Yet, too many glass-joints typically reduce the feasibility of a synthesis due to leakage.

- The fastest method with the least required preparation is the transfer using plastic syringes. However, the system needs to be opened under inert-gas flux, and it is a possible to intake impurities on or in the syringe. To reduce these impurities the syringes are washed using cyclohexane or toluene to clean off the release agents from the production process.

- A glove box was not available in this work. In principle, a glove-box unifies the advantage of low impurity intake and usability.

3.3 Synthesis of linear polymers

The theoretical background of synthesis is elaborated in 2.2 *Living anionic polymerization*, p. 6. The initiation reaction and the termination reactions are analogous to the polymerization of styrene. The propagation reaction of isoprene is special and was elaborated in Figure 2.4. Hence, only short repetition is displayed in Figure 3.4. In this section the focus lies on the polymerization of isoprene from a practical point of view.
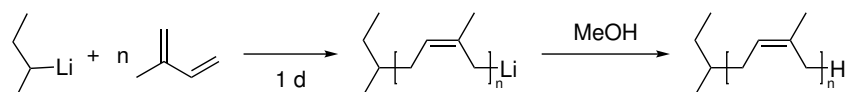

Figure 3.4. Polymerization reaction of isoprene in an unpolar solvent. Subsequently, the reaction is terminated by employing methanol.

Since the anionic polymerization of isoprene is well-established, it is referenced to the appendix for details in *Polymerization of isoprene to PI* (p. 124). Nevertheless, it is noteworthy that distilling degassed

methanol into the reaction mixture avoids side reactions during the termination process, resulting in no observable double molecular weight fraction.

3.3.1 Synthesis of triblock-homopolymers

The synthesis of the triblock-homopolymers is analogous to the synthesis of linear polymers. Once the monomer for the respective block has reacted, the monomer for the next block is added. Taking samples, to quantify the current molecular weight was skipped to avoid any moisture intake. The respective lengths of the blocks were calculated using the final molecular weight.

During the addition of the monomer for the new blocks, traces of impurities reach the reaction flask and consequently, a small fraction of the living anions are terminated. These fractions are detectable after the polymerization and can be used to verify the molecular weight of the respective blocks.

The term block-homopolymer is used, because deuterated and protonated molecules have comparable chemical and rheological properties.

3.4 Functionalization

In this section the functionalization of the employed polyisoprene is discussed from a practical point of view. The reader is referred to the appendix for more details.

Polyisoprene (PI) can be functionalized in different ways to introduce electrophilic groups. In this work, epoxidation was used, since this specific reaction was established in this working group and the substances possess low toxicity. Organic peroxy acid can oxidize alkenes in a Prileschajew-reaction forming epoxides that kinetically highly favors highly functionalized double bonds.[57]

Polyisoprene is highly unpolar, while peroxy acids are polar. Toluene is used to dissolve the PI, and the peroxy acids is formed *in situ* using formic acid and a hydrogen peroxide solution. Both are mixed forming a dispersion, the solubility of of the reactant is sufficient to have a significant conversion Figure 3.5.
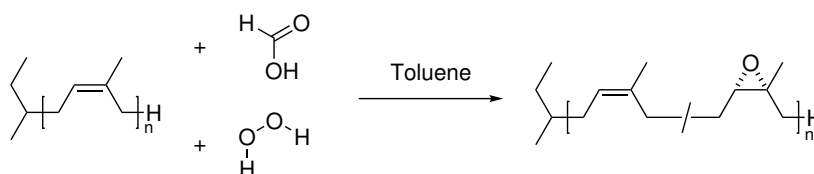

Figure 3.5. Epoxidation of polyisoprene: A peroxy acid is formed *in situ*, which oxidized the alkene group. Highly substituted double bonds are kinetically favored.

In order to yield to pure epoxidated polyisoprene (ePI), remaining water, acid and unreacted peroxy acid have to be removed. Literature suggests that three cycles of dissolving the ePI in THF and subsequent aceotropic destillation of the THF removes residual water.[58, 59] However, literature is not very specific on how to get THF into the flask with the ePI. This process presents is a non-trival issue since freezing ePI/PI below its T_g, results in a significant volume loss, while the adhesion to the glass is strong, resulting in flask breakage. Therefore, three different routes to add THF have been tested.

Firstly, the distillation of dried THF into the reaction flask with ePI using liquid nitrogen as cooling agent resulted in glass breakage in a few cases, and therefore, this approach was omitted as a safety hazard. Secondly, dried THF can be added to ePI using a syringe. This route has yielded good results. Yet, THF swells the polypropylene syringes resulting in a reduced feasibility. This matter can be circumvented by using glass syringes, however, this approach has not been done in this work.

Thirdly, the distillation of the dried THF using an ice bath as the cooling agent. This method results in a much smaller temperature gradient, assuming the THF in the reservoir is at ambient temperatures. Anyhow, the smaller gradient can be circumvented by longer distillation times. To reduce product loss, the obtained ePI was not washed with water, but the solvents were evaporated. Then the ePI was dried by dissolving it in THF and removing the THF in cycles under mild conditions (by using ice to cool the ePI flask). The reactants (hydrogen peroxide, formic acid and peroxo-formic acid) have a rather small vapor pressure with hydrogen peroxide having the highest, therefore, this route can remove of all relevant impurities. Since the approach has resulted in the highest purity of the products, this route has been chosen as the most suitable one (*e.g.,* in *Synthesis of partially a deuterated PI comb*, p. 50).

3.5 Synthesis of polyisoprene combs

In this section the synthesis of polyisoprene combs is discussed from a practical point of view. The reader is referred to the appendix for details. For a reaction scheme, refer to Figure 3.6.
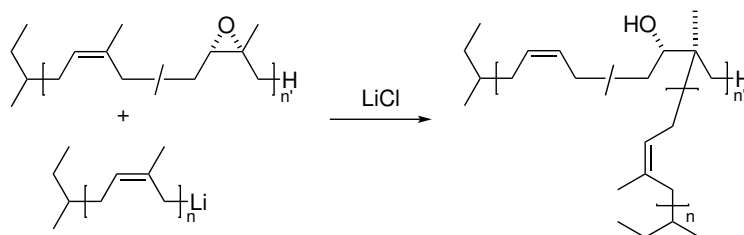

Figure 3.6. Grafting onto approach to a PI comb, by using epoxided PI as a backbone and living PI anions as later side chains. Since the epoxidized PI is dissolved in THF and the polymerization is performed in cyclohexane, the grafting onto is done in a THF/cyclohexane mixture in the presence of LiCl.

The synthesis of polyisoprene combs was performed by the *grafting onto* method. The ePI is prepared as explained in 3.4 *Functionalization*, p. 43, dried and subsequently dissolved in dry THF. Moreover, living PI carb-anions are synthesized in cyclohexane as side chains. To the ePI an aprotic Lewis acid (e.g, Lithium salts[58]) is added. To avoid any moisture intake due to the hygroscopic LiCl, a dry LiCl solution in THF was prepared in Schlenk-flask and added to the ePI. The living anions were added to the functionalized backbone stepwise, under Schlenk conditions and using glass joints.

A distinct yellow color indicates living PI anions in THF, which fades upon reaction with impurities and the epoxides in the backbone. While the former is very fast (basically diffusion controlled), the latter is slow (in the range of minutes/hours). Therefore, a stable color after adding a few percent of the anions is a indication that the backbone was sufficiently dry. Afterwards, the living anions are added stepwise. After reacting overnight, a sample is taken and characterized *via* SEC-MALLS. The addition of living anions is

repeated until the desired molecular weight and therefore the number of desired side chains is reached. Since side reactions cannot fully be avoided, the polymer combs is received as a mixture of terminated side chains and comb, which is purified in a further step.

3.6 Purification of polymer combs

In the method for the synthesis of polymer combs, side reactions terminate some of the living anions, resulting in a mixture of polymer comb and linear polymers. The polarity and solubility of the comb polymer typically does not deviate significantly from the linear homopolymer. Nevertheless, the solubility of polymers is a function of their molecular weight, therefore, a separation can be achieved by fractionated precipitation in *e.g*, a THF/methanol mixture.

Two methods have been established to purify homopolymers of different molecular weight: fractionated precipitation and purification by liquid chromatography, more precisely size exclusion chromatography. The advantage of the fractionated precipitation is that it can be used on a multigram scale and without additional equipment. However, a disadvantage is that a purification to greater 95 % is hardly showing any results.

The advantage of the SEC method is that the purity of the purified polymer is greater 99 %. The required SEC setup with a (preparative or semi-preparative) column, autosampler and fraction collector is required for significant quantities and poses an instrumental limitation. Moreover, the quantity is limited to about 2 mg/h, which is about 200 mg to 300 mg in a week.

The following subsection discuss the individual purification methods in greater detail.

3.6.1 Fractionated precipitation of polymer combs

The first step of a fractionated precipitation entails the dissolution of the polymer mixture (comb & linear) in a good solvent, *e.g.,* toluene for PI and PS. Subsequently, a non-solvent is added. Thereby, at the point where the solvents mix, polymer precipitates, which is redissolved fast (in less than 1 min) under stirring. During the process of adding the non-solvent to the polymer solution, the mixture continuously becomes opaque and milky. At the point at which polymer precipitates, without redissolution, the mixture is heated until all precipitate is redissolved again. Then the mixture is cooled down to ambient temperatures and after several hours, a high viscous phase is formed at the bottom of the solution. This polymer rich phase is separated. The top phase has an increased fraction of the small molecular weight polymers, and the bottom phase has an increased fraction of the high molecular weight species.

During the separation process high molecular weight species tends to stimulate the precipitation of smaller species. This phenomenon limits the success of the purification method. Therefore, in this process the amount of precipitated polymer is reduced to the minimum by working in dilute solutions $\leq$ 1 wt% and preferably by depleting the polymer mixture of the high molecular weight component, rather than precipitating all high molecular weight components and depleting the small molecular weight species in the precipitate.

3.6.2 Purification of polymer combs using size exclusion chromatography

The purification of polymer combs using SEC is facile, but requires high instrumental resources and is highly time consuming.

The column[1] of the SEC limits the maximum injectable mass. For the employed column in the current study, injections greater than 2 mg to 3 mg lead to strongly distorted peaks, due to overloading of the column. For instrumental details, refer to *Appendix*, p. 114.

A fraction collector and an autosampler allows for the automatization of the process, but the differential refective index (DRI) detector has to be kept as the last component, since it is very fragile. Therefore, either the process has to be done, without a DRI detector, or the DRI need to be installed after the fraction collector. In our case the latter was chosen, resulting in a setup with the following components: Autosampler, column, fraction collector, and DRI detector. In this approach, the DRI can only detect significant signals, when the fraction collector is not collecting. The amount of sample collected is about 1 mg per run.

THF is used as the solvent and it contains 250 ppm of the stabilizer 2,6-di-*tert*-butyl-4-methylphenol (BHT). A typical volume of fractionated the comb solution is about 4 mL with a semi-preparative column in a slightly overloaded state. Assuming 2 mg comb polymer per run result in about equal amounts of stabilizer and polymer are present in the fractionated solution. To extract the stabilizer the solution mixture after the chromatography, the solution is reduced under reduced pressure and subsequently, the polymer is washed with distilled methanol overnight three times.

3.7 Synthesis of ring polymers

PS ring polymers have been synthesized and characterized. The purity of the rings was estimated up to 95 % for the sample PS-ring10k. For the detailed procedure, the reader is referred to the appendix: *PS ring grafting* (p. 127) and *PS ring purification* (p. 127).

Table 3.1. List of synthesized PS-rings.

sample name	M_n[kg/mol]	$Đ$	ring content in the raw product wt%
PS-R11k	10.8	1.06	62
PS-R54k	54.4	1.08	42
PS-R138k	138	1.11	29
PS-R166k	165	1.07	28

The yield of the ring grafting is in the range of 15 % to 40 %, the 40 % for the small molecular weights, *e.g.,* PS-ring10k and 15 % for PS-rings above 100 kg/mol. The yield of the purification is depending on the resulting purity, but typically in the range of 70 %. Consequently, 20 g of employed styrene result in up approx. 5 g of purified ring. Several PS-rings have been synthesized in a cooperation with Prof. Dr. J. P. Lutz, Dr. M. Heck and Mr. M. Schäfer, which are listed in Table 3.1.

---

[1]Here a styrene-divinylbenzene column with a length of 300 mm, a diameter of 20 mm and a separation range of 10^2 g/mol to 10^6 g/mol was used.

3.8 Synthesis of deuterated isoprene

Fully deuterated isoprene was synthesized within the current thesis. The synthesis was adapted from Craig *et al.* [60] and performed in the JCNS (Jülich Center for Neutron Scattering) facilities under the supervision of Dr. A. Raba and Dr. J. Allgaier from the group of Prof. S. Förster.

Deuterated monomers are required to yield deuterated polymers. In principle, two routes are feasible to receive deuteron enriched monomers. The first possibility entails the synthesis of the molecule from scratch using deuterated chemicals only. Enrichment of the normal – protonated monomers with deuterium using exchange reactions presents the second option to obtain deuterated monomers. In this work a high degree of proton/deuterium purity is required, since both ^{2}H and ^{1}H-NMR spectroscopy have been done and on a block-co-polymer system that is both partially proton labeled and partially deuteron labeled. By building the monomers from scratch, the final degree of isotope purity is mostly determined by the purity of the starting materials. All relevant chemicals can be purchased with a isotope purity of well above 99 %. This way provides the maximum amount of deuteron purity. Therefore, the first option was selected.

From hereon, the synthesis of deuterated PI is described, for further details the reader is referred to the appendix *Deuterated 2-methyl-3-butin-2-ol*, *Deuterated 2-methyl-3-buten-2-ol* and *Deuterated isoprene* pp. 128 f. The method from literature [60] was adjusted to reduce the hazard of the synthesis. Instead of pure potassium to generate KOD together with D_2O, potassium *tert*-butoxide was used. In the first step, potassium *tert*-butoxide was hydrolized in D_2O. Subsequently, the *tert*-butoxide was removed under reduced pressure as presented in Figure 3.7. Since the potassium *tert*-butoxide does not have labile protons and is removed, non-labeled chemicals can be used.
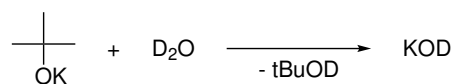

Figure 3.7. Synthesis of deuterated potassium deuterooxide (KOD). Starting from potassium *tert*-butoxide and D_2O, a potassium deuterooxide solution in D_2O and *tert*-butanole is obtained. To receive pure KOD, both the alcohol and the water have to be removed under heat and reduced pressure. The water content of the product is mainly influenced by the drying temperature, which overlaps with the melting point of the D_2O/KOD mixture (140 °C, for a water content of approx. 10 %).

Afterwards, the moisture content was reduced under heat and reduced pressure. Then diethylene glycol dimethyl ether (diglyme) was added as a polar solvent with a high boiling point. By melting KOD at elevated temperatures, a two phase systems (KOD and diglyme) is received, which is cooled to ≤5 °C under strong stirring into a slurry. This way, a basic mixture is obtained that is able to dissolve a significant amount of acetylene.

In the next step, acetylene is generated using calcium carbide and heavy water. For better heat distribution the CaC_2 is dispersed in diglyme and a flux of argon is applied. The acetylene is passed into the slurry and dissolved as presented in Figure 3.8.

To this slurry labeled acetone is slowly added over 1 h. The deprotonated acetylene can attack the carbonyl, forming the C5 structure which is the base body of isoprene. After adding D_2O to the dispersion two phases are formed: the alkaline aqueous phase at the bottom and the upper organic phase. After separation the organic phase is neutralized and distilled. To neutralize, dry ice is employed as a buffer (CO_2/$KHCO_3$) as presented in Figure 3.9.
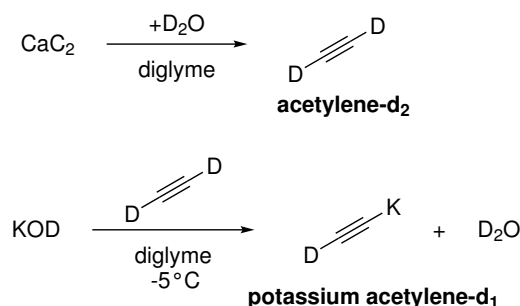
47

Figure 3.8. Synthesis of deuterated potassium acetylene.
A slurry of KOD in diethylene glycol dimethyl ether (diglyme) is prepared, by melting the KOD and cooling the two phased system under strong stirring. Calcium carbide is dispersed as a slurry in diglyme in a seperate container. A weak argon-flux is employed from the CaC_2 flask to the KOD flask to avoid moisture intake. Heavy water is added slowly to the CaC_2 and the resulting acetylene, which is diluted by the argon-flux and dried by $CaCl_2$, is passed into the KOD slurry. Potassioum acetylene is received as a slurry.
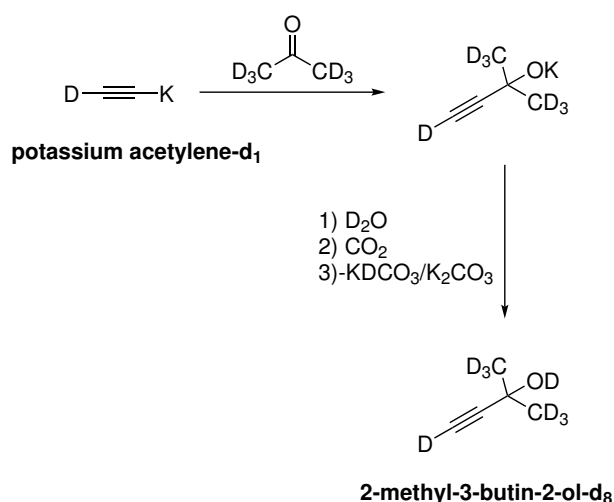

Figure 3.9. Synthesis of deuterated dimethyl butinol. The potassium acetylene is used as received and deuterated acetone is subsequently added under cooling. Afterwards, heavy water is added and the mixture is neutralized using carbon dioxide. After filtration, an azeotrope mixture of water and the butinol is received. The product and water form an aceotrope and their difference in the boiling point is less than 5 °C. Therefore a separation *via* distillation is difficult. Water can be either removed by using hygroscopic salts or ignored until the pyrolysis step, were an equimolar amount of water is produced anyway, which can be well separated from the isoprene. The dimethyl butinol is the C5 base body of the final product, isoprene.

After receiving the acetone free methyl-butinol, the mixture is deuterated[2] using D_2 and a Lindlar catalyst [Pd/Pb] as presented in Figure 3.11. As an example the ^2H spectrum of is presented in Figure 3.10. The methy-butenol is filtered, evaporated and pyrolized on a Al_2O_3 surface, refer to Figure 3.12. As a result deuterated isoprene is obtained and deuterated water as a side product. The mixture is collected and distilled at low temperatures (-70 °C) to yield pure deuterated isoprene, which is storable with a stabilizer (BHT).

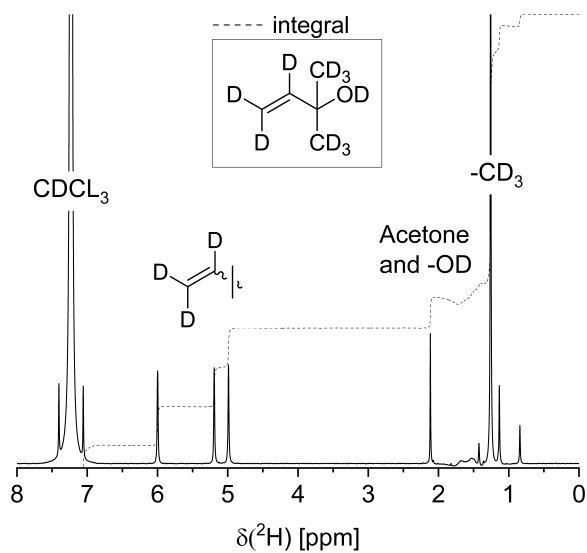[2]Like a normal 'hydration', but with D_2 instead of H_2.

Figure 3.10. ^{2}H-NMR spectrum of 2-methyl-3-buten-2-ol-d8.

2-methyl-3-butin-2-ol-d$_8$ **2-methyl-3-buten-2-ol-d$_{10}$**
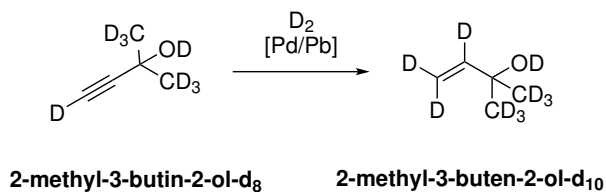
Figure 3.11. Synthesis of deuterated dimethyl butenol. The dimethyl butinol is deuterated/'hydrated' using D$_2$ and a Lindlar catalyst under pressure ($\leq$2 bar). The adduct is purified by filtering.

2-methyl-3-buten-2-ol-d$_{10}$ **isoprene-d$_8$**
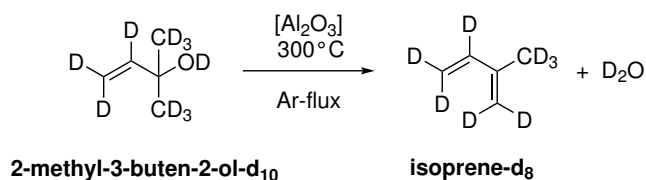
Figure 3.12. Synthesis of deuterated isoprene. A flow reactor in an oven is prepared with a flux of argon and a Al$_2$O$_3$ surface at 300 °C. The residence time of a molecule in this setup is approximately 10 s

.

3.9 Synthesis of partially a deuterated PI comb

A partially deuterated PI comb and a fully protonated comb with comparable attributes were synthezied, as in *Synthesis of polyisoprene combs*, p. 44. In the current section the molecular characterization is presented. All molecular weight values are calibrated against a protonated PI.

The analyzed data of the combs are presented in Table 3.2, the elugram is displayed in Figure 3.14 and a scheme is presented in Figure 3.15. The ^{1}H- and ^{2}H-NMR spectrum of the deuterated and epoxidized backbone is presented in Figure 3.13.
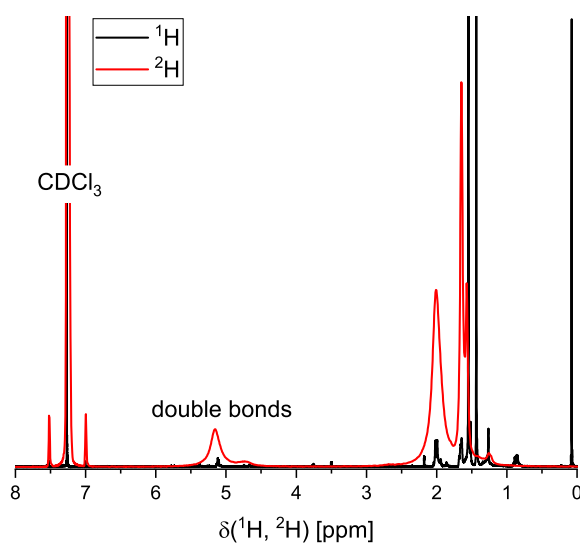

Figure 3.13. ^{2}H-NMR spectrum of deuterated epoxidized PI. In addition to that the ^{1}H-NMR spectrum of the $\lessapprox 1\,\%$ residual protons is added, since even though they are rare, the sensitivity for protons is superior and the selectivity is superior by about one order of magnitude. The chemical formula is presented in Figure 3.5, p. 43.

Table 3.2. Table with the molecular information of the labeled PI comb and a similar protonated comb. The molecular weight of the combs were obtained by SEC-MALLS and the molecular weight of the backbone and the side chains (sc) were obtained with conventional SEC.

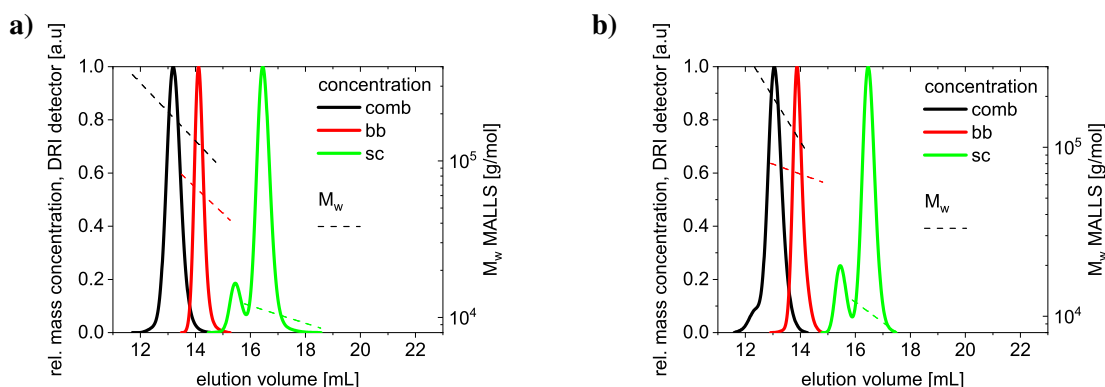| name	molecular weight M_n [kg/mol]			
	comb	backbone	side chain	number of sc
PI-D72k-9-H14k	190	72.6	13.8	8.5
PI-H68k-9-H14k	189	68.0	13.8	8.5

Figure 3.14. SEC Elugrams of the labeled PI comb **b)** and a similar protonated comb **a)**. Increasing molecular weights elute earlier, however, the topology differs between the samples a conventional calibration and is therefore not suitable for comb polymer systems. Consequently, SEC-MALLS was employed. The respective linear extrapolated molecular weights of the MALLS detector are presented by the dotted lines. Since these are extrapolations of the respective measurements, the molecular weighs are only valid for the respective trance and do not form a calibration curve. *Comb* refers to the final comb, *bb* to the backbone and *sc* to the side chains.

Figure 3.15. a) Scheme of the fully protonated PI comb PI-H68k-9-H14k and the partially deuterated. **b)** Scheme of the partially deuterated PI comb PI-D72k-9-H14k. The full lines represent PI side chains that are protonated and the dotted line represent the backbone that is deuterated. Both combs model systems are employed in 6.2 *DQ-NMR on model comb systems* (p. 86).

3.10 Synthesis of pom-pom topologies

Herein, a simple and scalable approach to relatively well-defined pom-pom like structures is introduced. Pom-pom polymer melts can be well modeled with the pom-pom-model [61] and are therefore a desired system in rheology. First mechanical characterizations were done on the synthezied system (refer to the appendix 11.1.2 *Rheology on a pom-pom topology*, p. 116), which can be expanded and investigated in a more in-depth way in the future. While the current chapter previous dealt with PI, herein the polymer is polystyrene (PS).

A triblock-co-polymer of PI20k-PS360k-PI20k, which was synthesized by sequential anionic polymer-ization[3], is dissolved in toluene and epoxidized with an excess of H_2O_2 and HCOOH. Hereby, a full conversion of the double bonds is targeted, refer to Figure 3.16.

The ePI-PS-ePI, dissolved in toluene, was washed with water to remove the remaining acid and hydrogen peroxide. However this approach was challenging, since the ePI-PS-ePI emulsifies the dispersion. To remove formic acid and hydrogen peroxide, the polymer was dissolved in dry THF, then THF is removed under reduced pressure and the polymer is again dissolved in THF. This cycle is repeated about 7 times.

---

[3]The author thanks Valerian Hirschberg for providing the sample PI20k-PS360k-PI20k.

After the third time, the polymer, which was milky after the epoxidiation, became clear. Subsequently, the ePI-PS-ePI is dissolved in THF and excess LiCl (dry and dissolved in dry THF) is added as preparation for the grafting onto reaction.

In a separate flask living PS anions in cyclohexane are prepared as side arms. In a grafting onto reaction the living PS is grafted onto the epoxidized backbone as displayed in Figure 3.17. PS anions have a yellow color, the loss of that color is an indication for the progress of the grafting reaction.

The adduct is a mixture of pom-poms and terminated side arm, which are separated by fractionated precipitation, which is working very favorably, since the contrast in molecular weight is high, and the solubility of the ePI part in MeOH is significantly worse than PS. The polymer is characterized by SEC-MALLS and SEC, the former for absolute molecular weights, and the latter with a big pored column to verify the dispersity. The parameters of the resulting pom-pom are listed in Table 3.3 and the molecular weight distribution is presented in Figure 3.18.
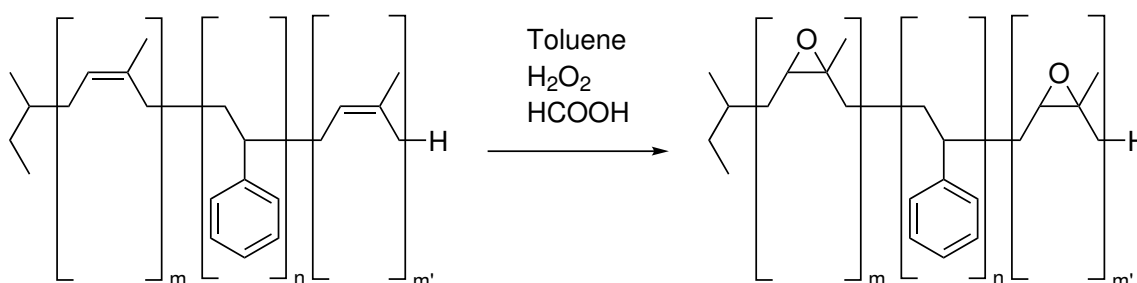

Figure 3.16. The epoxidation of a PI-PS-PI triblock-co-polymer to receive ePI-PS-ePI. The resulting polymer has a significant conversion of the double bonds. In the case of PI20k-PS360k-PI20k, $m = m' = 300$ and $n = 3430$.
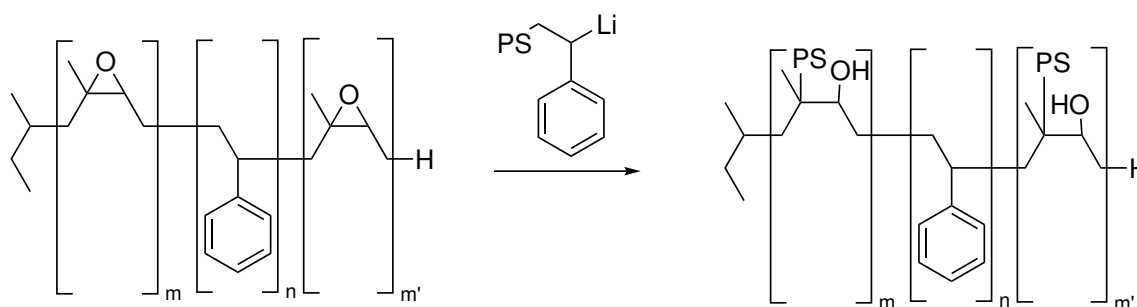
Figure 3.17. Grafting onto a ePI-PS-ePI with PS anions. ePI-PS-ePI is dissolved in THF at 0 °C. To this solution freshly prepared living PS anions with a molecular weight of $M_n = 135$ kg/mol in cyclohexane, are added.

Table 3.3. Parameter list of the PS pom-pom

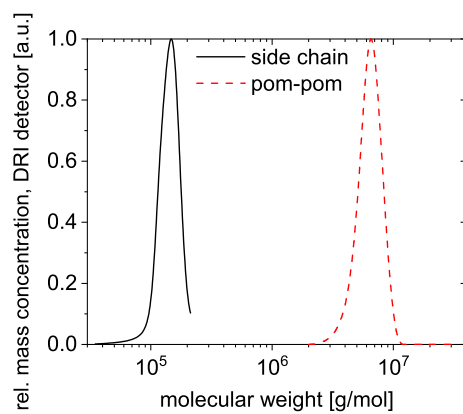| sample name	$M_{n,bb}$ [kg/mol]	$M_{n,sc}$ [kg/mol]	$M_{n,pom-pom}$ [kg/mol]	total number of side chains
PS pom-pom	360	135	6100	$2 \cdot 21 = 42$

Figure 3.18. Molecular weight distribution of the PS pom-pom obtained by SEC. The side chain is received with a conventional calibration and the pom-pom is characterized with a DRI/MALLS combination. The molecular parameters are listed in Table 3.3.

4 Fourier transform rheology of homopolymer model system

The current chapter deals with Fourier transform-rheology (FT-rheology) of different kinds of homopolymer melts. This project partially complies with a publication, that is in preparation, especially the introduction and section 4.2.5 *Model of volume-fraction weighted superposition*, p. 67.[62] As introduced in chapter 2.3.3 *Introduction into Fourier-transform rheology* a non-linear stress response to the oscillatory shear, contains higher harmonics (referred to the exaltation frequency). The theoretical background is elaborated as well as a parameter that characterizes the non-linearity, the intrinsic non-linearity parameter $^3Q_0$, which is defined in Equation 4.1 and Equation 4.2.

$$^3Q(\omega, \gamma_0) \equiv \frac{I_{3/1}}{\gamma_0^2} \tag{4.1}$$

$$^3Q_0(\omega) \equiv \lim_{\gamma_0 \to 0} \frac{I_{3/1}}{\gamma_0^2} \tag{4.2}$$

with the maximum shear amplitude γ_0 and the normalized intensity of the 3$^{\text{rd}}$ harmonic $I_{3/1}$. This relation was already emphasized in Equation 2.38.

In this chapter, the process to obtain the intrinsic non-linearity is demonstrated on the raw data. Afterwards, literature of the intrinsic non-linearity ($^3Q_0$) of homopolymer melts is reviewed. Finally, $^3Q_0(\omega)$ of polymer model systems are presented, including the prediction from semi-empirical models.

During the oscillatory shear on a strain-controlled rheometer, a sinusoidal strain is applied and the torque response is obtained (typical sampling rates are 512 per cycle), as shown in Figure 4.1 **a)**. By visual analysis of this raw data, no deviation from the linear torque signal is observable. Another possibility to display the rheological non-linearity are the Lissajous plots, which is a correlation plot that is not time dependent. The corresponding Lissajous-figures are displayed in Figure 4.1 **b)**. Since the measurement is periodic, any deviation from the linear relationship can be expressed by the higher harmonic components. Therefore, Fourier transformation (FT), which is an analytical transformation, can be employed to quantify the non-linearity as shown in Figure 4.2. To improve the information quality, one can truncate the first few halve circles which results in an enhanced the signal-to-noise ratio.

From the higher harmonics $I_{3/1}$ is normally chosen as the most sensitive parameter to represent the non-linearity. In a strain sweep experiment, $I_{3/1}(\gamma_0)$ is expected to have a quadratic scaling with the amplitude γ_0 for homopolymer melts. This leads to the parameter ^3Q that is defined as $^3Q \equiv I_{3/1}/\gamma_0^2$, which is expected to have a constant value for varying γ_0, as found in Figure 4.3. In this way, the required
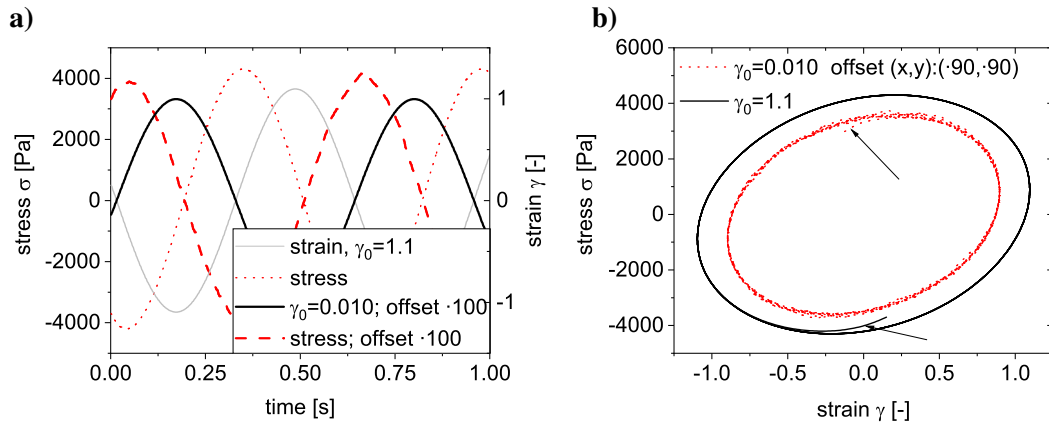
Figure 4.1. Experimental signals from two rheological measurements using a bidisperse PI (PI-12%120k,88%31k) at $T = 30\,°C$, $\omega = 10\,rad/s$ and $\gamma_0 = 0.010$ to 1.1. **a)** The stress $\sigma(t)$ and strain $\gamma(t)$ is presented as a function of time. The experiment with the lower amplitude $\gamma_0 = 0.010$ is offset by a factor of 100. Both strain signals are computer generated sines. The stress signals are recorded by the transducer which are both mostly sines. For the experiment with the lower amplitude $\gamma_0 = 0.010$ the response is noisy. **b)** The stress $\sigma(\gamma)$ is presented as a function of strain (γ). The experiment with the lower amplitude is offset by a factor of 90. A (perfect) ellipsoid corresponds to the application of two (perfect) sine signals with certain phase shift. A deviation of this ellipsoidal behavior is given at the beginning of the datapoints, which are indicated by arrows. Moreover, noise is visually observable for the case with less amplitude $\gamma_0 = 0.010$. At the higher amplitude $\gamma_0 = 1.1$, a barely noticeable deviation from an ellipsoid resulting from the non-linear contributions is observable.

parameters to analyze the linear and non-linear proprieties of homopolymer melts are reduced to four numbers: $|G^*|$, δ, $^3Q_0$ and δ_Q, the latter is the phase of $^3Q_0$.

Several systems have been characterized using FT-rheology in literatures, including linear monodisperse homopolymers[1, 63], polymer solutions[64–66], polymer combs[63, 67], polymer [68], composite systems[69–72], networks [73], solid (glassy) polymers [74–76] and industrial polymers [77–79].
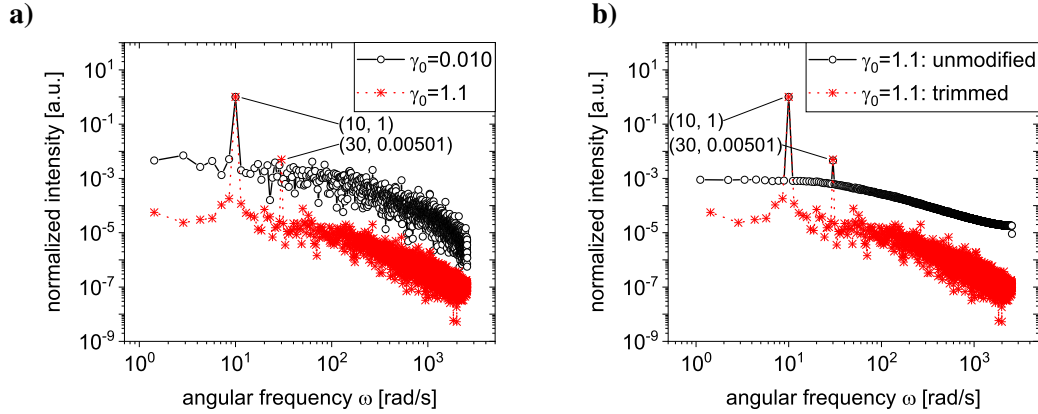
Figure 4.2. Normalized FT spectra of two rheological experiment using a bisdisperse PI (PI-12%120k,88%31k) at $T = 30\,°C$, $\omega = 10\,\text{rad/s}$ and $\gamma_0 = 0.010$ to 1.1.
a) Fourier transformed stress $\mathcal{F}(\sigma(t))$ of both experiments, the amplitude is normalized to a maximum of 1. A noise level of 1 % to 0.01 % is observable, the noise level of this normalized plot is reciprocal proportional to the amplitude of the stress. In the high amplitude experiment a 3rd overtone is found.
b) Fourier-transformed for the experiment of $\gamma_0 = 1.1$, the non-trimmed data set is the data as received and the modified data set is trimmed. The trimming truncates the first period (refer to Figure 4.1), removing possible effects change of the dynamic equilibrium. Moreover, the signal is truncated further with the first and last zero crossing being the limits. Since the experiment is done using only full cycles, the modified signal has an even number of halve cycles.
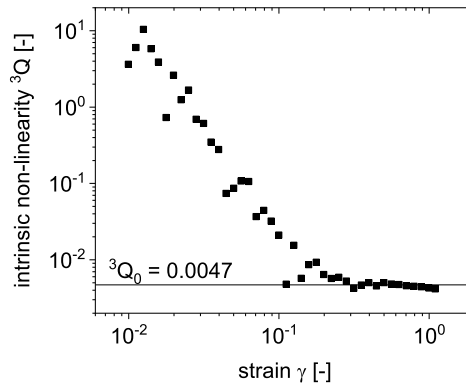

Figure 4.3. Strain sweep of a bisdisperse PI (PI-12%120k,88%31k) at $T = 30\,°C$ and $\omega = 10\,\text{rad/s}$ from $\gamma_0 = 0.010$ to 1.1. The non-linearity parameter $^3Q \equiv I_{3/1}/\gamma_0^2$ as a function of γ_0 shows three distinct trends. 1st The noise in I_3 is higher as the theoretical I_3. Therefore, I_3 takes a value that is a sum of noise and systematical errors that are mostly constant. Since I_1 is proportional to the strain, a $I_{3/1} \propto \gamma_0^{-1}$ relationship is found.[34] 2nd In MAOS I_3 is above its noise level, resulting in a constant ^3Q, as predicted. The extrapolation to $\lim_{\gamma_0 \to 0}$, which equals the mean value for constant data is the intrinsic non-linearity parameter $^3Q_0$, which has no dependency on the strain anymore. 3rd Towards high amplitudes, in the LAOS regime, ^3Q is not constant anymore, since $I_{3/1}$ has an upper limit of $I_{3/1} = 1/3$ for large strain amplitudes. However, this region is rarely reached in this type of experiments.

4.1 FT-Rheology of homopolymer melts

Cziep *et al.*[1] found a semi-empirical model, that predicts the intrinsic non-linearity $^3Q_0(De)$ as a function of the Deborah number De for all entangled monodisperse linear homopolymer melts. This model is derived by pom-pom model[80] and the molecular stress function (MSF) model[81–83]. The intrinsic non-linearity depends on the number of entanglements Z and the Deborah number De as presented in Equation 4.3.

$$^3Q_0(\omega)(De, Z) = 0.32 \cdot Z^{-0.5} \frac{De^2}{1 + 33.8 \cdot Z^{-1} \cdot De^{2+k}} \tag{4.3}$$

model for linear homopolymers [1]

The free parameter k was found to be in the range of $k = 0.35$ for all characterized monodisperse systems.[1] Equation 4.3 can be rewritten with the definition of the Deborah number $De \equiv \omega\tau_d$ to Equation 4.4. Even though, this transformation results in one more parameter compared to Equation 4.3, the used parameters ω is a directly obtainable experimental parameter and τ_d is a defined time (with a reference temperature).

$$^3Q_0(\omega, \tau_d, Z) = 0.32 \cdot Z^{-0.5} \frac{(\omega\tau_d)^2}{1 + 33.8 \cdot Z^{-1} \cdot (\omega\tau_d)^{2+k}} \tag{4.4}$$

The number of entanglements Z is a measure of the length of the polymer, normalized to the entanglement molecular weight. The relaxation time τ_d of the monodisperse polymer chains mainly depends on two variables: The glass transition temperature, which is dependent on the used monomers, and the length of the polymer chains, which can be expressed in Z. At the glass transition temperature (obtained from dynamic scanning calorimetry), the segmental relaxation time τ_s equals to approximately $100\,\mathrm{s}$[84]. As described in 2.4 *Dynamics and rheological properties of polymer melts*, p. 25, the terminal relaxation time τ_d can be calculated from the segmental relaxation time τ_s as a function of number of entanglements of the polymer chains Z, refer to Equation 2.48. Consequently, the resulting frequency dependent non-linear mechanical properties ($^3Q_0(\omega)$) in melt is a function of the a length parameter Z and the glass transition temperature T_g, as a monomeric property, only.

From Equation 4.4, it can be deduced that $^3Q_0(\omega)$ has an maximum. However, that maximum is at values $\omega\tau_d \neq 1$ (therefore, $De \neq 1$) but a value close to 1, which is derived in Equation 4.5, where two extrema are found.

$$\frac{\partial}{\partial \omega}\,^3Q_0(\omega) = \frac{0.64\omega\tau_d^2}{\sqrt{Z}\cdot\left(1+\frac{33.8(\omega\tau_d)^{2.35}}{Z}\right)} - \frac{25.4\omega^2\tau_d^3(\omega\tau_d)^{1.35}}{Z^{3/2}\cdot\left(1+\frac{33.8(\omega\tau_d)^{2.35}}{Z}\right)^2} \tag{4.5}$$

$$\text{extreme values: } \frac{\partial}{\partial\omega}\,^3Q_0(\omega) \overset{!}{=} 0$$

$$\omega_1 = 0$$

$$\omega_2 = \frac{0.469Z^{1/2.35}}{\tau_d}$$

$$^3Q_0(\omega_1) = 0$$

$$^3Q_0(\omega_2) = 0.0105Z^{0.351}$$

$$(\omega_{\text{trivial}},\,^3Q_0(\omega)_{\text{trivial}}) = (0,0) \tag{4.6}$$

$$(\omega_{\text{max}},\,^3Q_0(\omega)_{\text{max}}) = ([0.469Z^{1/2.35}/\tau_d],\,[0.0105Z^{0.351}]) \tag{4.7}$$

By excluding the limit case ($^3Q_0(\omega) \lim_{\omega\to 0} = 0$), a maximum is found at ($[0.469Z^{1/2.35}/\tau]$, $[0.0105Z^{0.351}]$). Which implies, that both ω_{max} and $^3Q_{0,max}$ are dependent on Z, but the value of $\omega_{max}\cdot\tau_d$ is close to 1.

4.2 FT-Rheology on bidisperse polymer melts

The model for the intrinsic non-linearity of monodisperse systems (refer to Equation 4.2) was extended to describe bidisperse polymer melts. Herein several leading questions and challenges occurred, which are explained in detail later. This includes the modeling of the linear rheology using models known in literature to obtain the relaxation times, such as the terminal relaxation time of the long and short components ($\tau_{d,L}$ and $\tau_{d,S}$). Additionally, the intrinsic non-linearity is modeled *via* different approaches. In Figure 4.4 the linear viscoelasticity (LVE) and FT-rheology of a bidisperse melt is compared to the two respective monodisperse components.

By mixing two monodisperse homopolymers, the polymer chain dynamics are a superposition of both components. In Figure 4.4 the mechanical response of monodisperse and bidisperse polymer melts is compared. In comparison the two linear monodisperse polymers, the relaxation time of the long component L relaxes faster because of the mixing with smaller components and the smaller component S relaxes slower, due to the mixing it with longer components. The trends in FT-rheology follow the same trend as in LVE. Moreover the absolute intensities of $^3Q_0(\omega)$ change due to mixing. The modeling of the $^3Q_0(\omega)$ trends are described in the following sections.
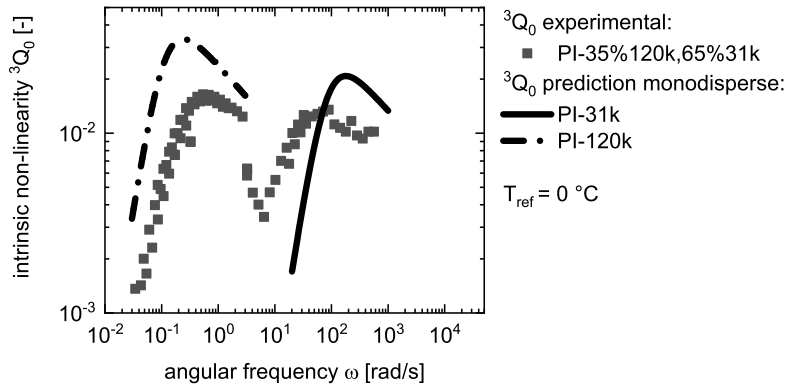
a)
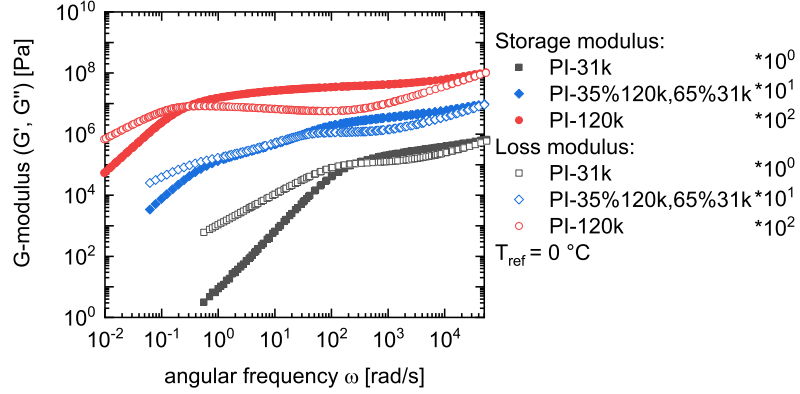
b)

Figure 4.4. FT-rheology and LVE of a bidisperse melt and its respective monodisperse components. **a)** Two linear monodisperse PI with a molecular weight of $M_n = 31\,\text{kg/mol}$ (PI-31k) and $M_n = 120\,\text{kg/mol}$ (PI-120k), and a mix of 35 % of PI-31k and 65 % of PI-120k (PI-35%120k,65%31k) are characterized in a linear mastercurve. **b)** The non-linear mastercurve $^3Q_0(\omega)$ for the bidisperse system was constructed and compared to the predictions (refer to Equation 4.4) of the mastercurve using the relaxation times from LVE experiments.

4.2.1 Models of dilution theory in the linear regime

Different models are known in literature to describe the relaxation of a bidisperse or multidisperse[1].[78, 85–88] The models for G are typically expressed in the time domain.[2] For example, a monodisperse polymer melt can be described by a single exponential decay[26], refer to Equation 4.8.

$$G(t)/G_N^0 = \exp(-2t/\tau_d) = [\exp(-t/\tau_d)]^2 \tag{4.8}$$

where G_N^0 is the plateau modulus.

---

[1]Multidisperse, in contrast to polydisperse, has a discrete and small number of components. (*e.g.,* ≤ 10)

[2]In contrast to typical rheological measurements in this thesis, which are expressed in the frequency domain.

For bidisperse melts, the respective volume fractions for the long and short component (ϕ_L and ϕ_S) and their terminal relaxation times ($\tau_{d,L}$ and $\tau_{d,S}$) are employed, which leads to Equation 4.9.

$$G(t)/G_N^0 = [\phi_L \cdot \exp(-t/\tau_{d,L}) + \phi_S \cdot \exp(-t/\tau_{d,S})]^2 \tag{4.9}$$

A more in-depth model, which considers additional effects, such as primitive path fluctuations, is the Rolie-Double-Poly (RDP) model.[85, 87, 89] To stay consistent with literature, the nomenclature is kept close to the work from Boudara *et. al.*[85] Herein two types of polymer chains L (long) and S (short) are considered. Depending on the respective volume fractions (ϕ_L and ϕ_S), the chances that an entanglement point a combination of the polymer $L - L$, $S - S$, $L - S$ or $S - L$ are given by $\phi_L\phi_L$, $\phi_S\phi_S$, $\phi_L\phi_S$ or $\phi_S\phi_L = \phi_L\phi_S$, respectively. Moreover, the entanglement survivability rate for pure L and S entanglements ($p_L(t)$ and $p_S(t)$) can be derived from reptation theory. The rate of $p_{L,S}(t)$ is described by the product of the respective components is described in Equation 4.10.

$$p_{L,S}(t) = p_L(t) \cdot p_S(t) \tag{4.10}$$

In the stress relaxation experiment, $G(t)$ is proportional to the remaining entanglements. The contributions from the $L - S$ entanglements normalized to G_N^0 are as presented in Equation 4.11.

$$G_{L,S}/G_N^0 = \phi_L\phi_S p_{L,S}(t) \tag{4.11}$$

For systems exceeding two components Equation 4.11 can be extended to n components as in Equation 4.12, however, herein the focus is set to bidisperse systems.

$$G(t) = \sum_{i=1}^{n} \sum_{j=1}^{n} G_{i,j}(t) \tag{4.12}$$

For further details the reader is referred to literature [85].

To use the RDP model the free software RepTate©[90] was employed. It allows for the import of experimental data with a graphical user interface in a very user friendly manner. Furthermore, different models can be selected to model the raw data, including the RDP, which in principle requires the molecular information of the employed polymer and τ_e (refer to Equation 2.50, p. 28), which are used to calculate the relaxation times τ_S and τ_L and the partial contributions to the moduli. The relaxation times can be exported directly from the software, however, the fit can only be saved as a (vector)graphic.[3]

4.2.2 Fitting with the RDP-model

Bidisperse PIs (for the sample list, refer to Table 4.1) were first characterized by linear oscillatory shear rheology and fitted using the RPD model. In Figure 4.5 the fits are compared to the experimental results. Models that predict the mechanical response from the chain relaxation, are limited to the regime where

---

[3]The received fitted data have to be extracted from the vector graphic.

the chain relaxation is dominant. This observation is found between the smallest terminal relaxation time $\tau_{d,S}$ and the entanglement relaxation time τ_e. For $G'(\omega)$ the it fits up to $\omega = 1/\tau_e$, while for $G''(\omega)$ the predictions works up to $\omega = 1/\tau_{d,S}$.
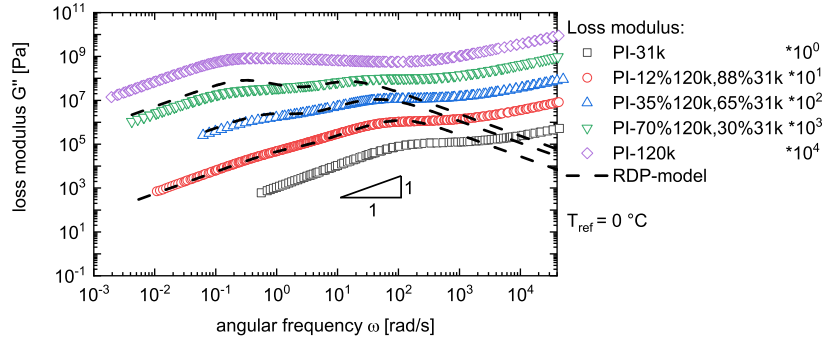
a)
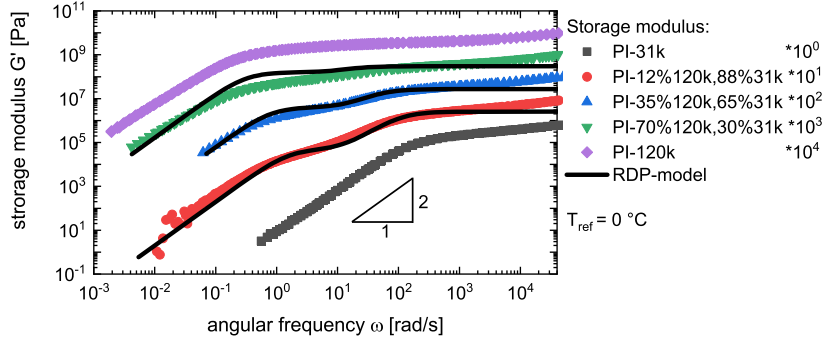
b)

Figure 4.5. RDP-predictions for bidisperse melts with the respective experimental results. **a)** The storage modulus of 3 bidisperse PI melts and their monodisperse components is presented. The data of the bidisperse systems are compared to the fits of the RPD model. In contrast to the monodisperse systems, the bidisperse systems show two relaxation modes observable by the two concave curvature. Towards high angular frequencies the storage modulus the model approaches G_N^0, which agrees with the experiment. **b)** The loss modulus of the same PI melts is presented and compared to the fits with RDP model. In addition to that, the storage modulus of the monosiperse components are presented for comparison. The two relaxation models are observable by the two concave curvatures, too. At high angular frequencies, the loss modulus approaches to zero in the RDP model, which does not agree with the experimental results.

In Figure 4.5 the trends of $G'(\omega)$ and $G''(\omega)$ are compared between the bidisperse melts and the monodisperse systems. For monodisperse systems two regimes are defined, the flow regime towards smaller frequencies and the rubber regime towards higher frequencies with the transition at $\omega = 1/\tau_d$. In the flow regime $G'(\omega)$ and $G''(\omega)$ show power law behavior with exponents of 2 and 1, respectively, which agrees with the Maxwell model. In the rubber plateau, $G'(\omega)$ is constant with increasing ω. At the point, where $\delta = \arctan(G'/G'')$ has a minimum, the plateau value for G_N^0 is received.

Bidisperse systems have three regimes which are dependent on the relaxation times of the two components (L and S, where $\tau_{d,L} > \tau_{d,S}$): The flow regime ($\omega < 1/\tau_{d,L}$), the regime of dynamic dilution ($1/\tau_{d,L} < \omega < 1/\tau_{d,S}$) and the rubber plateau ($1/\tau_{d,S} < \omega$). While the relaxation times τ_L and τ_S are

influenced by the respective volume ratios ϕ_L and ϕ_S ($\phi_S = 1 - \phi_L$), the scaling laws in the flow regime and the rubber plateau are the same as for the monodisperse samples. The regime of dynamic dilution is strongly dependent on the volume fractions.

A model that extends the tube model to bidisperse melts is displayed in Figure 4.6. It uses a tube model with a 'fat' and 'thin' tube[91]. Herein any polymer chain is confined in a double tube, a fat and a thin one. The thin tube is constrained by all types of polymer chains (L and S) with their respective relaxation times. The fat tube is constrained by the long chains (L) only. In the relaxation process, three cases can be analyzed, which correspond with the three regimes of bidisperse polymer melts, and is explained within this section: $\omega < 1/\tau_{d,L}$, $1/\tau_{d,L} < \omega < 1/\tau_{d,S}$ and $1/\tau_{d,S} < \omega$.

In the first regime, the tested chain is free of constrains and the material can flow.

In the second regime, all constrains of S are released, which allows for the test chain to diffuse in the fat tube. This comes with several implications and consequences, which are partially redundancies: Less entanglements per volume results in a fatter tube. A fatter tube results in less entanglements. Less entanglements result in a reduced modulus. Less entanglements results in a higher effective entanglement molecular weight. With a reduced effective M_e, the component L can drop under the semi-empirical condition of $M_n \gtrsim 3 \cdot M_e$, which is the precondition to have a rubber plateau. Consequently, if the condition is met, G' is dominant, otherwise, G'' is dominant.

In the third case, the test chain is constrained by entanglements of all types of chains that results in a rubber like state (rubber plateau).
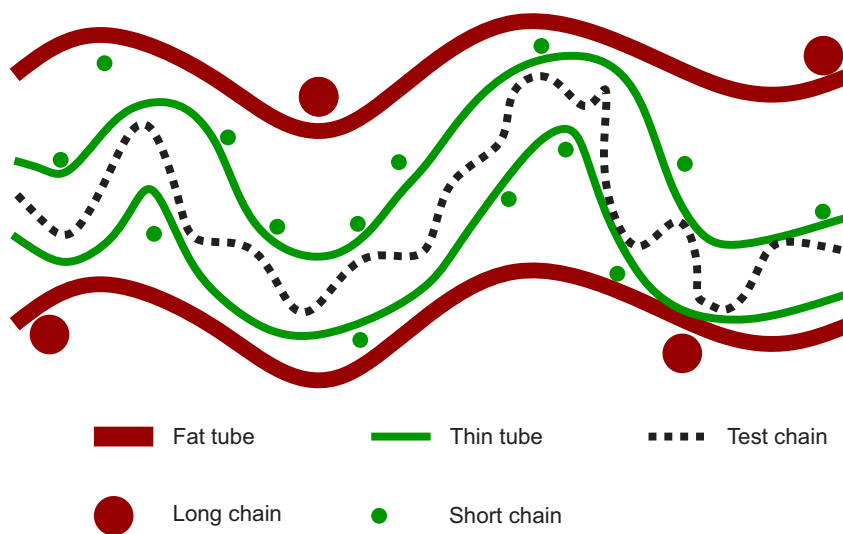

| ━━━ Fat tube | ━━━ Thin tube | ▪▪▪▪ Test chain |

| ● Long chain | ● Short chain |

Figure 4.6. Expansion of the tube model for bidisperse systems, with two virtual tubes. The 'thin' tube is constrained by all types of polymer chains. The 'fat' tube is constrained only by the longer chains. Within short time scales $< \tau_{d,S}$, the test chain is restricted by all types of chains and therefore in the thin tube. For medium time scales, which are faster than the relaxation of the small chain but slower than the relaxation of the long chain, the test chain is restricted by the long chains only and therefore in the fat tube. At time scales longer than the relaxation of the long chain $> \tau_{d,L}$, the test chain is not restricted.

Table 4.1. Relaxation times of the PI model systems for $T_{\text{ref}} = 0\,°\text{C}$. For the experimental data, refer to Figure 4.4. The values are obtained by fitting with the RDP model for the bidisperse systems or by the crossover angular frequency for the linear polymers.

sample name	ϕ_L	$M_{\text{n},L}$ [kg/mol]	$\tau_{d,L}$[s]	ϕ_S	$M_{\text{n},S}$ [kg/mol]	$\tau_{d,S}$[s]
PI-12%120k,88%31k	0.12	120	1.3	0.88	31	0.016
PI-35%120k,65%31k	0.35	120	2.5	0.65	31	0.03
PI-70%120k,30%31k	0.70	120	6.5	0.30	31	0.07
PI-120k $(= L)$	1.00	120	8.0	-	-	-
PI-31k $(= S)$	-	-	-	1.00	31	0.006

The resulting relaxation times are presented in Table 4.1. As expected, with increased dilution fraction of smaller chains the relaxation time of the long component increases, and with increasing addition of long components, the relaxation time of the smaller chains is increasing.

4.2.3 Comparison of the modes between FT-rheology and linear rheology

The relaxation times from the RDP model was compared to the relaxation times, obtained from FT-rheology in Figure 4.7. As elaborated in 4.1 *FT-Rheology of homopolymer melts* and Equation 4.7, the non-linear relaxation time is not equivalent to the maximum(s) of the non-linear mastercurve. In Figure 4.7 the relaxation times from the LVE and the trend of the maxima in the non-linear mastercurve correlate, resulting in a promising approach to model $^3Q_0$. To do so, a superposition is assumed and modeled by two terms similar to Equation 4.3, with the resctive relaxation times, obtained by LVE. Thereby, it is convenient to avoid the usage of the Deborah number De, since both relaxation times are of importance. The first basic approach is in 4.2.4 *Model of reduced entanglements*, to describe the decrease in non-linearity at the maxima of $^3Q_0$ as a reduction of entanglements due to dilution, since $^3Q_0(\omega)_{\mathrm{max}}$ is a function of Z.

In the second approach in 4.2.5 *Model of volume-fraction weighted superposition*, the absolute value of $^3Q_0$ is weighted by the volume ratio ϕ of the respective component.
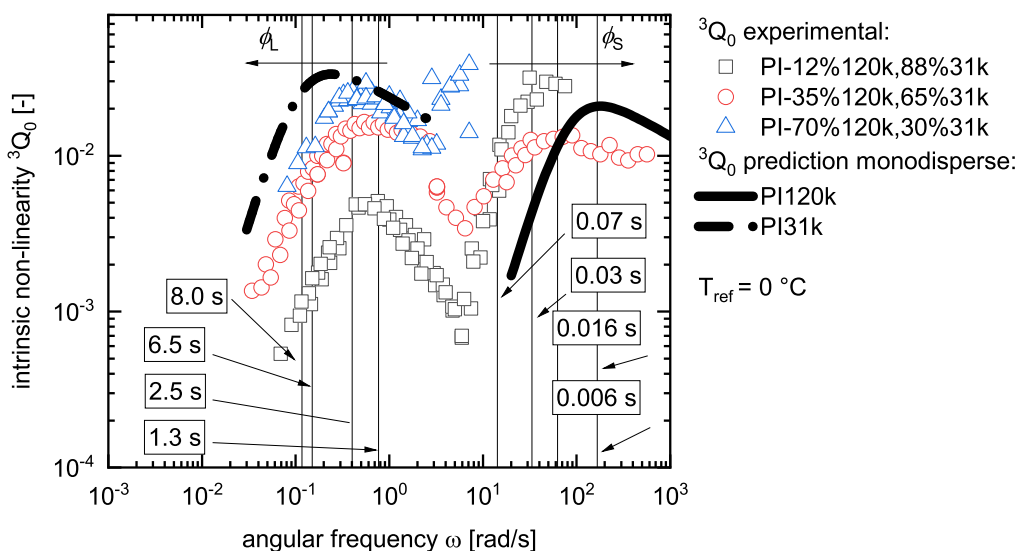

Figure 4.7. The non-linear mastercurve of the three bidisperse melts. Additionally, the predictions for the linear polymer melts are presented. Moreover the relaxation time, obtained by the RDP are added as listed in Table 4.1 are presented as vertical lines.

4.2.4 Model of reduced entanglements

In literature [1] $^3Q_0(\omega)$ is modeled as a function of Z. Herein, the approach is evaluated to model the non-linear behavior of bidispese systems with a reduction of entanglement according to the dilution theory. The lower plateau modulus decreases with decreasing volume fraction of the longer component $G_N^0 \propto \phi_L^2$, which originates from the double repation mechanism. Since M_e is inversely proportional to G_N^0 ($G_N^0 \propto 1/M_e$) and the number of entanglement in a polymer chain is reciprocally proportional to M_e

$(Z \propto 1/M_{\mathrm{e}})$, the effective number of entanglements is reduced relatively to ϕ_L^2. Some theories consider a slightly higher exponent expressed as $Z_L = Z_{L,undiluted} \cdot \phi_L^{1+\alpha}$ with $\alpha = 4/3$ [26, 92–94].

Derived from the picture assignment as the fat and thin tubes, two tube relaxation processes are assumed, with the respective relaxation times τ_L and τ_S. Consequently, Equation 4.13 is formed.

$$
\begin{aligned}
{}^3Q_0(\omega, \tau_L, \tau_S, Z_L, Z_S, \phi_L, k_L, k_S) &= 0.32 \cdot (Z_L \phi_L^2)^{-0.5} \frac{(\omega \tau_L)^2}{1 + 33.8 \cdot (Z_L \phi_L^2)^{-1} \cdot (\omega \tau_L)^{2+k_L}} \\
&+ 0.32 \cdot Z_S^{-0.5} \frac{(\omega \tau_S)^2}{1 + 33.8 \cdot Z_S^{-1} \cdot (\omega \tau_S)^{2+k_S}}
\end{aligned}
\tag{4.13}
$$

Hereby, the parameter k is reintroduced, it defines the negative slope towards high angular frequencies. It is found to be $k = 0.35$ for monodisperse systems[1]. The trends for applying the model in Equation 4.13 and $k_L = 0.35$ for the bidisperse system is presented in Figure 4.8. The parameter k_S is set to $k_S = 0.35$, which corresponds to the monodisperse (in the rubber plateau) for all following predictions. This model shows good agreement with the absolute intensities of the of the peak maxima. But it shifts the relaxation times of the long component towards longer times, in comparison with the experimental data. Moreover, the minimum, which corresponds respective values in the time scales between τ_L and τ_S the model shows no agreement with the experimental data. The analysis of Equation 4.13, with the assumption of $Z_L > Z_S$, $k = 0.35$ and $\tau_L >> \tau_S$, leads to a maximum of ${}^3Q_0$ as presented in Equation 4.14 that scales to $\phi_L^{0.351 \cdot 2} \approx \phi_L^{0.7}$. For a different value of k (e.g., $k = 0.90$) the maximum shifts on the abscissa and ordinate as shown in Equation 4.15. The deduction is longer and unclear, therefore, for the full calculation, refer to the appendix and Equation 11.5, p. 119.

$$
(\omega_{max,L}, {}^3Q_{0,max,L})|_{k_L=0.35} = \left(0.469 \frac{(Z_L \phi_L^2)^{0.426}}{\tau_L}, 0.0105(Z_L \phi_L^2)^{0.351} \right)
\tag{4.14}
$$

$$
(\omega_{max,L}, {}^3Q_{0,max,L})|_{k_L=0.90} = \left(0.391 \frac{(Z_L \phi_L^2)^{0.345}}{\tau_L}, 0.152(Z_L \phi_L^2)^{0.379} \right)
\tag{4.15}
$$

From Equation 4.14, Equation 4.15 and Equation 11.5 can be derived that the dependency of the maxima in absolute values and ω of the slope parameter k is strong and obscure.[4]

In summary, in this section the intrinsic non-linearity was modeled with a semi-empirical model (refer to Equation 4.13), which was derived from literature (Equation 4.3 [1]). Hereby, it is assumed that the number of entanglements of the long component is reduced according to dilution theory by small chain components. The swelling of the tube diameter is resulting in less effective entanglements, due to the small components. The absolute values for the peak maximum in ${}^3Q_0(\omega)$ is in good agreement with the model. Moreover, this model shows a significant shift in terms of the relaxation time, which is off by almost an order of magnitude for the sample PI-12%120k,88%31k. In the regime between τ_L and τ_S the

---

[4] 'Obscure' or 'unclear' in the sense that the relation between $(\omega_{max,L}, {}^3Q_{0,max,L})$ with k is defined, but complicated and hard to approximate.
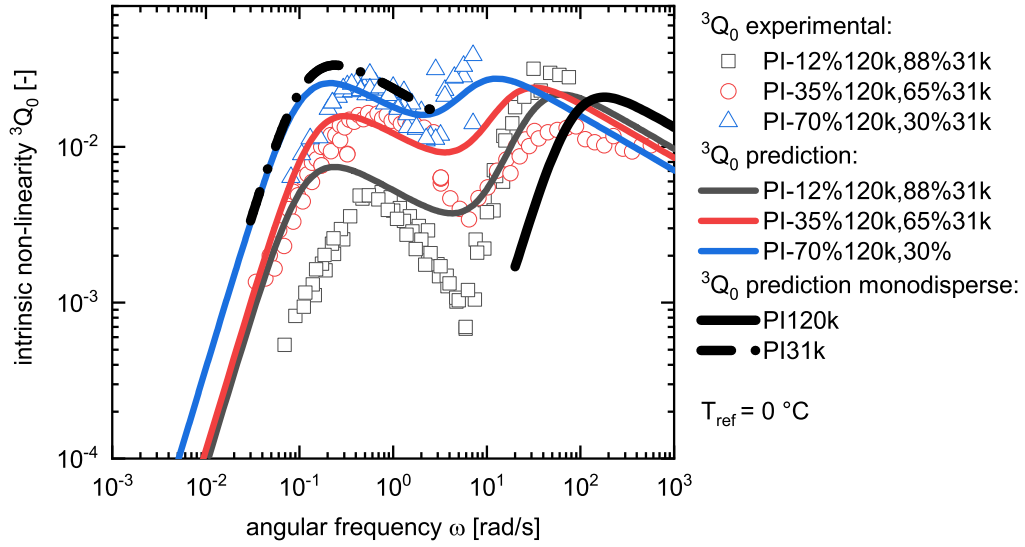
Figure 4.8. Modeling $^3Q_0$ by reducing the effective number of entanglements according to dilution theories $Z_{L,eff} = Z_L \cdot \phi_L^2$, while assuming the relaxation times obtained by linear rheology. While the absolute height of the peak maxima is in agreement with the experimental data, the shift in the absolute relaxation time of τ_L and the minimum between the two relaxation processes cannot be modeled sufficiently, so far.

model is in bad agreement with experimental data. The fitting parameter k, which influences this area has a strong impact on the peak position of the long component.

4.2.5 Model of volume-fraction weighted superposition

In Figure 4.7 the intrinsic non-linearity was modeled by a linear superposition with the respective relaxation times from LVE, which are weighted by the respective volume ratios (ϕ_L and ϕ_S). Additionally, the model from linear monodisperse systems (refer to Equation 4.3) was modified into Equation 4.16, hereby the parameter k is kept as a fitting parameter. In Figure 4.9 the quality of the model (Equation 4.16) is visualized.

$$
\begin{aligned}
{}^3Q_0(\omega, \tau_L, \tau_S, Z_L, Z_S, \phi_L, k) =& \phi_L \cdot 0.32 \cdot Z_L^{-0.5} \frac{(\omega \tau_L)^2}{1 + 33.8 \cdot Z_L^{-1} \cdot (\omega \tau_L)^{2+k_L}} \\
&+ \phi_S \cdot 0.32 \cdot Z_S^{-0.5} \frac{(\omega \tau_S)^2}{1 + 33.8 \cdot Z_S^{-1} \cdot (\omega \tau_S)^{2+k_S}} \\
\phi_L =& 1 - \phi_S
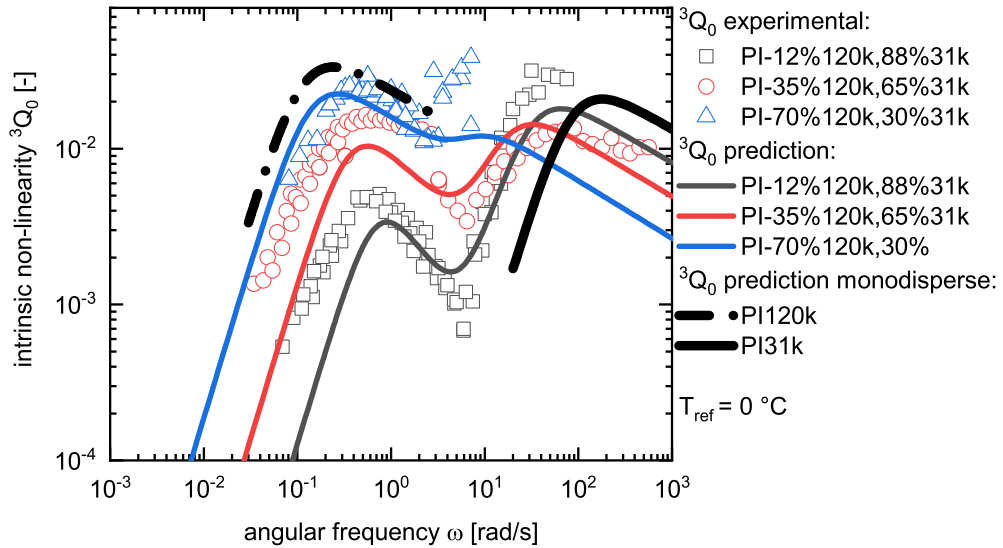\end{aligned}
\tag{4.16}
$$

Figure 4.9. Modeling ${}^3Q_0$ by a linear superposition, which is weighted by the respective volume ratios of the components. The slope parameter k is free. The general features of the experimental data is approximately modeled, such as the relaxation times, the absolute value and the region between τ_S and τ_L. Nevertheless, there are deviations.

This semi-empirical approach allows for a general description of the important trends of the experimental data, such as the peak position of the long and short component, the peak intensity of the long and short component, the slopes at small frequencies and the slopes between the relaxation time τ_L and τ_S (the modeling of the slope towards higher frequencies after τ_S not available due to insufficient data). As explained in the previous section k_S is set to $k_S = 0.35$, due to the lack of sufficient data. For the parameters in Equation 4.16, only ω and k_L are free, other parameters can be acquired or predicted using

different methods, such as ϕ_L, Z_L and Z_S from SEC while τ_L and τ_S are obtainable from linear rheology. This empirical finding is unexpected, because the intrinsic non-linearity is a normalized parameter as introduced in *Rheology* p. (17). $^3Q_0$ (only observing the part of the long chains) is normalized already to I_1 (see the double reptation *Fitting with the RDP-model* p. 60). Moreover, $I_1 \propto |G^*|$ and $|G^*| \propto \phi^2$. However, a proportionally of $^3Q_{0,max,L} \propto \phi_L$ can be observed, even though $^3Q_0$ is already normalized. Consequently, the dependency of non-linear intensities (*e.g.,* I_3) to ϕ_L have to be stronger compared than the contributions to LVE (e.g. that is essentially I_1), which means the non-linear contributions scale with ϕ_L^3.

Scaling laws of with power of about 3 are not uncommon in rheology, but typically are related to relaxation times such as $\eta \propto \tau_d \propto Z^3$. With the relationship of $G^* = i\omega\eta^*$, an additional time component is added to the mechanical property G^*, resulting in $\eta_0 \propto Z^3$. Assuming that the approach is correct, this model would imply that the non-linearity might be an interaction between the viscous and elastic part of the polymer melt. Collaboratively, the maximum intrinsic non-linearity is found at frequencies with a phase angle of $\delta = 45°$ for monodisperse systems, while in bidisperse systems that exhibit only one crossover point, it is found at the point where δ is close to $45°$.

4.3 FT-Rheology on comb polymers

In this section, comb polymer melts were characterized in oscillatory shear rheology in the LVE regime and in the MAOS, in the latter case by applying FT-rheology. Hereby highly defined topologies were employed. The combs were synthesized using living anionic polymerization and characterized as described in section 3.5 *Synthesis of polyisoprene combs* (p. 44), the herein this section characterized systems are presented in Table 4.2. The length of the backbone (bb) is monodisperse and well characterized, and the length of the side chains (sc) is monodisperse and well characterized. Moreover, the molecular weight distribution of the entire comb is characterized, which allows to calculate the average number of side chains per backbone.

Table 4.2. Table of the molecular information of the combs characterized with FT-rheology. The respective relaxation times are tabularized in Table 4.3, p. 75.

sample name	ϕ_{bb}	$M_{n,bb}$ [kg/mol]	ϕ_{sc}	n_{sc}	$M_{n,sc}$ [kg/mol]
PI-120k-6.5-31k	0.35	120	0.65	6.5	31.0
PI-70k-9-14k	0.38	70	0.62	9	13.8

In first approximation, the functionalization reaction and the grafting onto reaction are statistical processes, therefore, the side chains are expected to be distributed statistically on the backbones. Determining the

dispersity $Đ$ precisely is challenging[5], but $1.1 > Đ$ can be guaranteed.[6] Even though literature[95, 96] on the prediction of molecular weight distributions of comb-like systems is known, they are not applicable to our systems due to different synthesis approaches.

In this section, the experimental intrinsic non-linearity of comb polymer melts are modeled, by using information obtained by linear rheology and molecular information. An example for LVE and raw $^3Q_0(\omega)$ of a comb polymer melt is presented in Figure 4.10. In contrast to the monodisperse samples, the comb shows two rubber plateaus.[7] Moreover, the comb exhibits a greatly increased τ_d of the backbone, which is expected, since the total molecular weight increases. While the longest relaxation time of the entire comb from linear rheology is still accessible, so far the relaxation times from the side chains is complicated to extract.

In a first step, the relaxation time of the entire comb is extracted, by extrapolating the slopes of $G' \propto \omega^2$ and $G'' \propto \omega^1$ in the flow regime and using the crossover as relaxation time.[8]

In the last section is has been concluded that the peaks for both components (L and S) in the intrinsic non-linearity are related to the relaxation mechanism of the respective component of the bidisperse systems. A comb is different, in the sense, that it is a single molecule. A comb has has two different parts, the backone (bb) and the side chain (sc), which relax in a different way, for both parts normal reptation is restricted[26, 97, 98]. The comb is different from the corresponding bidispese blend, since the bb is chemically linked with the sc, other than physically transient entanglements. The sc relaxation mechanism is dominated by constrained release, double reptation and contour path fluctuations, since its reptation is restricted by the bb, which cannot be dragged into the tube of the sc. However, the relaxation of the bb is even more complicated. On the one hand the reptation is restricted in the same way as the sc. On the other hand, the bb relaxes much slower than the sc. Considering this fact, the bb can be seen as a chain an expanded tube with increased friction (which is introduced due to the sc).

---

[5]Measuring the $Đ$ of a comb is challenging, since a statistical distributed comb, has different topologies, which might elute at the same time. Therefore the assumption which the SEC-MALLS is typically applying, that the sample is monodisperse at a given elution volume, is not fulfilled anymore. Moreover, smoothing certain smoothing/fitting procedures are applied, which influence the molecular weight distribution.

[6]As an example the PI-H68k-9-H14k (p. 87, has a $M_{n,comb} = 189$ kg/mol), the bb is $M_{n,bb} = 66$ kg/mol, the sc is $M_{n,sc} = 13.8$ kg(/mol) and the number of side chains per backbone in average is 8.5. To calculate the resulting molecular weight the formula $M_{n,comb} = M_{n,bb} + n_{sc} \cdot M_{n,sc}$ is used. To calculate the dispersity from the standard deviation normal distributions in the molecular weights is assumed. With a standard deviation of $\sigma = (\sqrt{Đ - 1} \cdot M_n)$, while both components have a dispersity of approximately $Đ \approx 1.02$. Moreover, for the number of side arms a Poisson distribution of k elements is assumed, which is approximated with a normal distribution with $\mu = k = 8.5$ and $\sigma = \sqrt{k} = \sqrt{8.5}$. To calculate the deviations, we assume a random draw from the molecular weight distribution for the respective chain types and the observed length of the chain has a certain error (from monodisperse). Consequently the following relation applies $\mu = M_n$ the and the 'uncertainty' of this number is σ. With these, the Gaussian propagation of errors is applied to calculate the expected deviations. This results in following formula $\sigma_{M_{n,comb}} = \sqrt{(\sigma_{M_{n,bb}})^2 + (n_{sc} \cdot \sigma_{M_{n,sc}})^2 + (M_{n,sc} \cdot \sigma_{n_{sc}})^2}$ and a $M_{n,comb} = 189$ kg/mol) and $\sigma_{M_{n,comb}} = 44.5$ kg/mol, which results in $Đ = (\sigma_{M_{n,comb}}/M_{n,comb})^2 + 1 = 1.057$.

[7]Two rubber plateaus in a comb are observable, when both the side chains are well entangled and of the backbone is well entangled. The tube diameter of the backbone swell, compared to a linear polymer chain of equal length, since the side chains are swelling its surroundings.

[8]This method only works, if all polymeric components are in the terminal regime, a high dispersity leads to smaller scaling laws. For monodisperse systems this extrapolated crossover points is close the (not extrapolated) crossover in G' and G''.
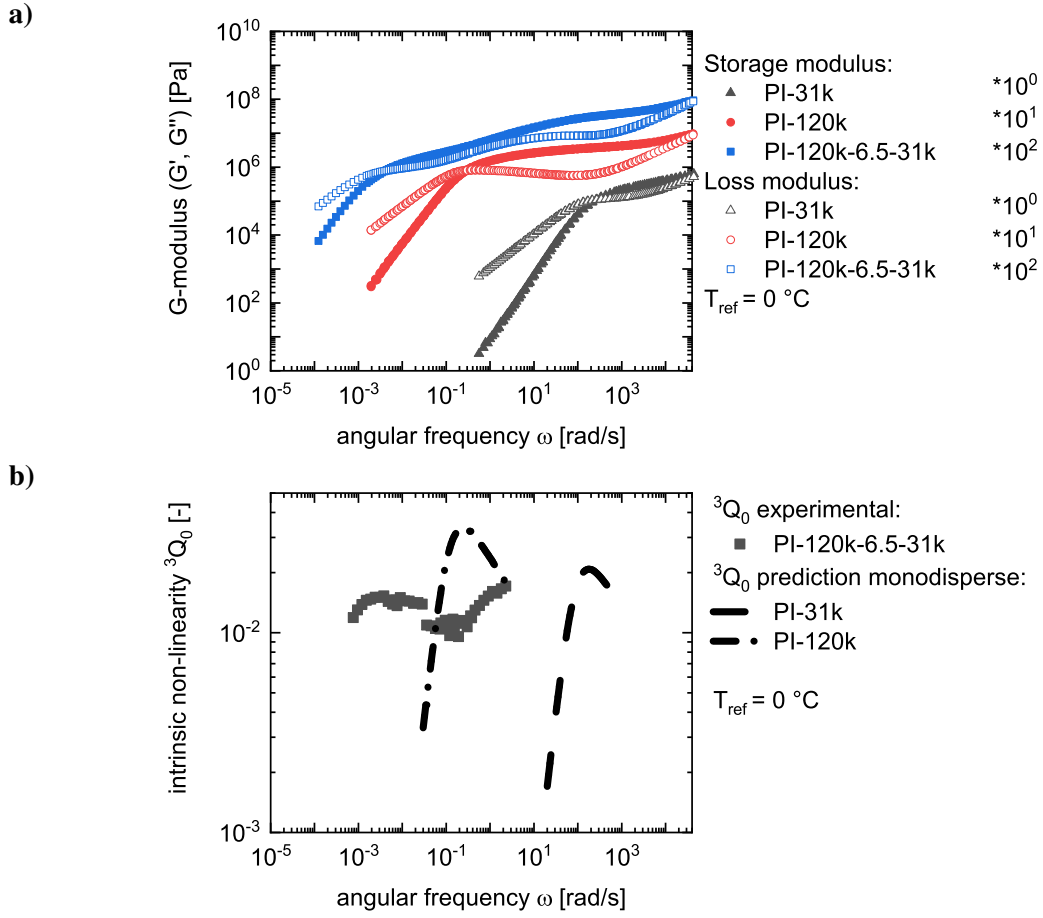
Figure 4.10. FT-rheology and LVE of a comb (PI-120k-6.5-31k) polymer melt and its monodisperse components. **a)** Two linear monodisperse PI, with a molecular weight of 31 kg/mol and 120 kg/mol, and a comb with bb of 35 % 31 kg/mol and 6.5 sc of 65 % 120 kg/mol each are characterized in a linear mastercurve. **b)** The non-linear mastercurve for the comb system was constructed and compared to the predictions (refer to Equation 4.4) of the mastercurve using the relaxation times from LVE. The $^3Q_0(\omega)$ trend is much flatter and the relaxation processes are shifted towards longer relaxation times.

To model the combs Equation 4.16 is used, but L and S are renamed to bb and sc, respectively to model the bb and sc in Equation 4.17.

$$^3Q_0(\omega, \tau_{bb}, \tau_{sc}, Z_{bb}, Z_{sc}, \phi_{bb}, k_{bb}, k_{sc}) = \phi_{bb} \cdot 0.32 \cdot Z_{bb}^{-0.5} \frac{(\omega\tau_{bb})^2}{1 + 33.8 \cdot Z_{bb}^{-1} \cdot (\omega\tau_{bb})^{2+k_{bb}}}$$

$$+ \phi_{sc} \cdot 0.32 \cdot Z_{sc}^{-0.5} \frac{(\omega\tau_{sc})^2}{1 + 33.8 \cdot Z_{sc}^{-1} \cdot (\omega\tau_{sc})^{2+k_{sc}}} \quad (4.17)$$

$$\phi_{bb} = 1 - \phi_{sc}$$

To understand the relaxation mechanism of polymer combs, the non-linear mastercurve of combs is modeled and compared to the model linear bidisperse melts. In Figure 4.11 the (renamed) model from Equation 4.17 from 4.2.5 *Model of volume-fraction weighted superposition* is applied to the intrinsic non-linearity. The parameters of the model are filled as follows:
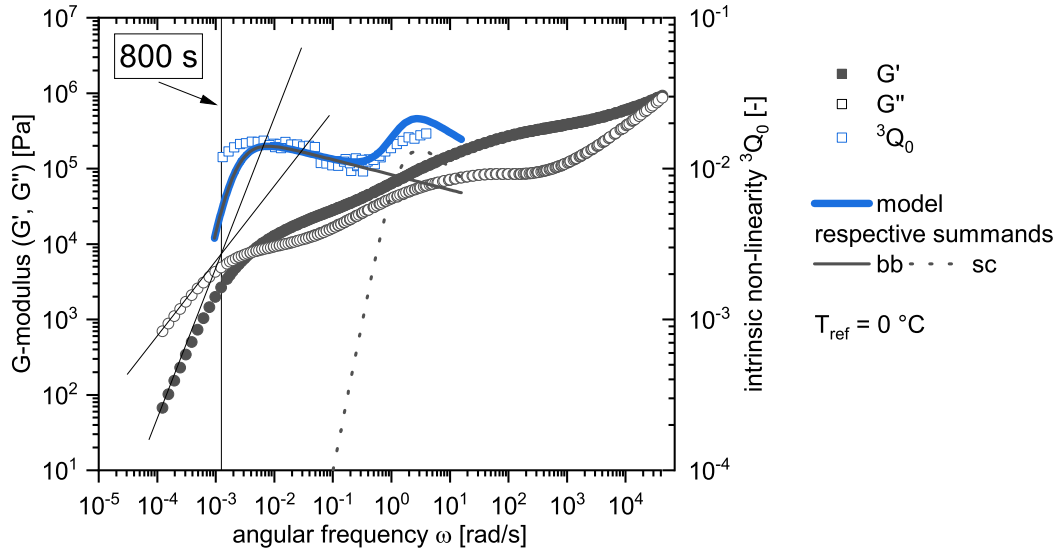
Figure 4.11. FT-rheology and LVE of a polymer comb melt. The comb (PI-120k-6.5-31k) with bb of 35 %
120 kg/mol and 6.5 sc of 65 % 31 kg/mol each. Presented are the LVE and $^3Q_0$. The $^3Q_0$ is modeled with
Equation 4.17, additionally, the respective summands are added.

ϕ_{bb} ratio of the bb to the comb ($M_{n,bb}/M_{n,comb}$, synthesis parameter)

ϕ_{sc} ratio of the sc to the comb ($n_{sc} \cdot M_{n,sc}/M_{n,comb} = (1 - \phi_{bb})$, synthesis parameter)

Z_{bb} number of the entanglements of the raw bb (synthesis parameter)

Z_{sc} number of the entanglements of the raw sc (synthesis parameter)

τ_{bb} extrapolating the crossover of $G' \propto \omega^2$ and $G' \propto \omega^1$

τ_{sc} free parameter

k_{bb} free parameter

k_{sc} $k_{sc} = 0.35$ (for the same reason k_S is set to $k_S = 0.35$ for the bidisperse case as explained in the
previous sections)

Hereby, only two parameters are free, from which τ_{sc} has a direct physical meaning (the relaxation time
of the sc), but is difficult to model in LVE. The slope parameter k_{bb} is found to be $k_{bb} = 0.1$, which is
different compared to the bidisperse systems in the previous section.
In literature[1] a peak broadening for increased and dispersity is reported. Moreover, combs which
are synthesized in the given fashion exhibit a dispersity which is strongly influenced by the number of
sc, where the sc are distributed statistically. For the comb polymers in this section, the dispersity is

approximately $Đ \leq 1.1$, which is a higher value compared to the 'monodisperse' samples with a dispersity of down to $Đ = 1.01$. Consequently, a broader peak is experted. Moreover, a broader peak influences the slopes on both sides of the peaks. This peak broadening is attributed to a k close to zero.
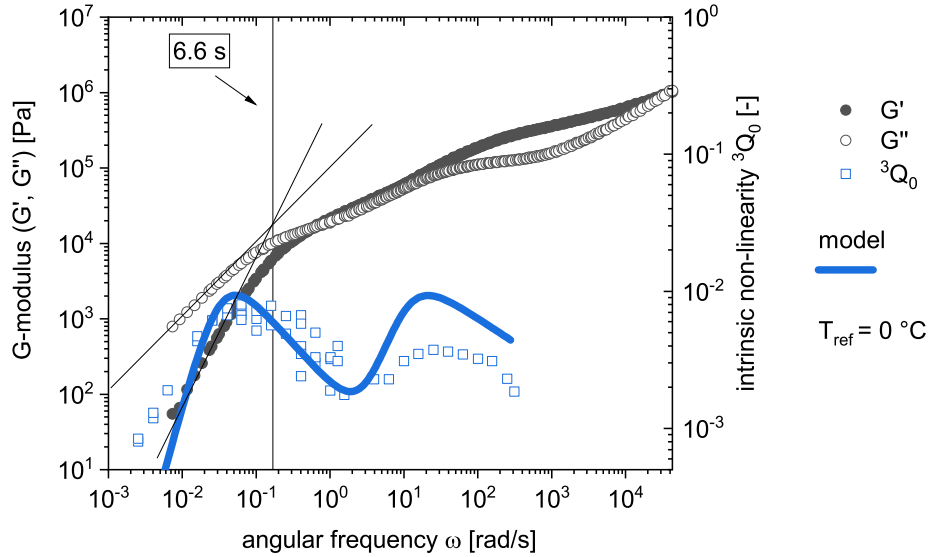

Figure 4.12. FT-rheology and LVE of a polymer comb melt. The model system is a comb PI-70k-9-14k with bb of 38 % 70 kg/mol and 9 sc of 62 % 13.8 kg/mol each. Presented are the LVE and $^3Q_0$. The latter is modeled with Equation 4.16.

Similar to the statistical distribution of the number of sc, the distance between two sc on a bb is also statistical. Therefore, a continuum of different distances between sc is expected, which leads to a multiple relaxation mechanisms. Consequently a flatter peak of $^3Q_0(\omega)$ is likely, resulting in a value for k of closer to zero.

In Figure 4.12, the intrinsic non-linearity of the comb PI-70k-9-14k is predicted by the model Equation 4.17. In the same way, the extrapolated relaxation time from the comb was used to obtain $\tau_{bb}, Z_{bb}, Z_{sc}, \phi_{bb}$, and ϕ_{sc}. The relaxation time of the sc remains a fitting parameter, and so does k, which has a value of $k = 0.6$.

Herein this section, Z_{sc} was takes as a molecular parameter. However, for future investigations, it can be considered that the number of entanglement, which this parameter is defined as, is practically increased, since the side chains are chemically connected to the backbone.

4.3.1 The slope parameter k

The parameter k shows a correlation with the volume ratio of the long component, as emphasized in Figure 4.13. Hereby, an empirical power law is found as in Equation 4.18.

$$k_L(\phi_L) = a \cdot \phi_L^b \tag{4.18}$$

where a is fixed at the limit for the monodisperse case $a = 0.35$ and $b = -0.54$. The pom-pom model predicts a slope of $k = 0$ and the molecular stress function (MSF) model predicts a slope of $k = 1$ for monodisperse systems, as reported in literature [1]. For small ϕ_L, the parameter k has a high probability above the theoretical predictions of the monodisperse case, which shows the necessity to further investigate polydisperse cases, especially with models that consider the interaction of different types of polymers.
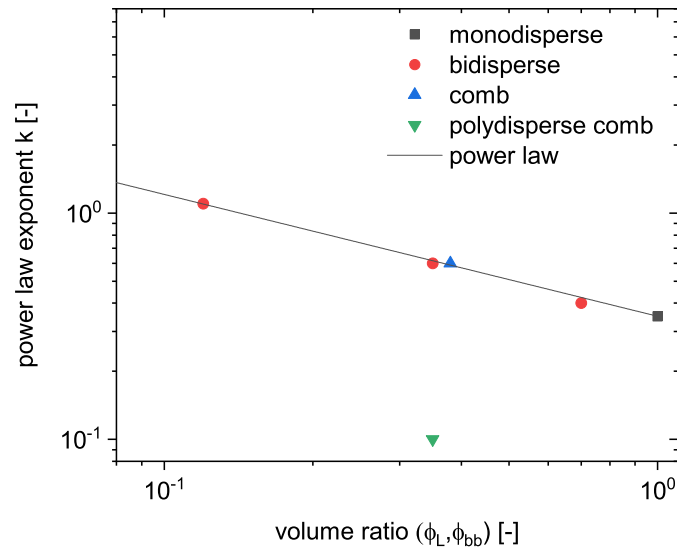

Figure 4.13. The power law exponent k as a function of the longer chains or the bb in polymer melts. The results of the bidisperse systems (refer to Equation 4.16 and Figure 4.9), the monodisperse case [1] and the combs systems (refer to Equation 4.17, Figure 4.11 and Figure 4.12) are included. The comb with the higher polydispersity shows a deviation from the trend. The power law slope k can be described with an empirical power law as a function of the volume ratio as follow: $k(\phi_L) = a \cdot \phi_L^b$, where a is fixed at the limit for the monodisperse case $a = 0.35$ and $b = -0.54$. In the case for the combs ϕ_L corresponds to ϕ_{bb}.

4.4 Summary of modeling the non-linear rheology of bidisperse and comb-like melts in the MAOS regime

Within this section the results from 4.2 *Fundamentals-rheology: Fourier-transformed time data* (p. 56), 4.2 *FT-Rheology on bidisperse polymer melts* (p. 58), and 4.3 *FT-Rheology on comb polymers* (p. 68) are summarized. The modeling from the intrinsic non-linearity from literature was adapted to fit different model system, such as comb polymer melts and bidisperse polymer melts. Hereby, the semi-empirical model (refer to Equation 4.3)[1] is extended by assuming a linear superposition of two relaxation modes. The resulting formula is Equation 4.19 (or with indexes corresponding to polymer combs Equation 4.17).

$$
{}^3Q_0(\omega, \tau_L, \tau_S, Z_L, Z_S, \phi_L, k_L, k_S) = \phi_L \cdot 0.32 \cdot Z_L^{-0.5} \frac{(\omega\tau_L)^2}{1 + 33.8 \cdot Z_L^{-1} \cdot (\omega\tau_L)^{2+k_L}}
$$
$$
+ \phi_S \cdot 0.32 \cdot Z_S^{-0.5} \frac{(\omega\tau_S)^2}{1 + 33.8 \cdot Z_S^{-1} \cdot (\omega\tau_S)^{2+k_S}} \tag{4.19}
$$
$$
\phi_L = 1 - \phi_S
$$
$$
k_S = 0.35
$$

Hereby, most of the parameters can be received from various methods, such as linear rheology or size exclusion chromatography (SEC):

The molecular weight of the components can be obtained by the SEC, which is linearly correlated to the number of entanglements. For comb-like structures, the molecular weight of the bb and the sc were determined during the synthesis. The molecular weight distribution of the bidisperse systems was obtained after blending and by analysis of the blending parameters.

To obtain the relaxation times of the respective components in bidisperse melts, the linear rheology results of the bidisperse melts were examined with the RDP model, which allows to access to the relaxation times (τ_L and τ_S) of its two monodisperse components. For the comb-like structures, the relaxation time of the bb (τ_{bb}) was obtained from the linear rheology, while the relaxation time of the sc (τ_{sc}) is more difficult to obtain, therefore, as a compromise τ_{sc} is a fitting parameter.

After receiving ϕ_L, ϕ_S, τ_L, τ_S, Z_L and Z_S (or ϕ_{bb}, ϕ_{sc}, τ_{bb}, τ_{sc}, Z_{bb} and Z_{sc} for combs) and setting $k_S \cong k_{sc} = 0.35$, due to the lack of experimental fulcrum paint, the parameter $k_L \cong k_{bb}$ is left as a free fitting parameter that itself shows a power law dependency on the volume ratio ϕ_L (or ϕ_{bb} for combs), refer to Equation 4.20.

$$
k_L(\phi_L) = a \cdot \phi_L^b \tag{4.20}
$$
$$
a = 0.35
$$
$$
b = -0.54
$$

The intrinsic non-linearity for bidisperse melts was modeled, by using observables and parameters which were obtained by different methods. The model shows good agreements with the experimental data and allows for deeper discussion of the meaning of the parameter $^3Q_0$. Concave peaks in the intrinsic non-linearity correspond with the relaxation times of the respective component of bidisperse polymer melts. Similarly, polymer combs can be modeled in the same way, showing agreement with the experimental data. However, the access to the relaxation time of the side chains of a comb from linear rheology is less straight-forward and was taken as a fitting parameter. It is likely that the relaxation time of the side chains of the comb and the relaxation time obtained by the intrinsic non-linearity mastercurve $^3Q_0(\omega)$ is corresponding, but this hypothesis requires further investigation and confirmation. However, the relaxation time of the entire comb polymer, which equals the relaxation time of the backbone, definitely agrees with the relaxation time from FT-rheology. Moreover, the trends of the slope parameter k can be predicted by a power law for linear bidisperse blends and for sufficiently monodisperse combs. This universal scaling law hints that the relaxation mechanism of bidisperse melts and polymer combs between the relaxation time of the long and short components (for linear bidisperse: τ_L and τ_S) or backbone and side chains (for combs: backbone: τ_L and side chain: τ_S) is similar. In Table 4.3 the parameters are summarized.

Table 4.3. Relaxation times of the PI model systems for $T_{\text{ref}} = 0\,^\circ\text{C}$. The molecular parameter are obtained through SEC characterization. The relaxation times are obtained by linear rheology, with the exception of τ_{sc}, which is a fitting parameter. The relaxation times obtained by linear rheology were applied in the modeling of the non-linearity.

sample name	ϕ_L	$M_{\text{n},L}$ [kg/mol]	$\tau_{d,L}$[s]	ϕ_S	$M_{\text{n},S}$ [kg/mol]	$\tau_{d,S}$[s]
PI-12%120k,88%31k	0.12	120	1.3	0.88	31	0.016
PI-35%120k,65%31k	0.35	120	2.5	0.65	31	0.03
PI-70%120k,30%31k	0.70	120	6.5	0.30	31	0.07
PI-120k $(= L)$	1.00	120	8.0	-	-	-
PI-31k $(= S)$	-	-	-	1.00	31	0.006

sample name	ϕ_{bb}	$M_{\text{n},bb}$ [kg/mol]	$\tau_{d,bb}$[s]	ϕ_{sc}	$M_{\text{n},sc}$ [kg/mol]	$\tau_{d,sc}$[s]
PI-120k-6.5-31k	0.35	120	800	0.65	31	0.6
PI-70k-9-14k	0.38	70	6.6	0.62	14	0.01

4.5 Normal forces and related non-linearity

Normal forces is the force orthogonal to the shear plane. As described in 2.3 *Rheology*, p. 17, the stress and strain of polymer melts was described in scalars. For a more in-dept and vector based analysis, tensors are required. The herein presented introduction based on *Polymer Rheology - Fundamentals and Applications* by Osswald and Rudolph [99]. In the following it is assumed that the shear plane is the $\vec{x}$, $\vec{y}$ plane and the orthogonal axis is $\vec{z}$. Therefore, the stress $\gamma_{x,y}$ is consists of its respective x and y components as in Equation 4.21.

$$\sigma_{x,y} = \frac{\partial \sigma_x}{\partial y} + \frac{\partial \sigma_y}{\partial x} \tag{4.21}$$

By adding the z-dimension, this relationship can be expressed in a tensor as in Equation 4.22.

$$\underline{\underline{\sigma}} = \sigma_{i,j} = \begin{bmatrix} \sigma_{x,x} & \sigma_{x,y} & \sigma_{x,z} \\ \sigma_{y,x} & \sigma_{y,y} & \sigma_{y,z} \\ \sigma_{z,x} & \sigma_{z,y} & \sigma_{z,z} \end{bmatrix} \tag{4.22}$$

Due to force balance, the tensor is symmetrical, consequently, $\sigma_{x,y} = \sigma_{y,x}$ applies.[9] Both $\sigma_{x,y}$ and $\sigma_{y,x}$ give shear modulus G and $\sigma_{x,x}$, $\sigma_{y,y}$ and $\sigma_{z,z}$ is the component corresponding to the normal force. All other terms are zero in oscillatory shear rheology, which allows a simplified expression as in Equation 4.23.

$$\underline{\underline{\sigma}} = \sigma_{i,j} = \begin{bmatrix} \sigma_{x,x} & \sigma_{x,y} & 0 \\ \sigma_{y,x} & \sigma_{y,y} & 0 \\ 0 & 0 & \sigma_{z,z} \end{bmatrix} \tag{4.23}$$

In the given case, the normal force is independent from the shear direction, which results in a response frequency which is double of the excitation frequency.[64] Moreover, the normal force is typically offset by a certain force. This means for a given strain (refer to Equation 4.24), the normal stress σ_N is described as presented in Equation 4.24.

$$\gamma(t) = \gamma_0 \cdot \sin(\omega \cdot t) \tag{4.24}$$

$$\sigma_N(t) = \sigma_{N,0} \cdot \sin(2(\omega \cdot t + \delta)) + \sigma_{N,c} \tag{4.25}$$

with the maximum amplitude of the normal stress $\sigma_{N,0}$, the same phase shift as in the previous sections δ and a stress offset of $\sigma_{N,c}$ that has a value of $\sigma_{N,c} = 0\,\mathrm{N}$ in the relaxed state.

---

[9]For systems in which this relationship does not apply, 2nd harmonic overtones are visible, and they are called *symmetry breaking*.

4.6 The non-linear of the normal forces a of polyisoprene

The acquisition of higher harmonics of normal forces is not an build-in feature of the employed ARES-G2 rheometer. However, the acquisition of the time data (inducing the current normal force F_N) of the experiments is possible. It can be Fourier transformed manually to acquire higher harmonics of the normal force. The time data of the normal forces F_N was acquired together with the time data of the stress for many model systems. In Figure 4.14 the normal force F_N of a bidisperse PI (PI-12%120k,88%31k) is presented. Outliers, as presented in **b)**, did occur in a significant amount of measurements. These outliers reduced the quality of the data in the inverses dimension significantly. Consequently, the quantification of the higher harmonics of the normal forces was not possible within this work. The origin of the outliers could be from the limitations of the force transducer or a fatally timed gap correction. Anyhow, the analysis of the non-linear response of the normal force from polymer melts, remains an interesting research topic for and should be further perused, when the technical limitations are resolved.
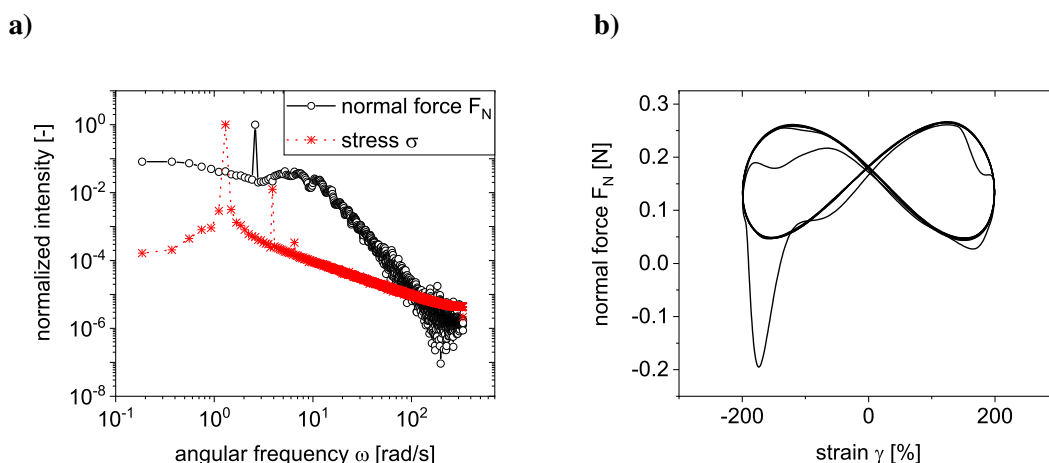
a)

b)

Figure 4.14. a) Fourier transformed spectra of the stress and the normal force F_N, of a bidisperse PI (PI-12%120k,88%31k) at $T = 7\,°C$, $\omega = 1.3\,\text{rad/s}$ and $\gamma_0 = 199\,\%$ and b) Lissajous figure of the normal force F_N. Both include 7 full cycles of strain oscillation. In a) the stress shows distinct peaks at the 1st, 3rd and 5th fundamental harmonic frequency. The normal forces F_N show a distinct peak at the double fundamental harmonic frequency, further harmonics are not visible. The signal/noise ratio is approximately 10. **b)** In the Lissajous plot a medium offset of about +0.15 N is visible, moreover the tilted 8 like shape is expected for responses with the double harmonic frequency. The mostly well reproducible trace shows few strong deviations of unknown origin, which likely dominates the FT-spectrum. These outliers appear in the majority of the measurements, and are most likely related to some gap adjustment mechanism in the instrument.

5 Broadband dielectric spectroscopy of polyisoprene model systems

Broadband dielectric spectroscopy (BDS) gives access to the dielectric constant $\epsilon^* = \epsilon' + i\epsilon''$ in a very broad frequency range (typically 0.1 Hz to 1 000 000 Hz) and temperature range. Corresponding to rheology, the time temperature superposition can be used to enlarge the observed frequency range. The BDS can be employed to observe the orientation modes of molecules. According to Stockmayer three types of modes for polymers are found, depending on the orientation of their molecular dipoles, for details the reader is referred to literature.[100] In summary, a 'type A' polymer (*e.g.,* 1,4-*cis* polyisoprene) has dipoles along its chain and the relaxation mode refers to the relaxation of the end-to-end vector $\vec{h}$ (refer to 2.4 *Dynamics and rheological properties of polymer melts*, p. 25), which is the longest relaxation time τ_d. 'Type B' polymers (e.g., poly(vinyl chloride)) show dipole moments orthogonal to the chain, the respective relaxation times are smaller compared to 'type A' polymers and typically involve 'skeletal chain motions' (refer to [100]). 'Type C' polymers (*e.g.,* poly(methyl methacrylate)) have a freely rotating group with a dipole, which is not restricted by the polymer chain.[101] Consequently, as the observed segments are smaller, the respective relaxation time are smaller compared to 'type B' polymers. For further introductions the reader is referred to the the literature[102–104].
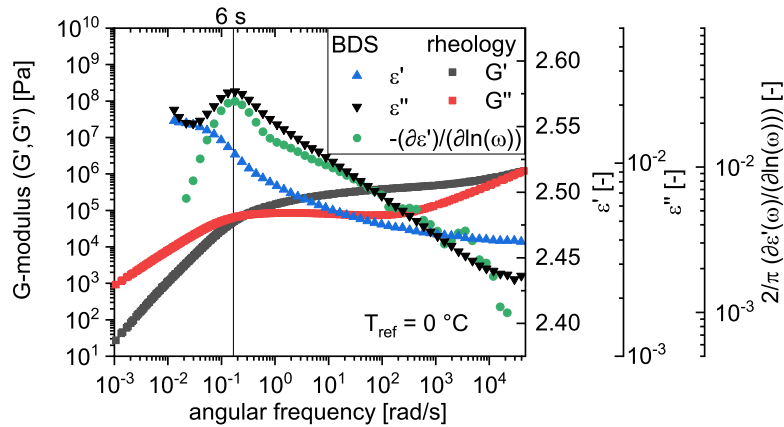

Figure 5.1. Oscillatory shear rheology and BDS on the same angular frequency axis pf the linear monodisperse sample PI-120k. The crossover of G' and G'', correlates well with the peak maximum in ϵ'' from BDS, which corresponds to the normal mode. Additional ϵ' and its derivative are presented. Since the former shows a deflection point at the normal mode, the derivative shows a peak at the normal mode. All experiments are referenced to $T_{\text{ref}} = 0\,°\text{C}$.

In this work the normal mode of the 'type A' polymer polyisoprene (PI) is in the spotlight, since the normal-mode corresponds to the terminal relaxation time. Herein, the BDS spectra of monodisperse PI are compared to linear bidisperse and comb structures. Finally, the BDS spectra are compared to the results of the FT-rheology. In Figure 5.1 the mechanical properties of a well entangled monodisperse polyisoprene melt ($M_\mathrm{n} = 120\,\mathrm{kg/mol}$, PI-120k) are compared to the respective dielectric properties. The terminal relaxation time of the polymer, obtained by rheology, correlates well with both the peak maximum of ϵ' and the peak maximum of the derivative (refer to Equation 5.1), which is know in literature[105]. Consequently, BDS is a suitable method to measure the relaxation times in PI melts, which can be used, *e.g.,* to predict the linear (oscillatory shear) mastercurve.

$$\epsilon_{der}(\omega) = \frac{\pi}{2} \frac{\partial \epsilon'(\omega)}{\partial \ln(\omega)} \tag{5.1}$$

In principle, BDS is not invasive and does not destroy the sample.[1] Practically, the applied voltage of 1.5 V sufficient to trigger side reactions such as carbonization of the polymer or stabilizer at the electrodes. Moreover, the electric field is partially orienting the dipoles, which in the case of PI is equivalent to the end-to-end vector. However, the applied frequencies are typically applied from the fastest to the slowest mode and the slow modes are faster than any external procedure, such as sample loading. Therefore, in a typical experiment the BDS is practically not changing the sample with respect ot the orientation distribution function.

5.1 BDS on a bidisperse PI system

Within the current section, the BDS of a bidisperse PI system is presented and discussed. The sample PI-12%120k,88%31k (refer to Table 4.1, p. 63) was characterized and is presented in Figure 5.2. The experiments were performed in a broad temperature range from $-55\,°\mathrm{C}$ to $130\,°\mathrm{C}$ and shifted using the TTS principle, resulting in a dynamic range of well above 13 decades. All angular frequencies are referenced to $T_\mathrm{ref} = 0\,°\mathrm{C}$, moreover, the ϵ'' is by T/T_ref(in [K]). In $\epsilon''(\omega)$ two modes are observed, which are the segmental relaxation time of $\tau = 6.7 \times 10^{-7}\,\mathrm{s}$ and a terminal relaxation time of the smaller chains of $\tau = 0.047\,\mathrm{s}$, the terminal relaxation time of the long chains is overlayed by different processes. Therefore, the derivative method (refer to Equation 5.1) is chosen [105], which allows for a higher dynamic range towards low frequency, and consequently enabling the detection of the terminal relaxation time of the longer polymer chain with $\tau = 4.5\,\mathrm{s}$. The terminal relaxation times of the small chain in this method with $\tau = 0.047\,\mathrm{s}$ and the segmental relaxation time of $\tau = 6.7 \times 10^{-7}\,\mathrm{s}$ are in good agreement with the modes obtained from ϵ''. The intensities in the peaks of the derivative method of both normal modes are for the longer chain $\epsilon_{der,L} = 10^{2.01}$ and for the smaller chain $\epsilon_{der,S} = 10^{1.56}$. Their ratio

---

[1]Linear oscillatory shear rheology does not destroy the sample, as the term linear implies. However, under larger deformations as required in FT-rheology, the sample is oriented. Depending on the sample, the system can recover or/and stay in an dynamic equilibrium.

$\epsilon_{der,L}/\epsilon_{der,S} = 0.35$ is in the range of the respective volume ratios multiplied with the square root of the molecular weight $\phi_L \sqrt{M_{n,L}}/(\phi_S \sqrt{M_{n,S}}) = 0.27.$[2] The dipole moment of PI is proportioal to its end-to-end vector, and the end-to-end vector scales with the square root of the molecular weight (refer to Equation 2.41 (p. 25) in 2.4 *Dynamics and rheological properties of polymer melts*).
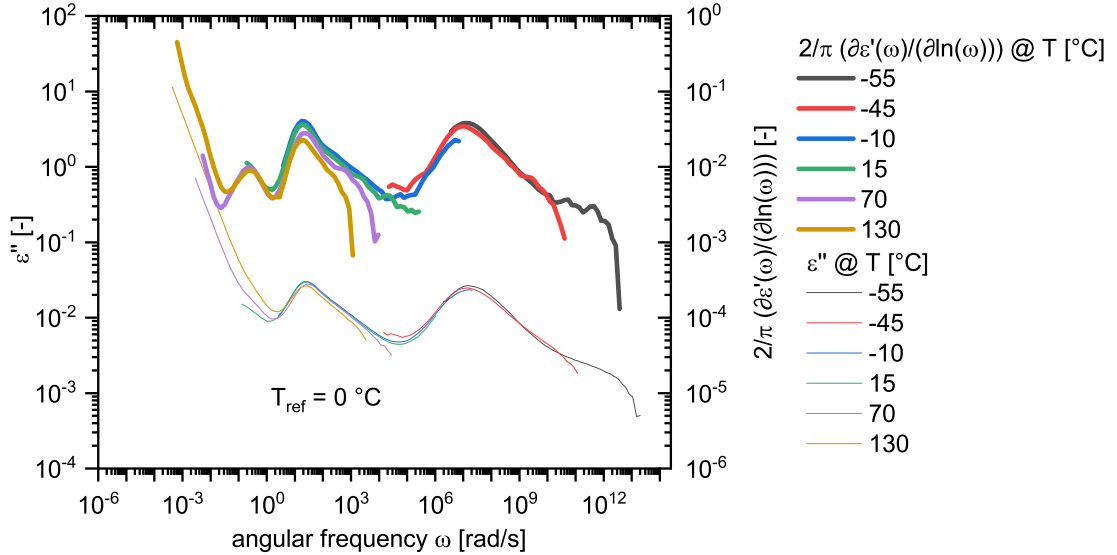

Figure 5.2. BDS of PI-12%120k,88%31k, selected temperatures are presented. Both, the trends in ϵ'' and in the derivative of ϵ' (refer to Equation 5.1) are presented. Since discrete derivatives are ill defined at the beginning and the end, the first and last three data points have been cut. After the shifting, the higher temperatures correspond to smaller frequencies and lower temperatures correspond to high frequencies. All experiments are referenced to $T_{ref} = 0\,°C$. By applying the TTS principle 16 decades of the dynamic range were covered.

As presented in Figure 5.2, BDS is a suitable method to quantify different normal modes in homopolymers. Consequently, the terminal relaxation time can be directly derived from the normal modes.

---

[2]The $\sqrt{M_n}$ is proportional to the mean end-to-end vector. The ratio of the peak intensities of ϵ_{der} fit the assumptions that the peak intensity is proportional to the volume ratio and proportional to the dipole moment, which is proportional to the end-to-end vector.

5.2 BDS on the PI comb PI-H68k-9-H14k

In the current section the BDS characterization of the PI comb PI-H68k-9-H14k is discussed and compared to the results of the oscillatory shear rheology experiments in the linear viscoelastic (LVE) regime and the non-linear VE regime. To do so, the sample was characterized by BDS in a wide temperature range from $-70\,°C$ to $100\,°C$. As an example in Figure 5.3, ϵ', ϵ'' and the derivative of ϵ' are presented for an experimental temperature of $50\,°C$.
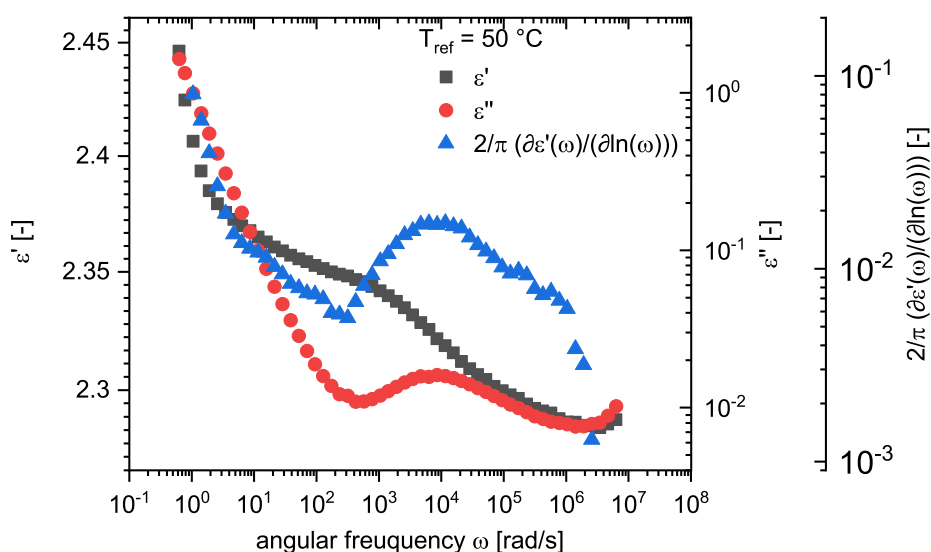
Figure 5.3. BDS of PI-H68k-9-H14k at $50\,°C$. ϵ', ϵ'' and the derivative of ϵ' are presented. The selected temperature covers the respective relaxation processes of the side arms and the backbone of the PI comb. The relaxation of the side arms are observed at $\omega = 8500\,rad/s$ in both, ϵ'' and the derivative of ϵ'. The relaxation of the backbone is observed at $\omega = 16\,rad/s$ in the derivative of ϵ' as a shoulder.

In Figure 5.4 the BDS results are compared to the results from rheology in the LVE regime and the non-linear VE regime, and in Table 5.1 the relaxation times are tabularized. The relaxation mode in the derivative of ϵ' towards small frequencies, agrees well with the relaxation times obtained from FT-rheology and linear rheology with $\tau_{BDS} = 4.13\,s$, $\tau_{FT\text{-rheology}} = 5\,s$ and $\tau_{linear\ rheology} = 6.6\,s$, respectively. For the results of the FT-rheology the reader is referred to 4 *Fourier transform rheology of homopolymer model system*, p. 54.

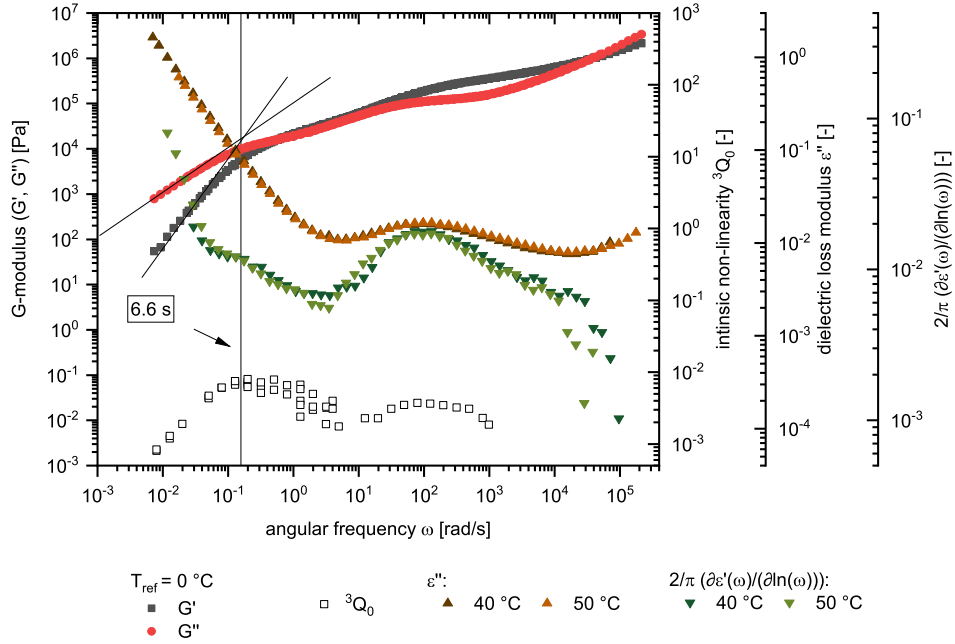**Figure 5.4.** BDS of PI-H68k-9-H14k referenced at $T_{\text{ref}} = 0\,^{\circ}\text{C}$. ϵ'' and the derivative of ϵ' are presented, and additional, the rheology results of the linear and non-linear oscillatory shear experiments as a comparison. The peak in the derivative of ϵ' towards low frequency matches well with the relaxation time obtained from linear (crossover frequency) and non-linear (maximum of $^{3}Q_0$) rheology. Moreover, the relaxation of the sidearm, observed by the mode towards higher frequencies, agrees well with the results from FT-rheology (maximum of $^{3}Q_0$).

Table 5.1. List of relaxation times of the PI comb PI-H68k-9-H14k obtained by BDS. Where $\tau_{d,bb}$ and $\tau_{d,sc}$ are the terminal relaxation times of the backbone and the side chains, respectively, and τ_s is the segmental relaxation time.

sample name	$\tau_{d,bb}[\text{s}]$	$\tau_{d,sc}[\text{s}]$	$\tau_s[\text{s}]$
PI-H68k-9-H14k	4.1	1.4×10^2	1.2×10^{-7}

To the best of the author's knowledge, the normal mode of an entangled backbone of a polymer comb has not been characterized, yet. Consequently, herein we show that BDS can be used to access both normal modes in a PI comb, the sidearms and the backbone. However, this technique is limited by the conductivity of the material towards low frequencies and high temperature.

5.3 Conclusion

Within this chapter, PI model systems were characterized, including a linear monodisperse polymer melt, a linear bidisperse polymer melt and a comb polymer melt. For the bidisperse system and the comb, the normal modes of both components (long and short chains in the bidisperse system; side chains and backbone in the comb) were distinguishable. Moreover, the obtained relaxation times match the relaxation times obtained by linear rheology and FT-rheology.

6 Multiquantum time domain nuclear magnetic resonance spectroscopy on PI model systems

Multiquantum-time domain-nuclear magnetic resonance spectroscopy (MQ-TD-NMR) was employed to monitor the degree of residual orientation of polymer chain segments and the ratio of chain segments with residual orientation. For the theoretical background, the reader is referred to 2.5 *Nuclear magnetic resonance (NMR) spectroscopy and relaxometry*, p. 29. Since the double quantum contribution is the strongest, it is often referred to as double quantum (DQ)-NMR.

Herein this chapter three model systems are investigated. In section 6.1 *DQ-NMR on sequentially labeled linear PI homopolymers*, 83, linear labeled polymer melts are investigated. In 6.2 *DQ-NMR on model comb systems*, p. 86, a polymer comb melt is investigated. And in 6.3 *TD-NMR on partially deuterated comb polyisoprene model systems*, p. 87, a set of partially deuterated and protonated comb polymer melts are compared.

6.1 DQ-NMR on sequentially labeled linear PI homopolymers

Two sequentially labeled (proton and deuteron) PI samples have been synthesized and prepared. The sample details are listed in Table 6.1. The results for the sample D48k-H193k-D48k at 326 K are presented in Figure 6.1. In Figure 6.1 **b)** the ratio of unrestricted protons is approximately 3 %, which includes the 1 wt% stabilizer, other small molecules and isolated protons. The observed part of D48k-H193k-D48k, which is the protonated middle part, is consequently still fully restricted within its part of the dynamic tube.

Table 6.1. Molecular information on the labeled tri-block homopolymers

Name	M_n [kg/mol] 1st part	M_n [kg/mol] 2nd part	M_n [kg/mol] 3rd part
H25k-D100k-H25k	H 25	D 100	H 25
D48k-H193k-D48k	D 48	H 193	D 48

In the case of H25k-D100k-H25k, where the inner part of the polymer is invisible, the fraction of chain segments, which are relaxed and therefore, without residual orientation, reached 53 % at $T = 326$ K. This amounts to a chain length of 13 kg/mol or about two entanglement molecular weights (refer to Figure 6.2). These results are in agreement with the reptation and tube model, since the relaxation of the polymer
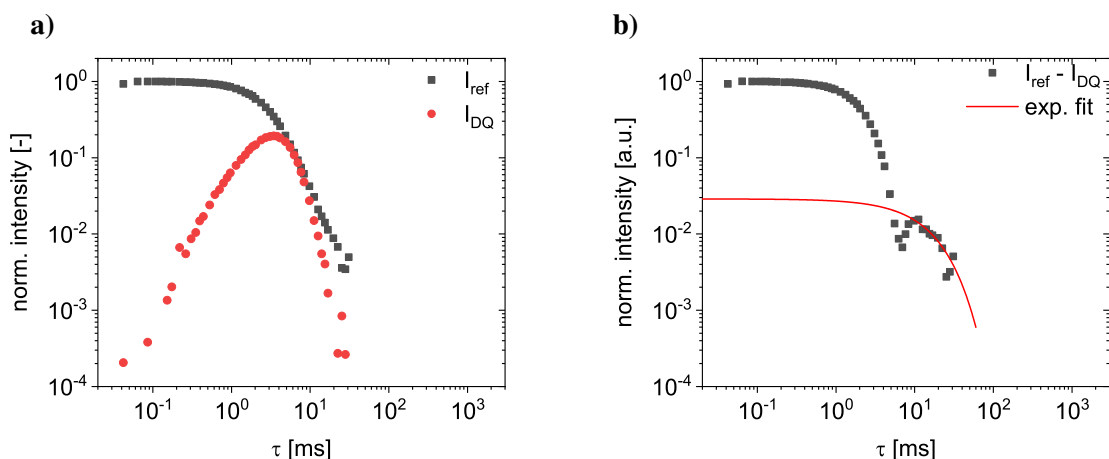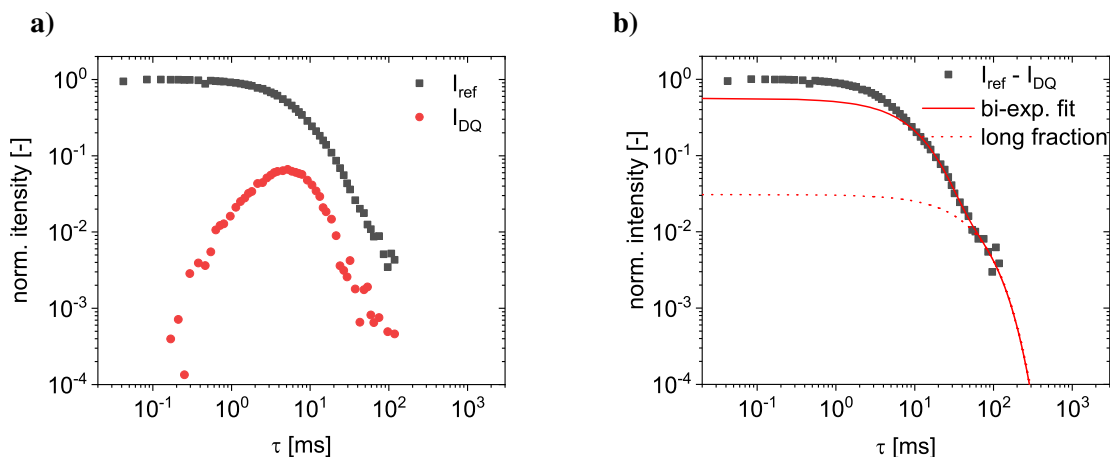
Figure 6.1. ^{1}H DQ-results of the sample D48k-H193k-D48k at $T = 326$ K. **a)** The raw data obtained by a DQ experiment, normalized to the maximum value. The reference, includes all protons, without DQ-transition, and the DQ signal includes all protons, that were subject to a DQ-transition. **b)** For times long times (here $\tau > 10$ ms), I_{ref} and I_{DQ} have to be equal for a coupling system. The difference of $I_{ref} - I_{DQ}$ amounts to the unrestricted fraction of the sample and is here determined by an exponential fit, to extrapolate to $\tau = 0$.

chains starts at the outer most part of the chains and progresses to the inner most part of the polymer chain.

Figure 6.2. ^{1}H DQ-results of the sample H25k-D100k-H25k at $T = 326$ K. **a)** The raw data obtained by a DQ experiment, normalized to the maximum value. The reference, includes all protons, without DQ-transition, and the DQ signal includes all protons, that were subject to a DQ-transition. **b)** The majority of the sample is part of to isotropically relaxed fraction. Moreover, two different exponential decays are monitored. The tail was fitted with a bi-exponential function. One decay with a 3 % fraction and a relatively slow decay, related to small molecules. The second exponential decay with a share of 53 % originates from the fraction of the polymer segments without local residual orientation.

The goal of the DQ-measurement is the monitoring of the DQ-coherence, which includes the observation of the dipolar coupling rate that can directly be translated to a residual orientation. To do so, the experimental data is fitted with Equation 6.1 and Equation 6.2[106] in Figure 6.3.[1] The κ is the negative slope of the

---

[1]$I_{\Sigma MQ} = I_{ref} + I_{DQ}$; $I_{\Sigma MQ}$ without the tail and I_{DQ} are fitted collectively with the respective functions.

segmental orientation autocorrelation function. Different slopes relate to different dominating relaxation processes, such as 0.25 for constrained Rouse, 0.5 for reptation and infinity for free diffusion, for details the reader is referred to the respective literature [107, 108].

$$I_{DQ} = \exp\left(-\frac{2\tau}{T_2}\right) \exp\left(\frac{-0.2D_{res}^2}{(\kappa-2)(\kappa-1)}\left(\left(\kappa-\kappa^2\right)t_0^2 + \left(2\kappa^2-4\kappa\right)\tau t_0 + 2\tau^{2-\kappa}t_0^\kappa\right)\right) \qquad (6.1)$$

$$\cdot \sinh\left(\frac{0.2D_{res}}{2(\kappa-2)(\kappa-1)}\left(\left(\kappa^2-\kappa\right)t_0^2 + \left(2^{3-\kappa}-4\right)\tau^{2-\kappa}t_0^\kappa\right)\right)$$

$$I_{\Sigma MQ} = \exp\left(-\frac{2\tau}{T_2}\right) \exp\left(\frac{-0.2D_{res}}{(\kappa-2)(\kappa-1)}\left(\frac{3}{2}\left(\kappa-\kappa^2\right)t_0^2 + \left(2\kappa^2-4\kappa\right)\tau t_0 + (4-2^{2-\kappa})\tau^{2-\kappa}t_0^\kappa\right)\right)$$

$$\qquad (6.2)$$
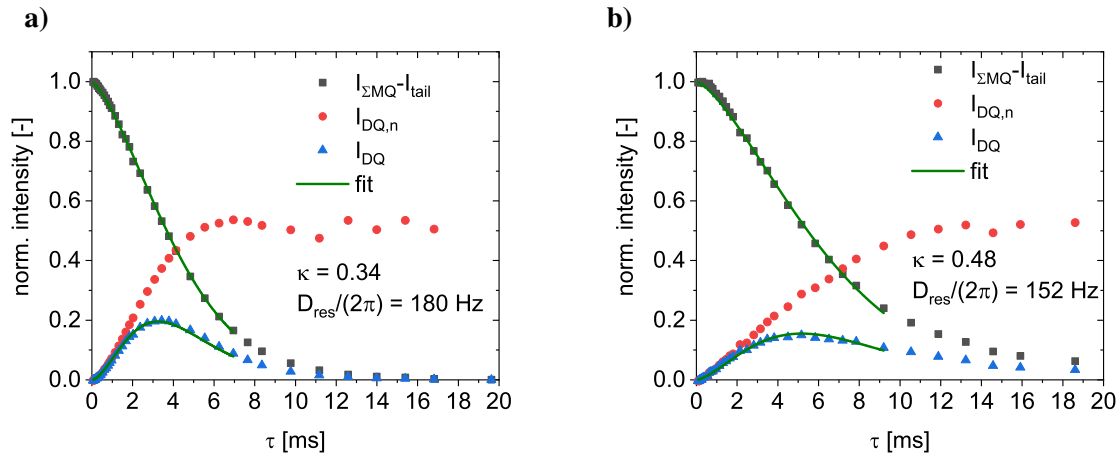
Figure 6.3. Modeling of the ^{1}H DQ-experiments with Equation 6.1 and Equation 6.2.[106] The modeling allows access to the dipolar coupling frequency and the κ value, which enables the quantification of the mode of relaxation. **a)** shows sample D48k-H193k-D48k and **b)** shows sample H25k-D100k-H25k .

Since D48k-H193k-D48k exhibits no tail that corresponds to polymer chains, the respective chain parts are still in their dynamic tube. However, sample H25k-D100k-H25k exhibits a 50 % tail, consequently half of the H25k block is relaxed (in the relevant time scale of about 100 Hz), which is a total polymer molecular weight of 13 kg/mol or about two entanglements.

6.2 DQ-NMR on model comb systems

The PI comb (PI-120k-6.5-31k) was characterized in the same way, as the two partially deuterated PI model systems as a fully protonated test system to evaluate the dimensions of deuteron labeled model systems. Figure 6.4 presents the DQ results at $T = 326\,$K. At $T = 326\,$K the polymer comb shows an isotropic fraction of 39 %. The total molecular weight of the comb is $M_n = 320\,$kg/mol, and it has approximately 7 side chains per backbone. Together with the 2 chain ends of the backbone, the total amount of chain ends per comb is 9. Consequently, 39 % of 320 kg/mol distributed to 9 chain ends per comb is 14 kg/mol. This result is comparable to the 13 kg/mol of (labeled) linear chains (sample H25k-D100k-H25k) in *DQ-NMR on sequentially labeled linear PI homopolymers* (p. 83). In Figure 6.5 the change in conformation is illustrated in a scheme.
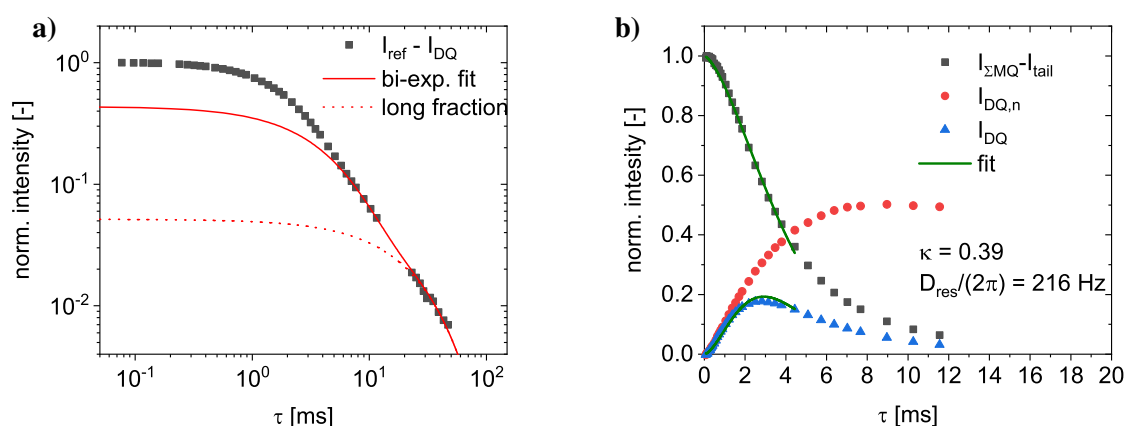
Figure 6.4. Modeling of the ^{1}H DQ-results as introduced in 6.1 *DQ-NMR on sequentially labeled linear PI homopolymers*. The sample is PI-120k-6.5-31k and the temperature is $T = 326\,$K. **a)** The sample shows two exponential tails with a fraction of 5.14 % ($T_2 = 22.2\,$ms) and 38.7 % ($T_2 = 4.02\,$ms), respectively. While the slow relaxing fraction refers to small molecules like stabilizer or chain ends, the faster relaxing tail, corresponds to isotropic relaxed polymer chains. **b)** Evaluation of the DQ experiment with the model from Equation 6.1 and Equation 6.2.
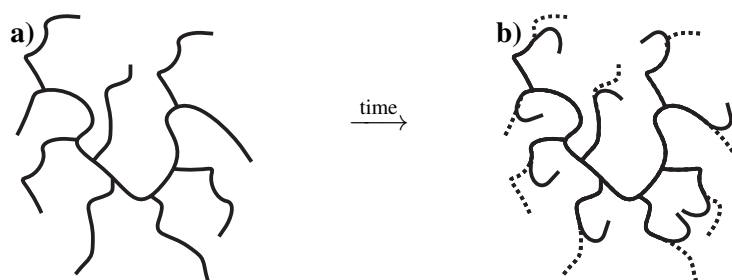

Figure 6.5. a) Scheme of the polymer comb PI-120k-6.5-31k. Even though the entanglement molecular weight is $M_e = 5.5\,$kg/mol the polymer chains have not been drawn entangled, to keep it comprehensible. **b)** Scheme of a polymer comb relaxation. The dotted lines represent the state before relaxation as in **a)**. The full line equates to the new conformation. Herein, approximately 39 % of the polymer chain is relaxed, the relaxation starts at the chain ends and goes towards the middle of the backbone. Practically, there is no difference between side chains and the end groups of the backbone. This relaxation corresponds to time scales of about 100 Hz at $T = 326\,$K.

6.3 TD-NMR on partially deuterated comb polyisoprene model systems

In the following section the TD-NMR characterization of two polyisoprene combs is reported and discussed. The synthesis is reported in 3.9 *Synthesis of partially a deuterated PI comb* (p. 50). Both combs (PI-D72k-9-H14k and PI-H68k-9-H14k) have comparable lengths of the backbone and the side chains, and the number of side chains.

The partially deuterated comb PI-D72k-9-H14k can be characterized in both ^{1}H-NMR and ^{2}H-NMR and is therefore a way to directly characterize the chain dynamics of the backbone or the side chains. Moreover, comb PI-H68k-9-H14k, which shows a superposition of the side chains and the backbone in ^{1}H-NMR can be compared to the chain dynamics of the side chains of the comb PI-D72k-9-H14k to yield the chain dynamics of the backbone as the difference. In principle, DQ-NMR can similarly be applied in ^{2}H-NMR. Practically, it is much harder to yield quantifiable information, since on the one hand, the smaller γ results in a much smaller signal, refer to section 2.5.1 *Zeeman interaction*, p. 30. On the other hand, besides the dipolar interaction, the quadrupolar interaction is observed as well, and consequently, the experiment might be dominated by quadrupolar interactions. Moreover, the quadrupolar interaction can be partially reduced by the fast spinning of the methyl-groups in the PI. Consequently, two different decays are expected.

The work within this section, 6.3 *TD-NMR on partially deuterated comb polyisoprene model systems*, and the respective subsections *^{1}H-DQ-NMR on the partially deuterated comb PI-D72k-9-H14k*, *^{2}H-DQ-NMR on the partially deuterated comb PI-D72k-9-H14k* and *^{1}H-DQ-NMR on the fully protonated comb PI-D68k-9-H14k*, is the result of a collaboration, therefore, the distinct contributions of this project is elaborated for clarity. Samples PI-D72k-9-H14k and PI-H68k-9-H14k were synthesized, prepared for characterization and characterized with SEC, (FT-)rheology, BDS and DSC by the author of this work. TD-NMR (^{1}H-DQ-NMR and ^{2}H-DQ-NMR) characterization was done by Mr. F. Shahsavan from the group of Prof. Dr. K. Saalwächter at the Martin-Luther-University Halle-Wittenberg, who was providing the author with the raw data. The data evaluation of the raw data, as presented in this section, is the work of the author within this thesis.

Table 6.2. The T_1-results of the PI combs PI-D72k-9-H14k and PI-H68k-9-H14k at $T = 100\,°\mathrm{C}$ modeled with Equation 6.3.
*) Fit values of T_1 smaller than the smallest τ are rounded to 0 ms, due to the lack of fulcrum points.

Name	Nucleus	A_a [%]	A_b [%]	$T_{1,a}$ [ms]	$T_{1,b}$ [ms]
PI-H68k-9-H14k	[1]H	1	99	0*	61
PI-D72k-9-H14k	[1]H	3	97	0*	62
PI-D72k-9-H14k	[2]H	49	51	0*	47

The longitudinal relaxation time (T_1) of samples PI-D72k-9-H14k and PI-H68k-9-H14k were obtained for ^{1}H and ^{2}H-NMR in saturation recovery experiments (SR) and modeled with a bi-exponential fitting function Equation 6.3.
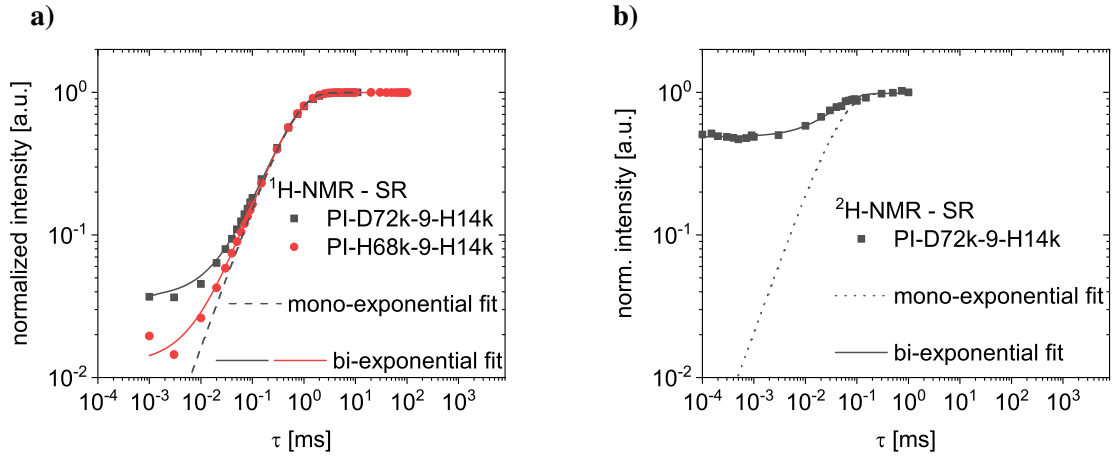
Figure 6.6. ^{1}H and ^{2}H saturation recovery (SR) experiments of the PI combs PI-D72k-9-H14k and PI-H68k-9-H14k at $T = 100\,°\text{C}$. All fitting results are presented in Table 6.2. In **a)** the ^{1}H SR results of both combs are presented and modeled by a bi-exponential build-up type function as in Equation 6.3. The dominant relaxation mechanism with a $T_1 = 61$ ms, which is highlighted, is the same for both samples, considering small uncertainties. In **b)** the ^{2}H results are presented, where an exponential build-up mechanism with a strong plateau ($\tau = 10^{-4}$ ms to 10^{-3} ms) with 49 % intensity is found. The relaxation time for the remaining 51 % is $T_1 = 47$ ms. The mono-exponential part without the plateau is highlighted. This plateau possibly originates from the residual electric wave of the excitation pulse (dead time).

$$I = A_a(1 - \exp(-\tau/T_{1,a})) + A_b(1 - \exp(-\tau/T_{1,b})) \tag{6.3}$$

$$A_a + A_b \overset{!}{=} 1$$

The results for $T = 100\,°\text{C}$ are presented in Table 6.2 and visualized in Figure 6.6. For both samples the T_1 relaxation times in ^{1}H-NMR is the same with approximately $T_1 = 61$ ms, which is to be expected, since the T_1 times for the same polymer and temperature are typically the same. Both samples exhibit a small plateau at small τ-values, which likely originates from the noise level. The T_1 relaxation time for the sample PI-D72k-9-H14k in ^{2}H shows a plateau of approximately 50 % and an exponential build-up of 50 % and a relaxation time of $T_1 = 47$ ms. This strong plateau of 50 % is unexpected and not reported in literature to the best of the authors knowledge. Saturation recovery experiments are well-known in literature, and these authors do not report a plateau[109]. This might be an instrumental artifact, *e.g.,* residual voltage from the excitation pulses (dead time problem), since typical dead times are in the range of 1 µs to 10 µs, which equals to the range of the plateau.

6.3.1 ^{1}H-DQ-NMR on the partially deuterated comb PI-D72k-9-H14k

The ^{1}H-DQ-NMR characterization of sample PI-D72k-9-H14k is presented within this section. Since NMR is sensitive towards the chosen nucleus only, the side chains of this comb are observed exclusively in ^{1}H-DQ-NMR. The observed chain parts are visualized in Figure 6.7.
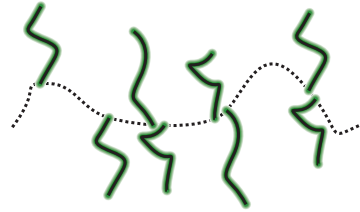

Figure 6.7. Scheme of the ^{1}H-NMR measurement of PI-D72k-9-H14k, the observed side chain segments are highlighted in green.

The sample was characterized at different temperatures $T = 30\,°\mathrm{C}$ to $100\,°\mathrm{C}$ in $10\,\mathrm{K}$ steps. The DQ-results and the tail fitting with a bi-exponential fit for three selected temperature is presented in Figure 6.8 and summarized in Table 6.3. The applied fit function is presented in Equation 6.4.

$$I_{tail} = A_a \exp(\tau/T_{2,a}) + A_b \exp(\tau/T_{2,b}) \tag{6.4}$$
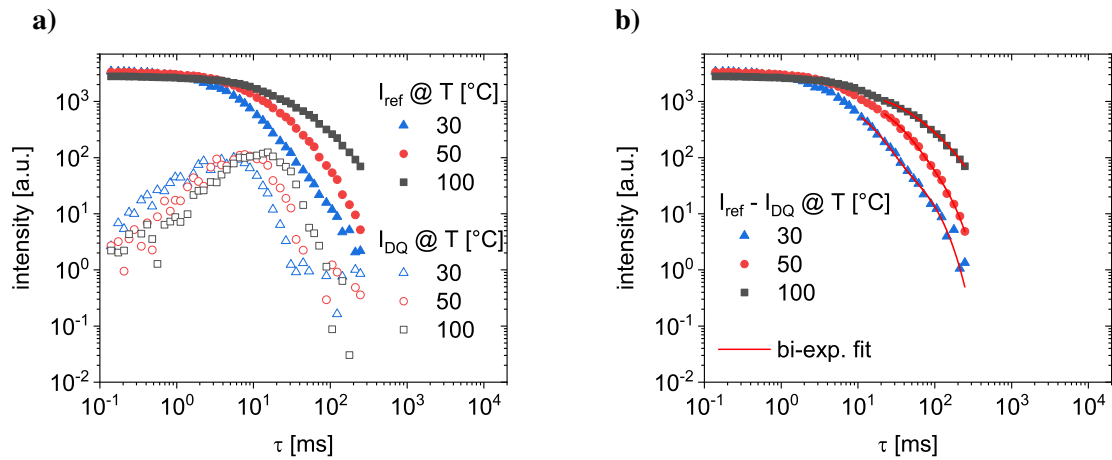
Figure 6.8. The DQ-measurement in ^{1}H-NMR for the sample PI-D72k-9-H14k at three selected temperatures. In **a)** the reference (I_{ref}) and the DQ (I_{DQ}) signal are presented. In **b)** the difference of the reference and the DQ signal is presented, with the respective fitting of the tails.

The modeling of the tail requires two exponential decays. The coefficient for the faster decay remains at around 40 %, which is independent from temperature. However, the second decay shows an increase in its ratio as the temperature increases. The fraction starts at approximately 3 % at $T = 30\,°\mathrm{C}$ and ends with approximately 16 % at $T = 100\,°\mathrm{C}$. The constant 40 % rapid decay is important, otherwise, the normalized DQ build-up $I_{DQ,n}$ cannot reach the plateau of 0.5 for infinite times. To illustrate the necessity to subtract the two tails, the results with the subtraction of a single tail only is presented in Figure 6.9. In

Table 6.3. The mobile tail fit results of the DQ-^{1}H-NMR measurement of PI-D72k-9-H14k at different temperatures. The coefficients are presented as the fraction of the total intensity. The respective fractions are named a and b.The fits have few fulcrum points to precisely determine the a fraction, moreover, $T_2 \leq T_1$, therefore, the values of precisely $T_{2,a}$ are likely to be overestimated.

Temperature [°C]	A_a [%]	A_b [%]	$A_a + A_b$ [%]	$T_{2,a}$ [ms]	$T_{2,a}$ [ms]
100	41.9	17.4	59.3	32.6	124
90	38.5	16.1	54.6	27.4	99.0
80	38.2	8.97	47.2	31.8	99.3
70	48.7	7.62	56.3	19.4	189
60	31.2	8.86	40.0	21.6	65.5
50	40.1	7.50	47.6	18.6	61.8
40	37.1	3.69	40.8	16.0	65.9
30	41.0	3.57	44.6	8.88	44.4

Figure 6.9, the normalized DQ build-up $I_{DQ,n}$ is between the subtraction of the slow decaying tail and of both components of the tail, which is an indication of unsuccessful data processing. The slow decaying tail fraction is increasing with temperature. The increase can be modeled with an exponential growth which is visualized in Figure 6.10. Hereby, a 100 % tail fraction, which is equivalent to a fully relaxed polymer, is expected at approximately $T = 177\,°C$.

By comparing the relaxation times in Table 6.3 the transverse relaxation times ($T_{2,a}$ and $T_{2,b}$) increases with temperature, which is to be expected.
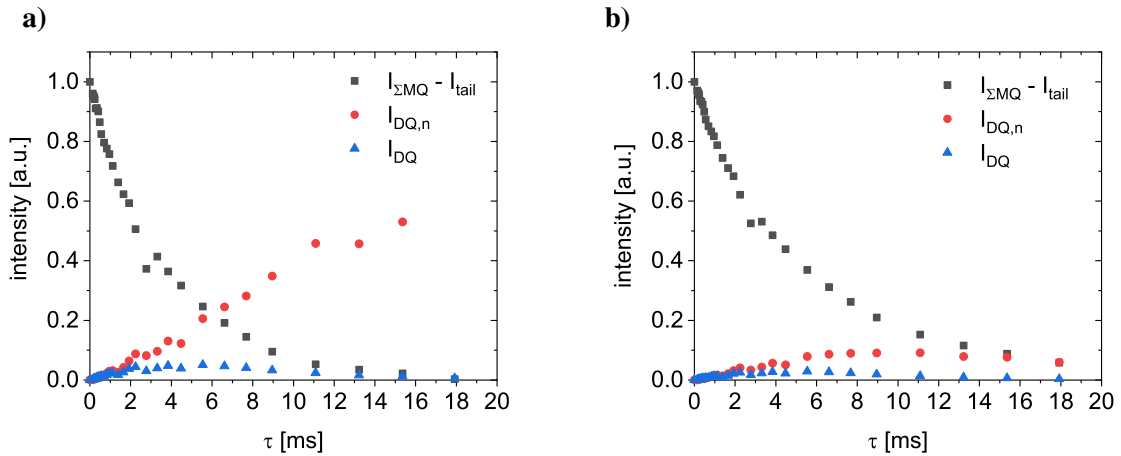
a)

b)

Figure 6.9. Different data processing procedures of the same raw DQ data of the sample PI-D72k-9-H14k at 30 °C. In **a)** both components a and b of the tail are subtracted, the resulting $I_{DQ,n}$ reaches the plateau at 0.5. In **b)** only the slowly decaying fraction b is subtracted, consequently the plateau in $I_{DQ,n}$ is not reached, even at a time far greater than 20 ms. For details of the fit parameters refer to Table 6.3.
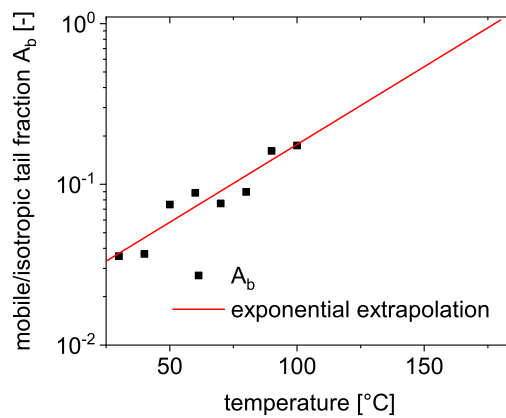
Figure 6.10. The fraction of the slow decaying tail A_b (refer to Table 6.3) of sample D48k-H193k-D48k. The results are extrapolated empirically with an exponential fit: $\exp((T - T_0)/d)$. Hereby, $T_0 = 177\,°C$ is the temperature, where a tail fraction of $100\,\%$ is expected and $d = 44.8\,K^{-1}$ is a fitting parameter. The tail (fraction) is the fraction of the polymer that is relaxed (has no residual orientation), consequently, T_0 is the temperature at which the entire system is relaxed.

6.3.2 ^{2}H-DQ-NMR on the partially deuterated comb PI-D72k-9-H14k

Herein, the ^{2}H-DQ-NMR measurements of sample PI-D72k-9-H14k is reported in the temperature range of 30 °C to 100 °C in 10 K steps. In Figure 6.11 the observed chain parts are highlighted.
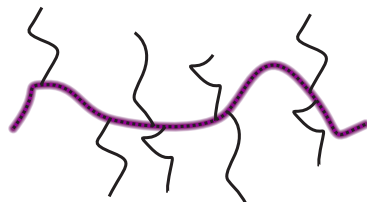
Figure 6.11. Scheme of the ^{2}H-NMR measurement of PI-D72k-9-H14k, the observed chain parts are highlighted in magenta.

The selected temperatures are presented in Figure 6.12 and the summary in Table 6.4. The tail fraction is increases with the temperature. By extrapolating the results, a temperature of 161 °C is expected for full relaxation as presented in Figure 6.13. The transverse relaxation time is increasing with temperature, because the mobility of the chains is increasing as well.
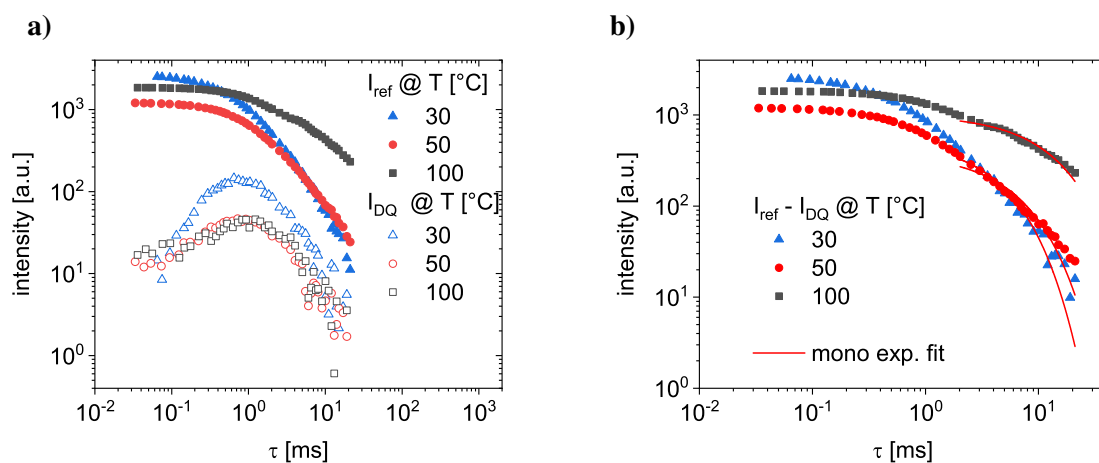
Figure 6.12. The ^{2}H-DQ-NMR measurements of sample PI-D72k-9-H14k at the three selected temperatures. In **a)** the reference (I_{ref}) and the DQ (I_{DQ}) signal are presented. In **b)** the difference of the reference and the DQ signal is presented, with the respective fit of the tails.

92

Table 6.4. The tail fit results of DQ-^{2}H-NMR measurement of PI-D72k-9-H14k at different temperatures. Including the tail fraction A and the T_2 time, refer to Equation 6.4.

Temperature [°C]	A [%]	T_2 [ms]
100	48.1	12.4
90	42.2	9.96
80	41.1	8.34
70	37.5	7.41
60	33.6	6.59
50	28.8	5.85
40	23.5	5.47
30	18.7	4.00
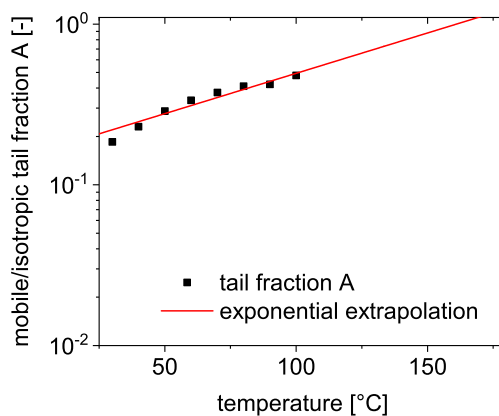
Figure 6.13. The fraction of the tail A (refer to Table 6.4) in deuteron NMR of sample PI-D72k-9-H14k. The results are extrapolated empirically with a mono-exponential fit: $\exp((T - T_0)/d)$, the used unit for T is [°C], but the fit results would be equivalent with any other unit. Hereby, $T_0 = 161\,°\text{C}$ is the temperature, where a tail fraction of $100\,\%$ is expected and $d = 86.5\,\text{K}^{-1}$ is a fitting parameter. The tail (fraction) is the fraction of the polymer that is relaxed (has no residual orientation), consequently, T_0 is the temperature at which the entire system is relaxed.

6.3.3 ^{1}H-DQ-NMR on the fully protonated comb PI-D68k-9-H14k

The DQ-characterization of sample PI-H68k-9-H14k is presented within this section, in Figure 6.14 the chain parts are visualized.
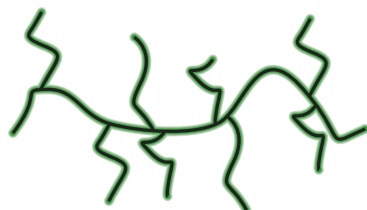

Figure 6.14. Scheme of the ^{1}H-NMR measurement of PI-H68k-9-H14k, the observed chain parts are highlighted in green, which includes the entire polymer.

Since this sample is not labeled, the results are a superposition of all molecular dynamics. The sample was characterized at different temperatures from 30 °C to 130 °C in 10 K steps. The DQ-results and the tail fitting with a bi-exponential fit for three selected temperature is presented in Figure 6.15 and summarized in Table 6.5. The fit function is Equation 6.4. The fraction of the tail was obtained as a function of time. This isotropically relaxed fraction as a function of temperature is visualized in Figure 6.16, the extrapolation of the tail predicts a full isotropic relaxation at $T = 149$ °C.

Table 6.5. The tail fit results of DQ-^{1}H-NMR measurement of sample PI-H68k-9-H14k at different temperatures. The coefficients are presented as the fraction of the total intensity. The respective fractions are named a and b. Fraction b was not obtained for $T > 50$ °C, since the received fraction would exceed 100 % or no additional tail was observable

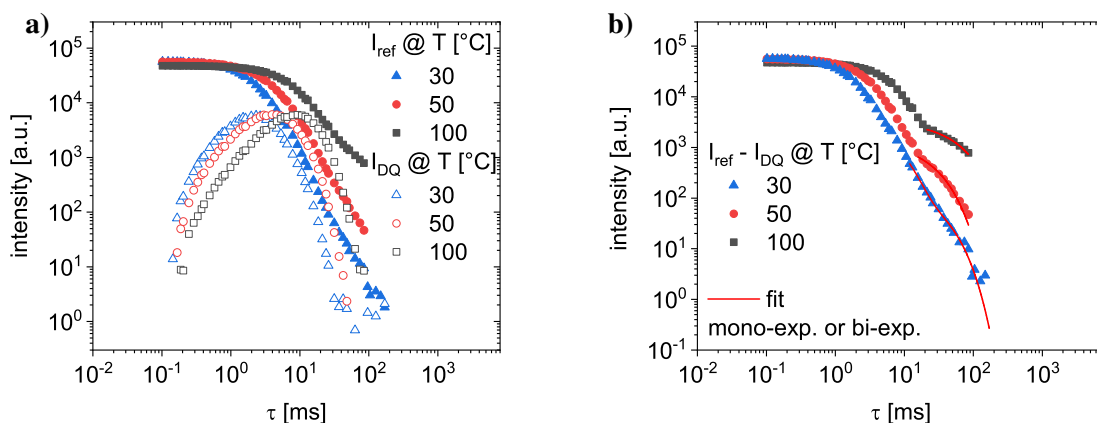| Temperature [°C]	A_a [%]	A_b [%]	$A_a + A_b$ [%]	$T_{2,a}$ [ms]	$T_{2,b}$ [ms]
130	41.3	-	41.3	83.4	-
120	42.5	-	42.5	75.3	-
110	26.0	-	26.0	39.9	-
100	7.41	-	7.41	56.7	-
90	5.3	-	5.3	49.1	-
80	4.47	-	4.47	40.5	-
70	3.21	-	3.21	37.6	-
60	2.82	-	26.8	21.66	-
50	1.7	50.5	52.2	26.6	3.31
40	0.7	15.1	15.8	26.9	4.6
30	0.3	7.9	8.12	26.6	4.8

Figure 6.15. The DQ-measurement in ^{1}H-NMR for sample PI-H68k-9-H14k at the three selected temperatures. In **a)** the reference (I_{ref}) and the DQ (I_{DQ}) signal are presented. In **b)** the difference of the reference and the DQ-signal is shown, with the respective fitting of the tails.
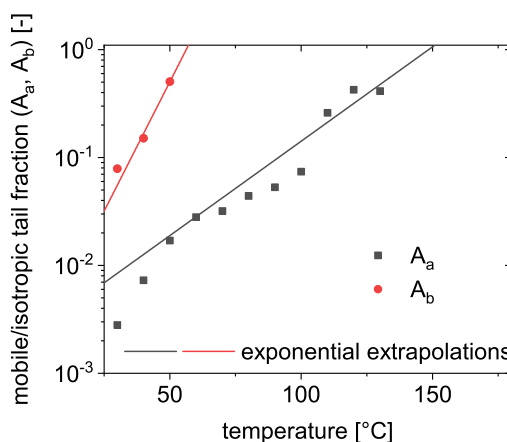

Figure 6.16. The fraction of the tail A_a and A_b, refer to Table 6.3, of sample PI-H68k-9-H14k. The results are extrapolated empirically with a mono-exponential fit ($\exp((T - T_0)/d)$) to obtain the temperature with an expected tail fraction of 100 %. The tail (fraction) is the fraction of the polymer that is relaxed (has no residual orientation), consequently, T_0 is the temperature at which the observed system is relaxed.
For the fraction a the temperature, where a tail fraction of 100 % is expected is $T_0 = 149\,°\mathrm{C}$ and d is a fitting parameter ($d = 24.8\,\mathrm{K}^{-1}$).
For the fraction b the temperature, where a tail fraction of 100 % is expected is $T_0 = 56.2\,°\mathrm{C}$ and d is a fitting parameter ($d = 9.07\,\mathrm{K}^{-1}$).

6.3.4 Conclusion on the DQ-NMR of partially deuterated model systems

In the current chapter DQ-NMR in ^{1}H-and ^{2}H-NMR was used to characterize two samples PI-D72k-9-H14k and PI-H68k-9-H14k. In this work the focus was on the quantification of the isotropic tail as a function of temperature. The temperature, at which the entire polymer is expected without residual orientation, is extrapolated and for all samples in the range of 149 °C to 177 °C. The respective temperatures are comparable to the crossover to the flow regime in rheology. The polymer with the given architecture is consequently fully relaxed in the NMR experiments for $\approx T_g + 200\,\mathrm{K}$. The observation of the bb and the sc with ^{2}H-NMR and 1 H-NMR, respectivly of the sample PI-D72k-9-H14k, extrapolate to similar temperatures, which is unexpected, since the side chains should be relaxed at much lower temperatures. Compared to the results in rheology, where the flow regime is observed for frequency scales of less than 10^{-1} rad/s ($T_{ref} = 0\,°\mathrm{C}$), this temperature is much higher. These finding are discussed in 7 *Comparison of the different techniques of the PI comb PI-H68k-9-H14k*, p. 96.

7 Comparison of rheology, FT-rheology, BDS and TD-NMR of the PI comb PI-H68k-9-H14k

The PI comb PI-H68k-9-H14k was characterized towards its mechanical properties and its molecular dynamics excessively with different techniques. The molecular information are listed in Figure 3.14, p. 51. The dynamics were investigated with TD-NMR (refer to chapter 6.3.3 *^{1}H-DQ-NMR on the fully protonated comb PI-D68k-9-H14k*, p. 94) and BDS (refer to chapter 5.1 *BDS on a bidisperse PI system*, p. 79). In addition to that, the mechanical properties were investigated in 4.3 *FT-Rheology on comb polymers*, p. 68.

The relaxation time obtained from rheology, FT-rheology and BDS are in good agreement to each other as presented in Figure 7.1. In addition to that, in Figure 7.1 the temperature shifted relaxation times from different techniques that are obtained through applying the WLF-equation are presented together with the extrapolated temperature for full isotropic relaxation, which was obtained by TD-NMR. The temperature of fully isotropic relaxation from the TD-NMR and the temperature dependent relaxation time from the mechanical/electrical analysis show a transition show a crossover at frequency values of $\omega/(2\pi) = 69\,\text{Hz}$ for the and $\omega/(2\pi) = 1600\,\text{Hz}$ for the side chains.
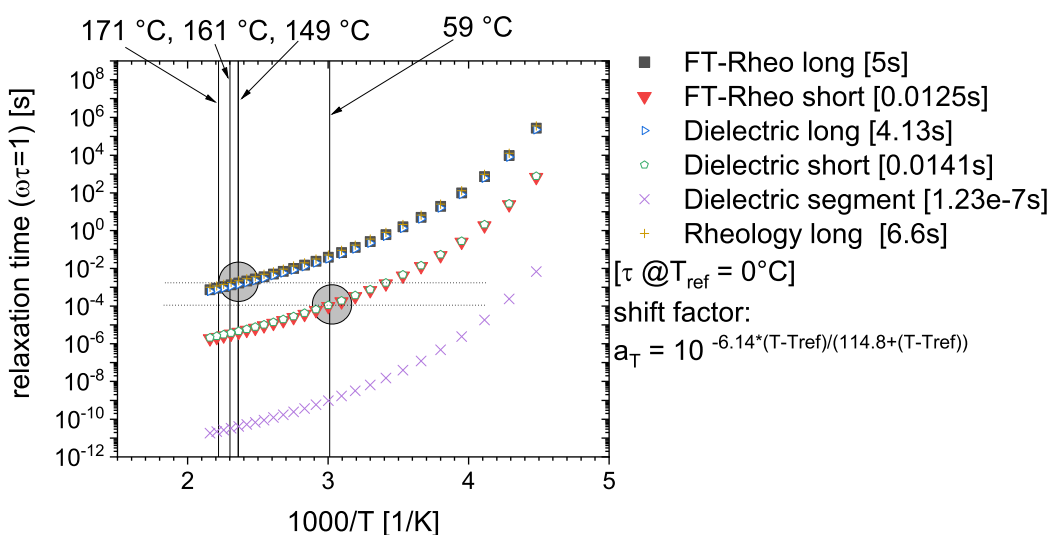

Figure 7.1. The temperature dependent relaxation times of different methods of different parts of the polymer comb PI-H68k-9-H14k are presented. Additional, the extrapolated temperature, for a fully isotropic relaxed polymer in TD-NMR are added as horizontal straight lines. The two methods connect at the respective temperature for an angular frequency of $\omega = 435\,\text{rad/s}$ for the bb and $\omega = 10\,000\,\text{rad/s}$ for the side arms, as marked with the gray circles.

8 Rheo-NMR used in polymerization kinetics - an in situ correlation of the mechanical modulus and the polymer concentration

This chapter deals with the simultaneous observation of mechanical properties and the T_1-weighted polymer concentration, which is a consequence of the segment dynamics of poly(acrylic acid) and the resulting correlation of the polymer concentration with the mechanical modulus. The previous chapters dealt with either the mechanical characterization of a specific sample or dynamic observations of the same sample, which was not done simultaneously. The herein presented method acquires both properties simultaneously, and consequently reduces timely uncertainties in the correlation. Before a general introduction is made, the setup and the procedure shall be explained. The chosen model system is the polymerization of acrylic acid with different degrees of crosslinking (DC).

This project complies with a publication that is in preparation between Christan Fengler and the author of this thesis.[110] The herein presented experiments and results were done by the author, the experimental results of the publication compared to this chapter are similar, but include additional fine-tuning of the experimental parameters. Consequently, the experimental results within this chapter build the base for the further and more precise experiments that are part the publication.

The polymer solutions and swollen networks that are employed within this project are a contrast to the PI-modelsystems. However, the acquisition of the concentration dependent modulus deals with comparable theoretical backgrounds to the dilution theory of bidisperse melts that was reported in section 4.2.2 *Fitting with the RDP-model*, p. 60.

8.1 The Rheo-NMR setup

Within this chapter the combination of a commercial rheometer and a custom-made low field NMR setup was used to characterize the polymerization of polymer hydrogels. A scheme presents this setup in Figure 8.1. As a rheometer a Discovery HR 3 (TA-Instruments), which is a stress-controlled rheometer, was chosen. The NMR magnet is based on an Hallbach array of NdFeB permanent magnets, which are heated to 40 °C for a stable field of $B_0 = 0.6$ T [$\omega_L/(2\pi) = 25$ MHz]. The probe is separated to the magnet by a partially silver layered Dewar to avoid heat transfer between the sample and the magnets. The probe has a dead time of ≈ 10 μs, a 90° pulse length of 2.2 μs and a 180° pulse length of 4.4 μs. The probe has an internal diameter of about 15 mm, which allows for geometries of 14 mm. The inside of the probe is temperature controlled with a Bruker VTU, in this project to 35 °C with an air (N$_2$) flux

of 270 L/h. The custom-made probe is connected to a commercial preamplifier and amplifier, which is connected to a computer with the MiniSpec© (all 3 from Bruker). For further details the reader is referred to literature, which includes technical drawings[111].
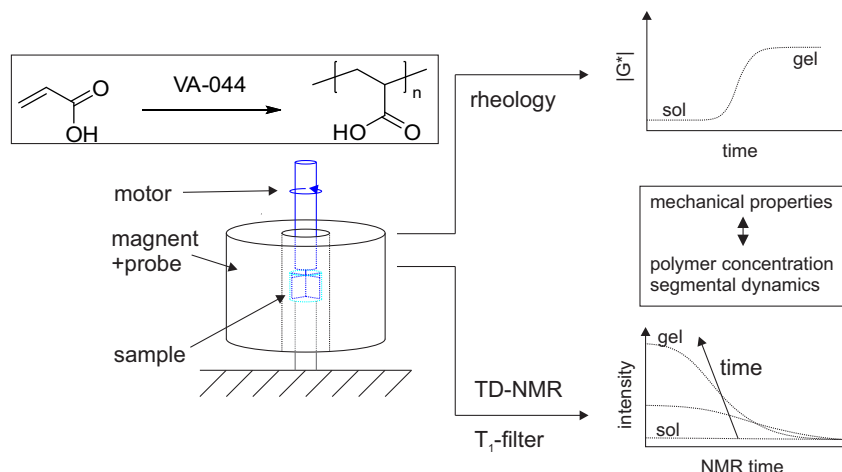

Figure 8.1. Scheme for the experimental setup (Rheo-NMR). The rheometer is represented by a fixed plate, which is connected to the bottom part of the geometry, and a rotatable upper geometry. The bottom geometry is a cup and can hold the sample, the top geometry is a vane-geometry with 4 fans. Around the geometries the probe and the magnet is placed. The rheology gives access to the mechanical modulus. The NMR setup gives access to segmental dynamics on a low nanometer scale and a T_1-weighted concentration. In this way, for the polymerization (with the thermal activated initiator VA-044) of acrylic acid, the mechanical modulus can be correlated with the concentration of the selfsame sample. All drawings and graphs are sketches. The volume of the geometry is about 1 mL. For drawing of the geometries, refer to the appendix 11.3 *Rheology/RheoNMR*, pp. 120 ff.

The special combination of mechanical testing and NMR requires special geometries, which fit the prerequisites for rheology (mechanical strength) and NMR (proton-free, non-conductive), moreover, the material has to be processed. Materials that fulfill these conditions are rare, they include glass, ceramics and perhalogenated polymers. Ceramics geometries have been employed in the studies of the vulcanization of rubbers[112] and the crystallization of polyolefins[113]. While polytetrafluoroethylene (PTFE) is commonly used in NMR, the material has poor mechanical properties, in particular a poor creep resistance. Similar to PTFE, polychlorotrifluoroethylene (PCTFE) is proton free as well and has sufficient mechanical properties. However, the thermal stability is limited, compared to ceramic geometries. Nevertheless, PCTFE was chosen as the material for the geometries within this project, since the used temperatures are well below its melting point and below its glass transition temperature[114]. Glass has been discarded, due to its limited processability and potential danger hazard. Ceramics are too brittle to be manufactured into the delicate structures of our geometries. Glass-fiber reinforced PTFE is a potential candidate for a suitable substance for geometries, however, due to the health hazard of broken glass fibers, this approach was omitted.

A bob-vane structure was used as a geometry design. It allows for a high sample volume ($\approx$ 1 mL), which is advantageous for NMR and it prevents spilling of low viscous samples due to its cup structure. Moreover, the surface exposed to air is small.

8.2 Synthetic parameters

The polymerization of acrylic acid and its kinetics were studied elaborately in the literature[115–118]. However, to the best of the author's knowledge, no other group was able to investigate polymerization kinetics while observing the mechanical properties and the concentration of the polymer/hydrogel formation simultaneously.

In this work, the radical polymerization of acrylic acid was investigated in solution (20 wt% in D_2O) with different degrees of cross-linking (DC) with *N,N'*-methylenebis(acrylamide) (0 % to 1 %, written as DC0 - DC1.0)[1] and a thermal initiator for aqueous systems for low temperatures (VA-044, fixed at 0.5 wt% is respect to the monomer). For the reaction scheme and the chemical structures of the reactants, refer to Figure 8.3 and Figure 8.2. In the presented results the AAc was not neutralized and therefore, the resulting hydrogel does not contain any cations except for H^+/D^+.

VA-044

***N,N'*-methylenbis-(acrylamid)**
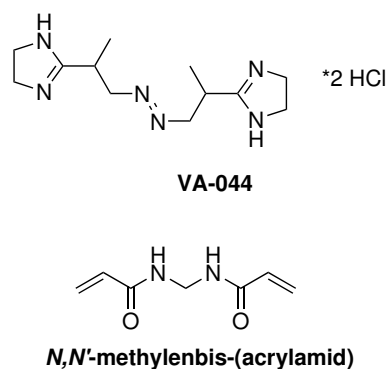
Figure 8.2. Chemical structures of the initiator VA-044 and the cross-linker *N,N'*-methylenebis(acrylamide).
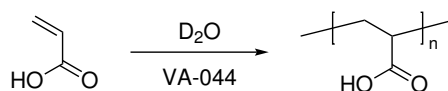

Figure 8.3. Polymerization of acrylic acid to poly(acrylic acid). D_2O was used as a solvent that is invisible in ^{1}H NMR experiments. The monomer concentration was 20 wt%. The hydrogen of the carboxylic acid is constantly exchanging with the (heavy) water and consequently, mostly a deuteron.

The resulting polymeric structures are observed well above the glass transition temperature and either networks or well entangled swollen polymer melts.

8.3 Time domain NMR measurements

The polymer melt dynamics during polymerization are observed by ^{1}H NMR T_2 relaxometry, *via* employing a combined MSE-CPMG/XY16 pulse sequences, which is presented in Figure 8.4. This type of experiment allows for the monitoring of the T_2 relaxation rates of all protons weighted by their T_1 rate.

---

[1]The degree of cross-linking is defined as the mol percentage of the cross-linker in relation to the monomer.

As introduced in 2.5 *Nuclear magnetic resonance (NMR) spectroscopy and relaxometry* (p. 29) both rates are dependent on the correlation time between two protons.

Longitudinal relaxation times

The relevant structures show a big contrast in T_1, which allows a precise classification into small molecules and polymeric structures (refer to Table 8.1). The experiments to obtain the T_1 distribution have been done after the polymerization process.

Table 8.1. ^{1}H NMR T_1 results at $T = 35\,°C$. Table with proton containing molecules, their respective assignment and T_1 time. The reported values are obtained from a PAAc DC0.3, however, the values do not significantlly change with different degree of cross-linker. Herein this thesis, only non-neutralized hydrogels are investigated. The values are obtained after the polymerization, consequently, any free oxygen was chemically removed before the gelation. The T_1 is expected to be less directly after mixing the reactants, since the sample was not degassed and residual oxygen is paramagnetic.

type		T_1 [s]	assignment
solvent:	HDO	≈ 3	sol
monomer: AAc & *N,N'*-methylenebis(acrylamide)		≈ 3	sol
hydrogel:	PAAc	0.03-0.1	network

The recycle delay was chosen to be $rd = 300\,\text{ms}$, which is much higher than the relaxation time of the network and much less than the relaxation time of the sol. Therefore, the network is relaxed to $> 99\,\%$, while the sol is relaxed to 10 % of the maximal possible intensity.[2] The experimental results of a saturation recovery experiment which has been employed to get the T_1 times are visualized in Figure 8.5. The experimental results are fitted with a bi-exponental build-up curve (refer to Equation 8.1)

$$I_{SR} = A_{gel}[1 - \exp(-\tau/T_{1,gel})] + A_{sol}[1 - \exp(-\tau/T_{1,sol})] \tag{8.1}$$

The resulting ratios of A_{poly} and A_{sol}, equal to the fraction of polymers and sol. Typical normalized values are $A_{poly,n} = 70\,\%$ to $75\,\%$ and $A_{sol,n} = 30\,\%$ to $25\,\%$. Since the plateau of the sol is not reached, and it would take significant additional time to obtain bigger τ's, $A_{sol,n}$ has a significant uncertainly and the coefficients typically add up to > 1. However, this error has no direct consequences for the further measurements.

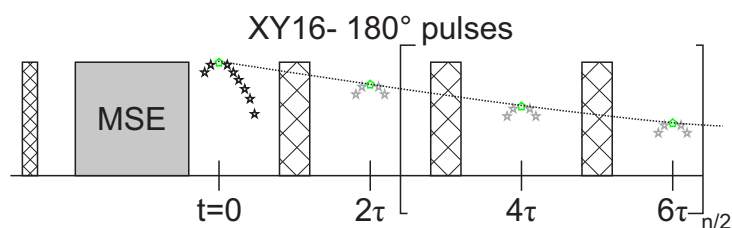[2]$[1 - \exp(-rd/T_1)] \approx 10\,\%$

Figure 8.4. The MSE(magic sandwich echo)-CPMG/XY16 pulse sequence. After an initial 90° excitation pulse, the magic sandwich echo sequence allows to refocus all magnetization avoiding the dead time, which results in an echo which is set arbitrarily to $t = 0$. Thereafter, a train of 180° pulses is applied with alternating phases. Hereby, the echoes between the pulses are recorded and saved as an intensity/time pair. Due to the phase cycling and spinlock effects as observed in the original CPMG sequence are avoided.
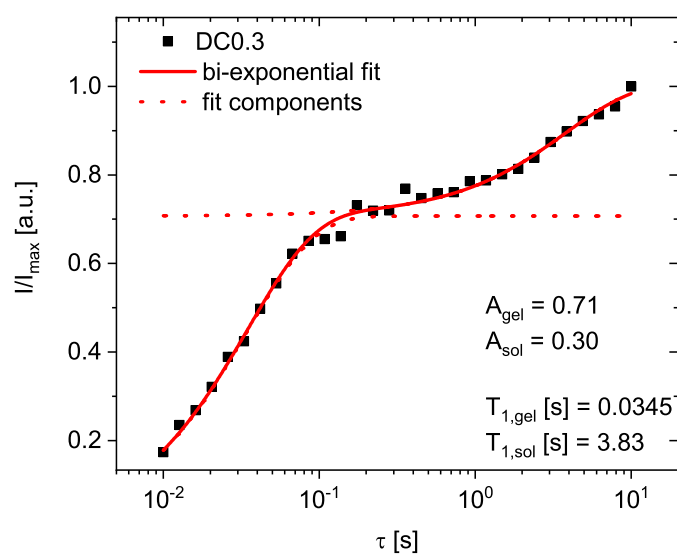
Figure 8.5. ^{1}H T_1 saturation recovery experiment of a poly(acrylic acid) DC0.3 and a polymer concentration of 20 wt%. The experimental results are modeled with the bi-exponential build-up curve Equation 8.1, giving access to the relaxation times of both the polymer network and the sol. Additionally, the respective summands of the bi-exponential fit are presented. The experiment is recorded after the polymerization kinetics. The summands add up to slightly > 1, since the system is not in full equilibrium after 10 s.

Transversal relaxation times T_2

The polymerization kinetics of poly(acrylic acid) were recorded with the MSE/XY16 experiments in time sweeps. The characterization of hydrogels in commercial relaxometers and relaxomtery, in general, as a universal non-invasive tool has been studied excessively.[119–124] However, these types of experiments typically focus on a sufficient signal intensity and have very long time spans available. The geometry was chosen to maximize the sample volume to 1 mL. Several points have to be considered and optimized, to have a sufficient signal-to-noise in the time sweeps of the NMR experiments.

- After the inhibition[3] period, polymerization finishes in about 500 s.

  A repetition time of less 10 s is desirable in order to have about 50 datapoints.

  A single NMR scan, including rd, pulse times and data processing, takes about 1 s.

- A very broad range of T_2 relaxation rates is expected, from about 1 ms to several seconds.

  To monitor the fast decays, the acquisition rate[4] is desired to be less than 100 μs in order to resolve fast T_2 decays well.

  The distance between two 180°-pulses, cannot be altered in mid-sequence, without having substantial systematic errors in the following echoes.

  The NMR probe requires significant power (> 100 W) during the pulses, which heats the probe. And the heat has to be dissipated with the air flow from the temperature control unit. Consequently the amount of 180°-pulses per time is limited to about less than 1000 pulses per second, which relates to heating of about 6 K.[5]

All things considered, the desirable parameters seem to contradict each other. After the first experiments, to following settings were chosen, which optimized all the bottlenecks.

- two scans with 128 echoes per decay

- five experiments with different acquisition rates are merged

  The shortest time between pulse and echo (τ_{CPMG}), which is a setting parameter, is $\tau_{CPMG} = 20$ μs. The resulting acquisition rate is about double (37 μs). For every subsequent experiment τ_{CPMG} is tripled. The longest time in the NMR experiment is consequently 414 ms

- one non-acquired dummy-scan is added, to avoid unexpected echoes from different acquisition rate experiment

---

[3]The inhibition period is discussed later in Figure 8.7, p. 104.

[4]The acquisition rate is herein this chapter defined as the time between two data-points in the CPMG/XY16-train. The term dwell time is avoided, since the dwell time is the rate of aquisition in the FID, which is many decades faster.

[5]A pulse length is 5 μs, consequently with a pulse rate of 1000 Hz the occupancy rate (duty cycle) is 5/1000. Assuming a maximum power of 100 W, the average power output is 0.5 W. The air flow is about 270 L/h = 0.075 L/s and by assuming a heat capacity of about 1.2 kJ/(m^3 K), the resulting heating of the air flow is about +6 K.

Together, a time sweep point can be acquired every $\approx 14\,$s. The resulting relaxation can be evaluated in different ways, such as fitting with different models, including a stretched bi-exponetial fit, a stretched exponential fit with offset, or a Laplace transformation. As the data is very noisy, especially at times before gelation, the parameters of the fits have to be restricted, to avoid meaningless outliers.

The best fitting results have been achieved by combining 3 of the 5 experiments with different acquisition rates and the function presented in Equation 8.2.

$$I(t) = A_{gel} \exp(-t/T_{2,gel})^{0.7} + A_{sol} \exp(-t/T_{2,sol}) \tag{8.2}$$

Hereby, the parameter A_{gel} represents an uncorrected relative polymer concentration. Minor correction are done afterwards to obtain the concentration that explained later on. In Figure 8.6 **a)** the transversal decay of a fully cured PAAc hydrogel (DC0.3) and the respective fit is presented. The stretching parameter (β) was chosen as $\beta = 0.7$, since it shows in average the best agreement throughout different degrees of cross-linking. This implies that the herein presented hydrogels are more inhomogeneous compared to synthetic rubbers that have higher values for β For liquids, no stretching is expected $\beta = 1$, while for defined polymer melts or networks a compression is observed. In the case of glasses or crystals, a Gaussian behavior is observed ($\beta = 2$) and for rubbers Weibull-type functions, resulting in a value β in between.[112, 125–128] The fitting can be run automatically, which removes a bottleneck in the
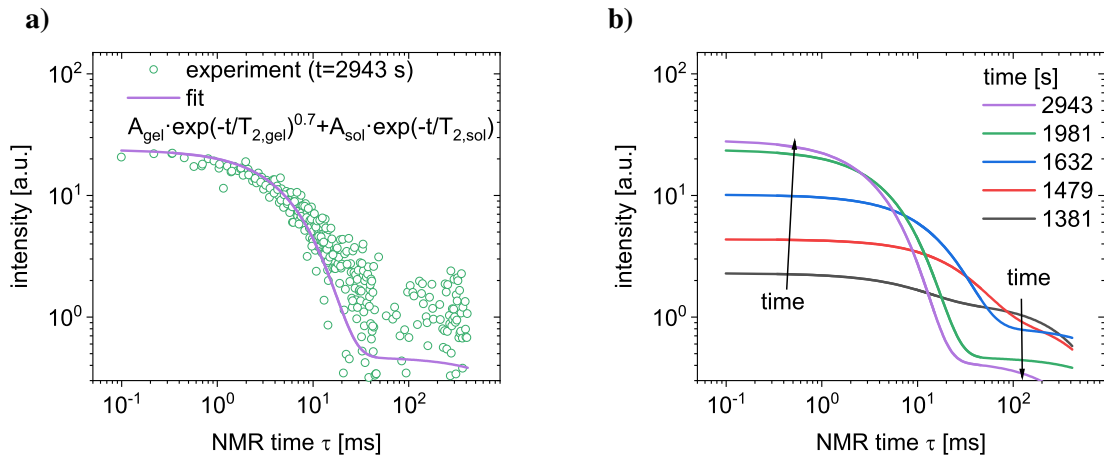

Figure 8.6. Relaxometry measurement of poly(acylic acid) hydrogels ($c = 20\,$wt%, DC = 0.3 mol%) during gelation and their respective fits. In **a)** the transversal decay of a fully cured hydogel is presented with the fit of Equation 8.2. The NMR data is very noisy, however, all the data was acquired in 14 s. **b)** presents the transversal decay at different time steps for the gelation process. After along (1381 s) period of inhibition, the polymerization converses within $\approx 500\,$s. Thereby, several trends can be followed. Firstly, the total intensity increases with progressing polymerization. Secondly, the sol content decreases with progressing polymerization. Thirdly, the transverse relaxation time decreases with increasing conversion

data-evaluation. The collected fitting parameters can be presented as a function of time. The focus in this work, is on the fraction of the gel, since it is proportional to the polymer concentration, while the sol is suppressed with the T_1-filter. In Figure 8.7 the gel-fraction parameter A_{gel} is presented as a function of time. The parameter A_{gel} itself is proportional to the polymer concentration. To receive the exact polymer

concentration, it has to be devided by the plateau value of A_{gel} or the gel-fraction of the non-normalized T_1 measurement (refer to Equation 8.1)
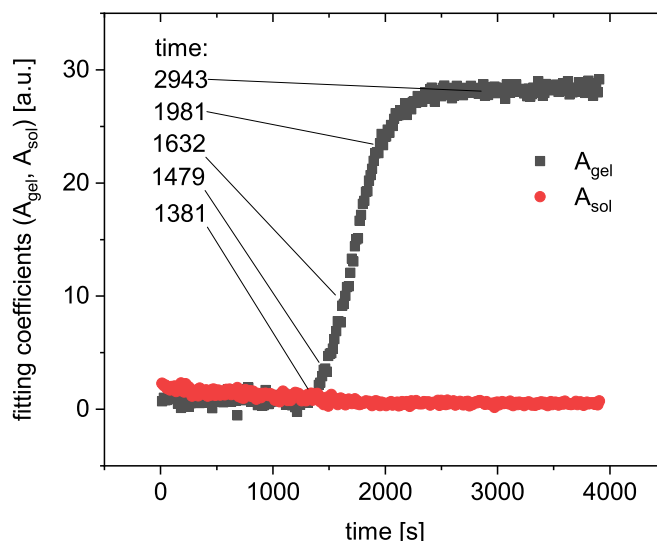

Figure 8.7. Polymerization kinetics of PAAc DC0.3. The fitting parameters of Equation 8.2, are plotted against the time. Selected times have been marked as a reference to Figure 8.6. The polymerization has a long inhibition period of about 1381 s. The parameter A_{gel} starts with a plateau close to zero, then has an S shaped growth, which finally results in a plateau. The A_{sol} parameter remains almost constant at a relatively low level. However, a steady drop in magnitude until the end of the inhibition period is observed, which is most likely due to a change of the T_1 time, since the radicals of the initiator consume the paramagnetic oxygen.

Signal-to-noise

The signal-to-noise ratio is important in any experiment, since it characterizes the reliability of the presented data. While the term noise is often used, the term uncertainty is more precise. Two types of uncertainties are differentiated, the systematic uncertainty, which is the same for every experiment, and the statistical uncertainty, which scales with the square root of the experiments.
Systematic uncertainties can occur due to constant offsets in the experimental setup, or by applying models that cannot describe the data in its entirety. The quantity of the systematic uncertainty is not dependent on the number of experiments. In contrast to that, statistical uncertainties originate from randomized events, such as thermal fluctuations. The statistical uncertainties can be averaged by multiple experiments and scale with the square root of the number of experiments.[6]
To quantify the uncertainty in the presented results, experiments with different number of scans have been compared. The sample was a PAAc DC0.3, after gelation. The NMR experiments a MSE/XY16 pulse train, with 128 echoes and a distance between pulses of $2 \cdot 20\,\mu s$ was employed. All transverse relaxations were fitted with a stretched exponential, by using the software OriginPro2019b. The coefficient of the

---

[6]Consequently, the S/N -ratio scales with one over the square root of experiments.

exponential function, which is the y-axis intercept, was taken as the signal S and the uncertainty of this coefficient was taken as the noise/uncertainty of the fits.
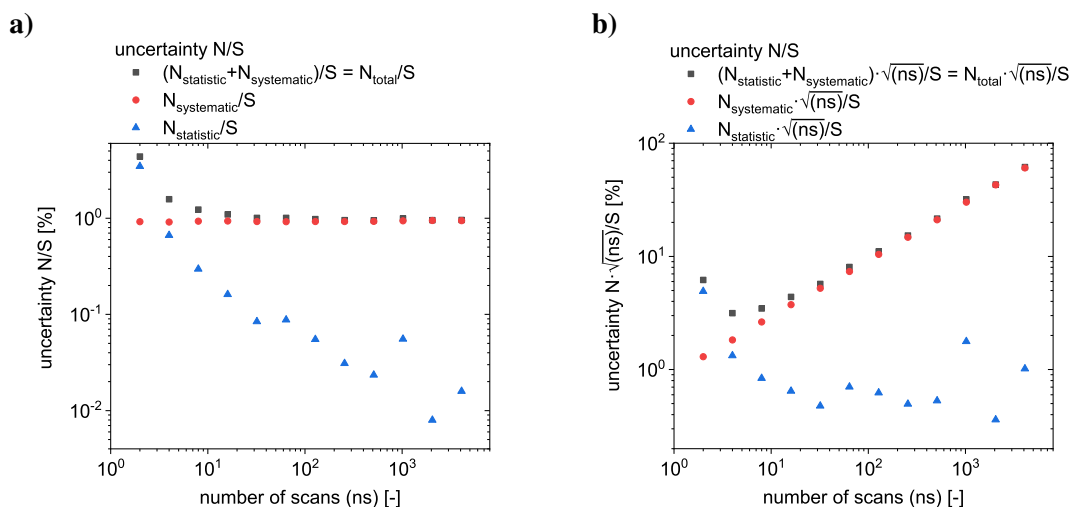
Figure 8.8. a) The noise level N/S is the transverse relaxation time measurements, as a function of number of scans. The total noise shows a plateau at about 1 %. This plateau-value is taken as the systematic uncertainty, since it is independent from the number of scans for high number of scans. Consequently, the statistical uncertainty is the difference of the total uncertainty and the systematic uncertainty. **b)** The noise level N/S·$\sqrt{\text{number of scans}}$, as a function of number of scans. The total uncertainty shows a minimum between 4 and 8 scans. The systematic uncertainty shows power law behavior with the expected slope of 0.5. And the statistic contribution shows a plateau at N/S·$\sqrt{\text{number of scans}}$ = 0.62 %, which is an intrinsic property of the measurement conditions.

In Figure 8.8 the inverse of the S/N ratio is presented. The systematic uncertainty is in the range of 1 % independent from the number of scans. Furthermore, the statistical uncertainty is 3.5 %, 0.66 % and 0.30 % for 2, 4 and 8 scans respectively. The N/S·$\sqrt{\text{number of scans}}$ shows a minimum between 4 and 8 scans, making it the optimum between time resolution and precision. However, as elaborated in the section 8.3 *Transversal relaxation times* T_2, p. 102, the measurement might have to be done at lower scan repetition numbers to enhance the time resolution. Nevertheless, the uncertainty for the worst case is of two scans is 4.4 %, consequently the S/N in this case has a value of 23, which is well above the limit of quantification with a value of 10.[129]

8.4 Mechanical properties during polymerization

During the polymerization of PAAc in solution, the mechanical properties were monitored. Moreover, the transverse relaxation was monitored simultaneously and was discussed in the previous section 8.3 *Time domain NMR measurements* (p. 99). The rheological geometry is a bob-vane geometry[7] in a stress-controlled rheometer (for more detail see 8.1 *The Rheo-NMR setup*, p. 97, and for drawing of the geometries, refer to the appendix 11.3 *Rheology/RheoNMR*, pp. 120 ff.). The change in mechanical properties is presented in Figure 8.9. In the beginning a plateau is observed, which is dominated by the inertia of the geometry. This observation was proven by monitoring a phase angle of 180°, which is equivalent to the second derivative of the excitation. The true start of the polymerization is indicated by a sharp increase in mechanical modulus, which levels to a plateau of 28 kPa (for PAAc DC0.3) after approx. 500 s. The used rheometer is stress controlled, and as the limit for the linear regime a stress of $\sigma = 1000$ Pa was found. To stay within the linear regime during the polymerization and to reduce the maximum amplitude a stress of $\sigma = 10$ Pa was chosen as experimental parameter.
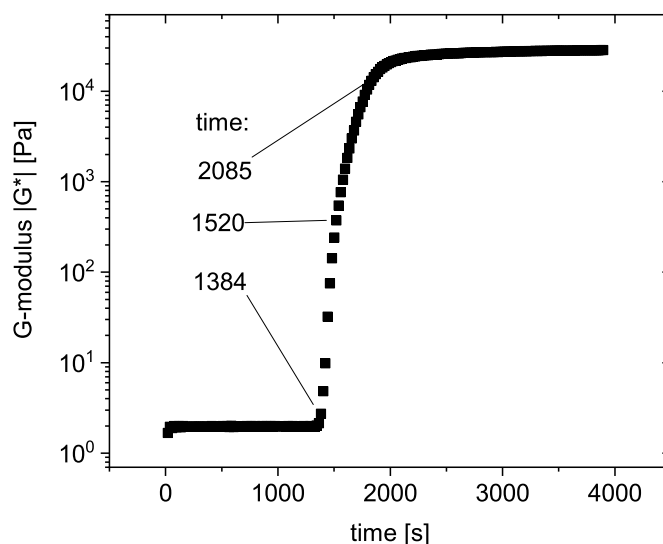
Figure 8.9. Polymerization kinetics of PAAc as determined *via* $|G^*(t)|$ of PAAc DC0.3 (20 wt%) at 35 °C. In rheology was obtained in the stress controlled mode at $\sigma = 10$ Pa and $\omega = 1$ rad/s. The mechanical shear modulus is presented as a function of time. The modulus starts from a plateau, until the end of the inhibition of about 1840 s. The modulus grows in a S-shape, until it reaches a plateau of 28 kPa.

---

[7]A plate-plate geometry has been discard, since the used geometry has a much higher sample volume (0.13 mL *versus* 1 mL). Moreover, the relative surface is bigger of a plate-plate geometry, which would increases drying-out effects.

8.4.1 Comparing relative concentration parameter A_{gel} and mechanical properties

By comparing the mechanical properties in Figure 8.9 and the relative concentration, obtained from TD-NMR, in Figure 8.7, the timely trends of the mechanical properties and the concentration appear to be very similar. To quantify a correlation, the time dependent parameters have to be put on the same time scale. Therefore, the all data within the interval of 60 s are reduced to a single value by building the median value. In Figure 8.10 the comparison and the correlation are presented. The correlation **b)** is split in two parts: The first one, in the gray area, are values during the inhibition period, where the expected polymer concentration is zero. Therefore, these points are dominated by systematic errors, which relate to the moment of inertia in G^* and an apparent solid fraction in the transversal relaxation, due to strong noise, respectively. The second part, corresponds to the desired correlation.
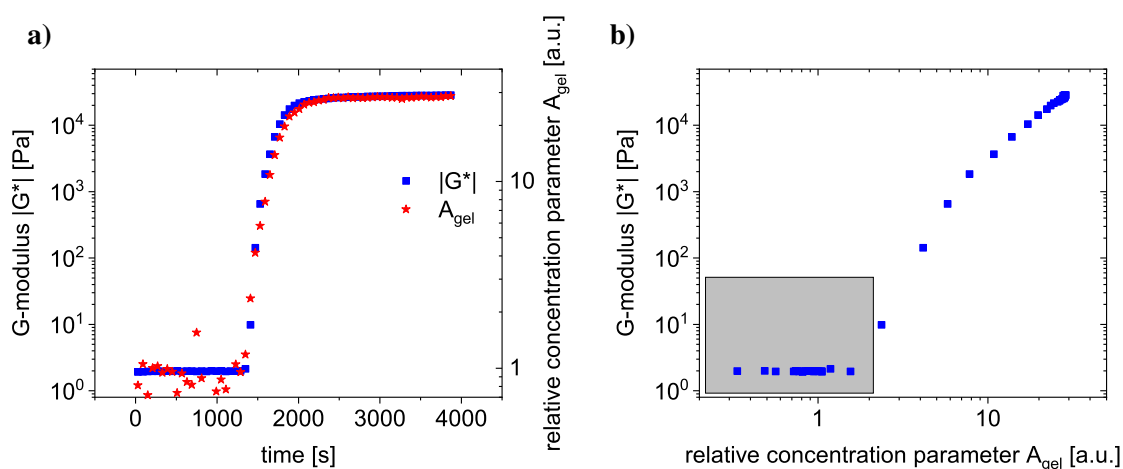
Figure 8.10. In **a)** the comparison of $|G^*|$ (obtained by rheology) and the concentration parameter A_{gel} (obtained by TD-NMR) is presented. The time axis was reduced to 60 s steps by building the median of all values within this step. The same data is presented in **b)** as a correlation without any corrections. Marked in the gray area, are experiments while the inhibition period. The remaining experimental data points show a power law behavior.

Within the correlation the time component is avoided. Polymerization kinetics are very sensitive towards, small changes to i.e., temperature, concentration or the degree of degassing. Moreover, the gel-effect, which reduces the termination reaction in free radical polymerization, make kinetics more challenging to model. Since in the correlation, the time component is not present, all these consideration are not affecting the final results, which is highly increasing the reproducibility.

All rheological data below 3 Pa and the corresponding TD-NMR data were omitted, since it is the threshold the systematic error of the employed rheometer, and then continued with the evaluation of the correlation.

8.4.2 Correlation of concentration and mechanical properties

The final goal is the quantification of the correlation of the mechanical modulus and to the polymer concentration c. The parameter A_{gel} is normalized, consequently, the maximum of $A_{gel}/A_{gel,max}$ corresponds to the maximum polymer concentration c_{max}, which is $20\,\mathrm{wt}\%$, and therefore, the current concentration c is accessible a presented in Equation 8.3.

$$A_{gel}/A_{gel,max} = c/c_{max} \tag{8.3}$$

The correlations of samples with different DC are presented in Figure 8.11, fitted using Equation 8.4 and these results presented in Table 8.2, moreover, the modulus as a function of DC is presented in Figure 8.12. The modulus $|G^*_{max}|$ is increasing with DC and is modeled with a linear fit. For higher DC the fit overestimates the true modulus, which is likely due to a reduced crosslinking efficient at high DC. To account for uncertainties regarding the concentration and the modulus, an orthogonal regression has been chosen and weighted 'statistically'(which means the weight is inverse to the absolute value). The orthogonal regression is chosen, since both dimensions show uncertainties and the weighting is selected, since it is assumed that the uncertainty is relative to the respective value.
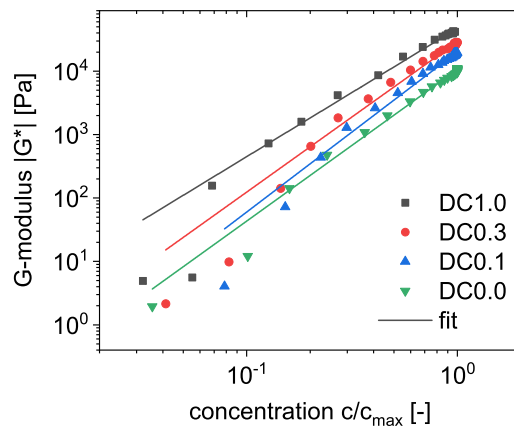
Figure 8.11. Correlation of G-modulus and concentration with different DC. All samples show similar trends. The raw data is fitted with Equation 8.4.

$$|G^*| = |G^*_{max}| \cdot [c/c_{max}]^n \tag{8.4}$$

To summarize, the mechanical properties and the transverse relaxation of PAAc during gelation was monitored during polymerization at the same time. In polymerization kinetics many effects influence the results, which reduce the predictability of the polymerization process. Hereby, small deviations, *e.g.,* in temperature or oxygen content, leads to different results. To avoid the time component, the G-modulus, which was obtained in the rheometer, has been directly correlated with the concentration,

Table 8.2. Fit results of the correlation of the mechanical G-modulus and the concentration. By employing Equation 8.4, the modulus as a function of DC is graphically presented in Figure 8.12.

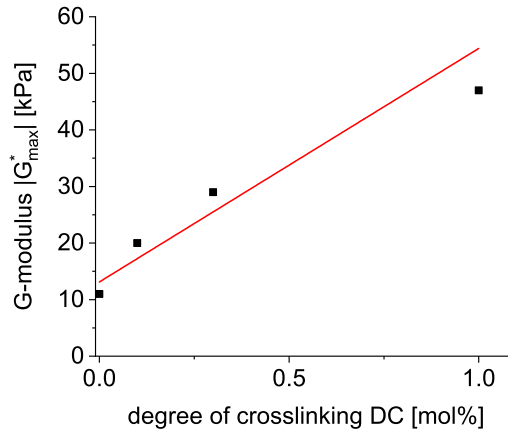| DC [mol%]	$|G^*_{max}|$ [kPa]	n
0.0	11	2.4
0.1	20	2.5
0.3	29	2.4
1.0	47	2.0

Figure 8.12. The fitted plateau modulus $|G^*_{max}|$ as a function of DC of 20 wt% PAAc in water. The modulus is fitted with a linear function $|G^*_{max}| = a + DC \cdot b$, with $a = 13.1$ kPa and $b = 41.3$ kPa/%.

which is obtained by the T_1-filtered transverse relaxation time. The scaling exponent in respect to the concentration is in the range of $2 - 2.5$. The herein presented results show uncertainties, as observed in Figure 8.11. The scaling laws (refer to Table 8.2) are in the same range as in literature $n = 2.25$ [130], $n = \{7/3, 2.31, 3/2\}$ (for polymers in θ-solvents, polymers in good solvents or polyelectrolytes, respectively) [131] and $n = \{2, 7/3\}$ (depending on the assumed dilution coefficient) [26]. However, the data quality and point density is improvable for $c/c_{max} < 10\%$.

Outlook

The correlation parameters as listed in Table 8.2, show uncertainties. By optimizing the experimental conditions, the time resolution and the precision of the NMR-results can enhanced. Following further considerations can be made: The relaxation time of the sol is of no importance, therefore, the sol does not have be recorded in the NMR experiments. Consequently, the dynamic range that the NMR experiments have to cover, can be condensed into a single XY16 train, which avoids the hassle with merging XY16 trains with different τ. Moreover, repeating the very same experiment does not require dummy shots, which increases the duty time even more. By reducing the used time by the previous mentioned suggestions, the number of scans can be increased to the optimum of 4 or 8 scans averaging per experiment, while retaining the high time resolution.

9 Conclusion

Within the presented thesis, polymer model systems were synthesized by living anionic polymerization and characterized.

Linear bidisperse polyisoprene (PI) melts were characterized in oscillatory shear rheology in the linear and non-linear regime. Hereby, the linear viscoelasticity was modeled using the Rolie-Double-Poly model to acquire the terminal relaxation relaxation time of respective components. Moreover, a semi-empiric model[1] for the intrinsic non-linearity for monodisperse samples was extended to fit bidisperse homopolymer melts. The required parameters are all obtainable from different methods, including the volume fraction and molecular weight, which is accessible by SEC. Moreover, the relaxation times are determined by the modeling of the LVE. Consequently, a semi-empiric model was presented that predicts the non-linear viscoelasticity of bidisperse homopolymer melts with only external acquirable parameters. In addition to that, the model for the intrinsic non-linearity of the bidisperse melts was applied to polymer combs. The non-linear experiments show good agreement with the prediction for the bidisperse systems, by assuming that the backbone is the longer component and the side arms are the shorter component of a bidisperse system. Hereby, the volume ratio is the backbone/side arm ratio. The relaxation time of the backbone can be acquired in a straight-forwardly manner from the linear viscoelasticity. However, the relaxation time of the side arms was not modeled and therefore taken as a free fitting parameter.

As an outlook, the non-linear rheology of ring polymers (with small fractions of linear polymers) were compared to linear polymers. As a result, a good agreement was found in the rubber regime, nevertheless, the flow regime has a different scaling law in the intrinsic non-linearity.

The FT-rheology of self-synthezied samples was acquired and successfully modeled allowing the prediction of the non-linear rheology of linear bidisperse melts and comb polymer melts.

Deuteron labeled isoprene was synthezied and employed in the anionic polymerization of partially deuterated polyisoprene model systems, including linear 'triblock'-co-polymers and comb polymers. The model system were characterized in proton TD-NMR. Additionally, the partially deuterated comb was characterized in deuteron TD-NMR. The comb has proton labeled side arms and a deuteron labeled backbone, allowing for the observation of the chain dynamic of the respective parts. The isotropic relaxed fraction in a wide temperature range was characterized and extrapolated to the temperature of full isotropic relaxation. This temperature was compared to the temperature dependent relaxation time obtained by different methods, including the linear rheology, FT-rheology and broadband dielectric spectroscopy. The temperature of fully isotropic relaxation from the TD-NMR and the temperature dependent relaxation time from the mechanical/electrical analysis show a transition show a crossover at frequency values of

$\omega/(2\pi) = 69\,\mathrm{Hz}$ for the and $\omega/(2\pi) = 1600\,\mathrm{Hz}$ for the side chains.

Furthermore, the broadband dielectric spectroscopy (BDS) properties of polyisoprene combs have been characterized in a broad temperature and frequency range. For a model system PI comb, two normal modes were found and assigned to the backbone and side arm relaxation respectively. The two normal modes, obtained by BDS, are in good agreement with the results from rheology and FT-rheology.

In the novel Rheo-NMR setup the gelation kinetics of hydrogel polymerization with polyacrylic acid was characterized in rheometry and TD-NMR simultaneously. The hyphenated technique allows for the correlation of the mechanical properties with molecular dynamic properties. Hereby, the T_1-weighted proton concentration was used to calculate the current polymer concentration in the sample. Consequently, the correlation c of the polymer concentration with the G-modulus ($|G^*|$) at a fixed frequency was obtained. In the direct correlation of c/c_{max} *vs.* $|G^*|$ a power law was found, where the coefficient is the maximum modulus and the exponent scales at about 2.0 to 2.5, which is in good agreement with the standard models in literature, which predicts a value between 2 and $7/3$.

10 Outlook

In this work, the modeling of linear shear rheology allowed for the prediction of the non-linear properties in linear bidisperse systems and partially in polymer combs. By further investigating polymer melts with defined topologies, the range of architectures for that the intrinsic non-linearity $^3Q_0(\omega)$ can be predicted from linear rheology will be increased. These promising architectures include especially pom-poms, since the pom-pom model is well-established.

The synthesis of a pom-pom using a facile synthesis and first oscillatory shear rheology results were shown. The synthesis of pom-poms with different dimensions, their shear rheological and elongational characterization remains to be performed. Moreover, the comparison to the theoretical predictions is of interest. This is important, because the scientific community in severe lack of characterized pom-poms and with the presented method, the range of characterized systems can will increased by a large margin.

First measurements on partially deuteron labeled polymer samples were investigated. Therefore, the range of investigated samples can be increased, including different structures like pom-poms. Moreover, a more localized labeling (*e.g*, the crosslinker section of a polymer comb), combined, with a broad sample range, would allow for the in-depth characterization of a specified system. The double quantum results, or more precisely the derived segmental orientation autocorrelation function is facile parameter in molecular dynamic simulations. In consequence, the comparison of the NMR results with molecular dynamic simulation is of interest.

The investigation of polymer melts, especially PI, combined with the monitoring of either time domain NMR or broadband dielectric spectroscopy (BDS) in the same setup poses a challenge. The orientation of PI-polymer chains should be observable in both techniques. First tests were performed, but the results were not quantifiable due to limitations in the setup. In the case of BDS, an applied strain to a non-relaxed system should orient the end-to-end vector towards the x, y-plane, and consequently a reduced the dielectric constant should be observed. Hereby a way has to be found to keep the PI between the electrodes, since polymer melts under strain tend to be forced out of the restriction. The dipolar coupling in NMR is dependent on the angle between the external magnetic field and the vector between the observed nuclei, consequently an orientation of the segments under strain, leads to a difference in the dipolar interaction.

By using the Rheo-NMR, a hyphenated technique of oscillatory shear rheology and TD-NMR, was used to show the correlation of concentration *versus* the mechanical modulus for the polymerization of acrylic

acid by employing a T_1 filter. A broader range of monomers at different solvent qualities should be further investigated, ranging from θ-solvents to polyelectrolytes in water.

An interesting field could be the polymerization of styrene in solvents of different quality, such as (*iso-*)alkanes as θ-solvents, towards more polar solvents like toluene, very good solvents like THF, towards very polar solvents such as alcohols. By doing so the power law exponent of the G-modulus *versus* the concentration as a function of polarity or solvent quality can be obtained and compared to existing predictions in literature. The challenges hereby are to find an initiator that is soluble in all solvents and that decays at an as low temperature as possible, next to finding solvents that evaporate slowly.

In this work, non-charged hydrogels were investigated, consequently, the variation of the degree of neutralization is a promising topic. By having a partially charged polymer, the polymerization is essentially a co-polymerization between the charged and uncharged species, which increases the complexity in terms of polymerization kinetics.

The Rheo-NMR correlation was conducted for a free radical polymerization. As a similar, yet different topic controlled radical polymerizations are of interest, since the chain concentration is constant and slowly growing (while during the free radical polymerization the molecular weight and dispersity is almost constant throughout the polymerization and the number of chains is growing). In this system, while measuring the polymer concentration, the molecular weight would be indirectly be measured. However, since controlled radical polymerization typically lead to smaller molecular weights, the contrast in T_1 would most likely change throughout the entire polymerization process. Anionic polymerization, as the standard for monodisperse high molecular weight polymerization, is basically impossible in the used equipment, but the controlled radical polymerization might be a sufficient substitute.

The free radical polymerization is a chain growth polymerization. In contrast to that, a step growth polymerization such as a polyaddition is worth investigating. Hereby one has to consider, that the principle of least constraint to remove a condensate is not applicable, which basically rules out polycondensations. In the polyaddition polymerization the mass of oligomer/polymer is constant, but the polymer chain get increasingly restricted with the degree of polymerization. Consequently, the correlation of the mechanical module $|G^*|$ with the transverse relaxation time T_2 is promising.

11 Appendix

11.1 Further characterizations

11.1.1 Thermal stability of polyisoprene

Polyisoprene (1,4-*cis*) and all other micro structures (refer to *Microstructues of polyisoprene*, p. 12) have unsaturated double bonds that are more reactive than saturated polymers, like polypropylene or stabilized double bonds, such as the phenyl rings in polystyrene. Most of the characterization methods used in this work require elevated temperatures to fully characterize the sample. During heating, the sample must not degrade. By *degradation* in this work the author refers to thermal cross-linking, depolymerization, chain fracture and unwanted chemical functionalization. Since the main topic of this work is the characterization of the dynamics of model systems, the model system are characterized in a wide temperature range. To avoid temperatures that destroy the model system a small study towards the thermal stability of polyisoprene was evaluated. All measurements where a thermal degradation can be relevant, were performed under either inert gas atmosphere or in vacuum.

Many studies of the stability of polyisoprene have been done and are well known in the literature.[132–135] However, the dominating method to measure the thermal stability is the thermogravimetric analysis (TGA), which observes the weight loss, but has no information about possible cross-linking or chain cleavage reactions. Even if TGA neglects these reactions, the literature agrees that above 200 °C a significant weight loss is observed, which relates to degradation. Consequently, changes of molecular weight are expected latest at this temperature.

To quantify the degradation on a molecular level, the change of the crossover frequency in a dynamic frequency sweep of a PI sample after different intensities of thermal exposure is monitored. As the sample of choice, a well entangled polyisoprene with a dispersity of $Đ = 1.3$, a molecular weight of $M_n = 250 \, \text{kg/mol}$ and 1 wt% of the stabilizer 2,6-di-*tert*-butyl-4-methylphenol (BHT) was chosen. The sample was subject to different curring conditions and was characterized in a frequency sweep in between. The curing time was 1 h at the given temperatures (no curing, 100 °C, 120 °C, 140 °C, 160 °C, 180 °C, 200 °C, 210 °C). The angular frequency at the terminal crossover point in the G-modulus was taken as a parameter that is very sensitive to changes in the molecular weight ($1/\omega_{crossover} \propto M^3$, refer to 2.4 *Dynamics and rheological properties of polymer melts* p. 25), thus being sensitive towards cross-linking and cleavage reactions.

In Figure 11.1 the frequency sweep of a test PI is presented, as well as, the $\tan(\delta)$ of the strain sweep after curing for 1 h at different temperatures. Since the differences in the mechanical properties are small, the frequency of the crossover point was chosen to be the reference parameter for a change in the molecular

weight. The change in crossover frequencies is visualized in Figure 11.2. Consequently, the material is stable until 180 °C for minimum an hour. To prevent thermal degradation in long term studies 150 °C was set as the maximum temperature for long time heat exposure. The herein presented method of tracking the degradation with the terminal relaxation time, has in contrast to TGA the advantage that it is sensitive towards changes in molecular weight and consequently the change of chain dynamics, which is the main focus of this thesis.
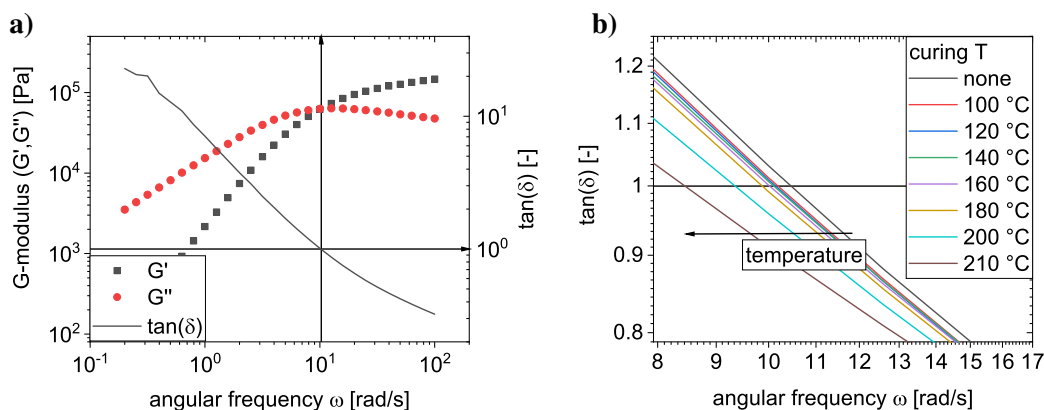
Figure 11.1. Oscillatory shear characterization of a PI that is stabilized with BHT, all measurements are done at $T = 120$ °C with an amplitude of $\gamma_0 = 1\%$. **a)** Dynamic frequency sweep of PI sample ($M_n = 250$ kg/mol, $Đ = 1.3$) after curing the sample at 100 °C for 1 h. **b)** Enlarged section of the crossover region ($\tan(\delta) = 1$) for the same PI sample, after curing consecutively at different temperatures for 1 h each time. After the first curing at 100 °C, where traces of solvent evaporated, the mechanical properties are stable until about 180 °C. The change in the crossover point are visualized in Figure 11.2. While the curing was done at different temperatures, all dynamic frequency sweep measurements were done at $T = 120$ °C.
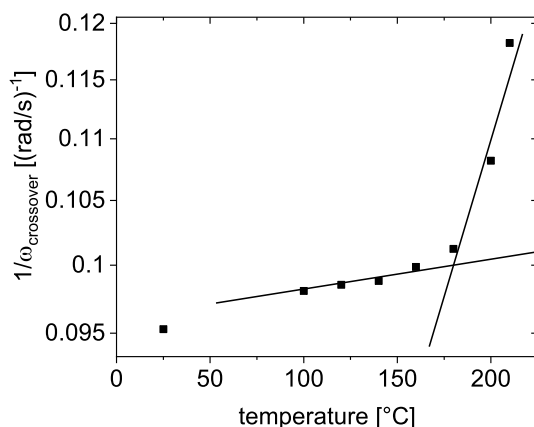
Figure 11.2. The change of the crossover frequency after different curing temperatures of the PI that is stabilized with BTH. The material is stable until 180 °C. The sample was cured for 1 h at the respective temperatures and then the crossover frequencies are measured at $T = 120$ °C.

115

11.1.2 Rheology on a pom-pom topology

Pom-poms are interesting systems, since its melt dynamics can be easily modeled with the pom-pom model. First rheological properties of the self synthesized pom-pom polymer were characterized. The synthezied sample has a backbone molecular weight of $M_{n,bb} = 360$ kg/mol and side chain molecular weight of $M_{n,sc} = 135$ kg/mol. The pom's have 21 side arms on each side as calculated from the total molecular weight of the pom-pom. To characterize the mechanical properties in melt a dynamic frequency sweep was done at different temperatures to form a mastercurve in Figure 11.3. In the first part **a)**, the mastercurve is presented, in **b)** the Van Grup–Palmen plot visualizes the results without the time component. Two separate plateaus in $|G^*|$ are monitored in the Van Grup–Palmen plot, which are resulting from the relaxation of the backbone and the entire polymer, respectively.
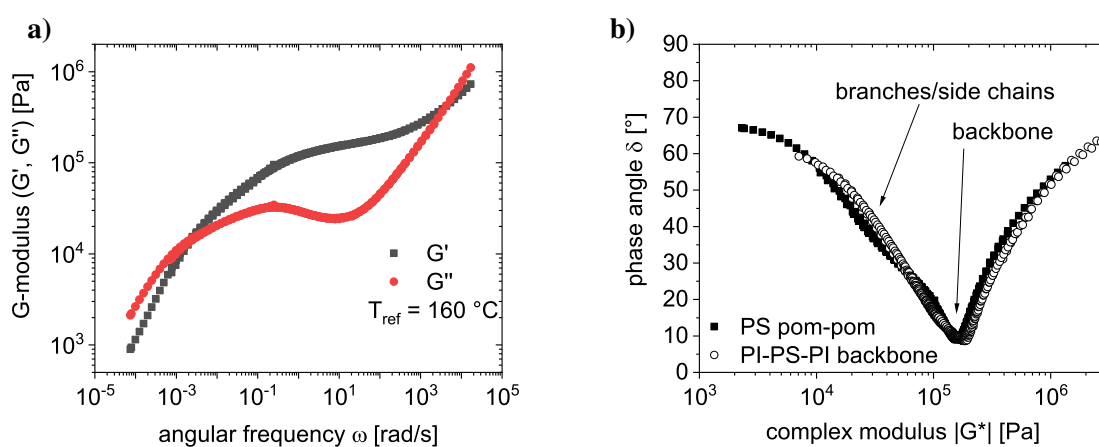
Figure 11.3. $T_{ref} = 160\,°C$ **a)** Mastercurve of the pom-pom with the parameters $M_{n,bb} = 360$ kg/mol, $M_{n,sc} = 135$ kg/mol and total number of side chains of both pom's is 42. **b)** Van Grup–Palmen of a). This presentation, has no time component, convex peaks indicate a rubber plateau with the respective modulus in $|G^*|$. Starting at high moduli, the first peak is very distinct an has typical values for a PS rubber plateau, the second 'plateau'/peak is very weak, nevertheless, it is a second relaxation mechanism.

To characterize the mechanical melt properties further, it is desirable to characterize the sample in elongation rheology. To do so, the sample was prepared in a rectangular shape of approx. $1\,mm \cdot 10\,mm \cdot 20\,mm$ in a mechanical press for 1 h with several $100\,M\,Pa$ at $180\,°C$ (and at $200\,°C$ in a second experiment). Upon loading the sample in to the elongation rheology geometry at measurement temperatures ($180\,°C$ to $220\,°C$), the sample showed strong wrinkles and was contracting, which indicates that the sample was still not in an isotropic melt after pressing into its form at elevated temperatures. Nevertheless, the sample was employed in elongation rheology experiments, however, the sample broke in its middle, which is completely unexpected for melt rheology experiments, and consequently, no reliable elongational rheology experiments can be presented.

To summarize, first rheology experiments on self-synthezied pom-poms were presented. Since the scientific community is in severe lack of characterized pom-poms, this way opens up a possibility to obtain rheological data on pom-pom. The used molecular weight $M_n = 6100$ kg/mol, has a high terminal relaxation time, consequently, the sample might be too big (in number and/or length of the side chains) to reach the flow regime, and consequently, hinders the sample preparation for elongational rheology measurements.

11.1.3 DSC characterization of PI

Within this thesis, the samples are characterized in a very broad temperature range, from $-80\,^\circ$C up to $220\,^\circ$C. A universal characteristic temperature for every polymer is the glass transition temperature (T_g). A T_g can be obtained by different methods such as rheology (including dynamical mechanic analysis), differential scanning calorimetry (DSC) or more uncommon methods like NMR. A widely used method is the characterization with DSC at a defined heating rate of 10 K/min, where the T_g is the inflection point in the heat flux, since the glass transition is a transition of 2nd order. Within this section, the DSC measurement of the sample PI-H68k-9-H14k, which was thoroughly characterized with other methods in the previous chapters is presented (refer to Figure 11.4). For sufficiently high molecular weights, T_g is basically independent from the molecular weight.[1] The herein presented trends are the same for all PI used in this work.
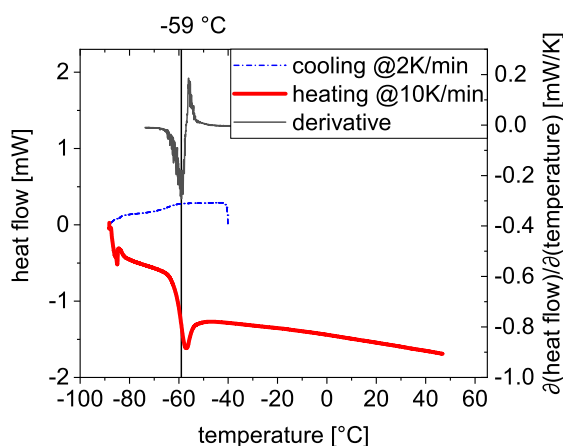
Figure 11.4. The DSC measurement of the sample polyisoprene sample PI-H68k-9-H14k (refer to 3.9 *Synthesis of partially a deuterated PI comb*, p. 50). The T_g is at $-59\,^\circ$C, with the derivative method at a heating rate of 10 K/min. The cooling rate (2 K/min) is slower than the heating rate (10 K/min), due to instrumental limitations. In the heating run after the glass transition temperature, there is a negative peak, which indicates that the sample is consuming heat energy. This is mostly related to frozen tension within the glassy sample. From ambient temperatures towards higher temperatures, the PI shows no phase transition.

A glass is a melt, that is frozen in its state on length scales of a few nm. Hereby the word 'frozen' means the stop of all segmental movements, and not the crystallization of a polymer (or freezing water to ice). Moreover, the density chances with T, which can lead to stress in the glassy polymer, even if the melt was tension free.[138] This phenomenon is observed in Figure 11.4 after T_g towards higher temperatures, where the stress release is consuming heat energy, since less stress increases the entropy.

---

[1]The T_g for different molecular weights can be predicted with $T_g = T_{g,\infty} - A/M_{\text{n}}$, where $T_{g,\infty}$ is the glass transition temperature for sufficiently high molecular weights and A is a parameter ($A = 100$ K/(kg/mol) for polystyrene, for isoprene much lower, however difficult do determine, since the micro-structure has a strong effect, too. In the literature no systematic changes in T_g above a molecular weight of $M_{\text{n}} = 10$ kg/mol for polyisoprene are reported.[136, 137]).

11.1.4 FT-Rheology on polymer rings

In this chapter the FT-Rheology on a polymer ring system is discussed. Since this is an ongoing project within this group, the results are presented separately from the results in 4 *Fourier transform rheology of homopolymer model system*, p. 54 and are to be taken as an outlook in this field.

The characterization of ring polymers has a renaissance in the recent years[139–143]. Ring polymer, in contrast to linear polymers, have no chain ends, consequently, the reptation mechanism as observed in linear or linear-derived architectures is not applicable to ring polymers. Consequently, the viscosity scaling law are different compared to liner polymers.[144] In addition to that, the conformation of the ring in the equilibrium melt state is different and more compact compared to linear polymers.[145–147]

For the synthesis the reader is referred to 3.7 *Synthesis of ring polymers*, p. 46. The received sample is has a purity of above 90 %.
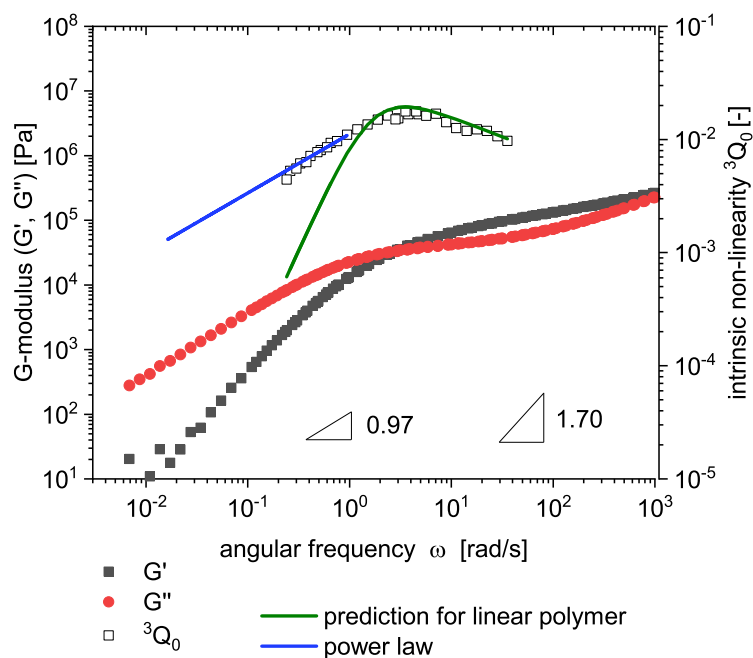
Figure 11.5. Linear and non-linear viscoelasticity if a PS ring with a molecular weight of 98 kg/mol at a reference temperature of $T_{\text{ref}} = 160\,°C$. The sample was kindly provided by Prof. Dr. J. P. Lutz. The sample has contaminations of linear PS. Comparable to the LVE of linear PS, the sample exhibits a rubber plateau and in LVE the flow regime has scaling law deviation from 1 and 2. The triangles represent the slopes in the terminal regime of G' and G'' respectively. In the intrinsic non-linearity, a strong difference to the prediction of the linear sample (refer to Equation 4.3, p. 57) is found. $^3Q_0$ is fitted with a power law of $^3Q_0(\omega) \propto \omega^{0.52}$.

The relaxation process of polymer rings is different, since common reptation is impossible.[148] In Figure 11.5 the oscillatory shear rheology characterization of a PS ring with a molecular weight of 98 kg/mol is presented. The entanglement molecular weight of PS is in the range of 18 kg/mol [149], however the concept of entanglements is not applicable in the same way as for linear polymers. Pure rings do not show a rubber plateau[150] and are very sensitive in melt rheology in the addition of linear chains. Since in Figure 11.5 a rubber plateau is found, the sample is contaminated with linear components.

Moreover, the scaling laws in the terminal regime derivate from 1 and 2. Additionally, the sample is characterized in FT-rheology and compared to the predictions[59] of a linear PS with the respective relaxation time and the same molecular weight. The comparison non-linear rheology of the linear and ring polymer show good agreement in the rubber plateau, however strong difference in the flow regime. All well entangled linear polymers show a power law exponent of 2 in the flow regime[1], but in the ring sample a power law exponent of 0.5 is observed.

The presented rheology results on PS rings indicate a different relaxation mechanism compared to linear PS, which was observed by the different slopes in the terminal regime of $^3Q_0$, compared to linear PS. Moreover, the slope of the intrinsic non-linearity in the flow regime, is a promising parameter to determine the purity of ring polymer melts.

11.2 FT-Rheology

Analysis of $^3Q_0$ as in Equation 4.13 with the free variable k, with the focus on the long component, which can be considered basically independent for a big contrast in the relaxation times. The case of reduced entanglements is considered.

$$^3Q_{0,L} = 0.32 \frac{\omega^2 \tau_L^2}{(\sqrt{Z_{L,eff}} \cdot (1 + 33.8(\omega\tau_L)^{2+k}/Z_{L,eff}))} \tag{11.1}$$

$$Z_{L,eff} = Z_L \cdot \phi_L^2 \tag{11.2}$$

$$^3Q_{0,L} = 0.32 \frac{\omega^2 \tau_L^2}{(\sqrt{Z_L \cdot \phi_L^2}(1 + 33.8(\omega\tau_L)^{2+k}/(Z_L \cdot \phi_L^2)))} \tag{11.3}$$

$$\frac{\partial}{\partial\omega}{}^3Q_{0,L} = 0.64 \frac{\omega\tau_L^2}{(\sqrt{Z_L \cdot \phi_L^2}(1 + 33.8(\omega\tau_L)^{2+k}/(Z_L\phi_L^2)))}$$
$$- 10.816 \frac{\omega \cdot \tau_L^2(\omega \cdot \tau_L)^{2+k}(2+k)}{(\sqrt{Z_L\phi_L^2}(1 + 33.8(\omega \cdot \tau_L)^{2+k}/(Z_L\phi_L^2))^2 \cdot Z_L\phi_L^2)} \tag{11.4}$$

$$\frac{\partial}{\partial\omega}{}^3Q_{0,L} \overset{!}{=} 0$$
$$\left(\omega_{max,L}, {}^3Q_{0,L}(\omega_{max,L})\right) = \left(\frac{\exp(\frac{-2.83 + \ln(Z_L L) + 2\ln(\phi_L) - \ln(k)}{2+k})}{\tau_L},\right.$$
$$\left.\frac{8\phi_L \exp(\frac{(-5.65 + 2\ln(Z_L) + 4\ln(\phi_L) - 2\ln(k))}{(2.+k)})\tau_L^2 \cdot k \cdot \sqrt{Z_L}}{(25Z_L\phi_L^2 \cdot k\tau_L^2 + 50Z_L \cdot \phi_L^2 \cdot \tau_L^2)}\right) \tag{11.5}$$

11.3 Instruments

SEC-MALLS

The molecular weights of the polymers were determined using size exclusion chromatography (SEC) equipped with multi angle laser light scattering (SEC-MALLS) from Polymer Standards Service, PSS, Mainz, Germany. The SEC equipment was from the Agilent1200 series, and the MALLS unit was the PSS SLD7000/BI-MwA, Brookhaven Instruments. The SEC measurements used THF as the solvent at 25 °C and a flow rate of 1 mL. The SEC columns from PSS (SDV-Lux-10^3 Å and 10^5 Å, 5 μm) were calibrated using linear PI or PS standards ranging from 476 g/mol to 2.5×10^6 g/mol.

SEC-preparative

A SEC-column from PSS, Mainz 'SDV linear M in THF', with a length of 300 mm, a diameter of 20 mm and a seperation range of 10^2 g/mol to 10^6 g/mol was used.

^{1}H-Spectroscopy

A 400 MHz Bruker Avance III Microbay spectrometer was used.

Rheology/RheoNMR

Small/Medium-amplitude oscillatory shear (SAOS/MAOS) and uniaxial extensional measurements were performed on an strain-controlled ARES-G2 rheometer from TA Instruments, using 13 mm plate-plate/cone-plate, respectively.

Rheo-NMR experiments were performed on an stress-controlled DHR3 rheometer from TA Instruments. The geometries for the Rheo-NMR experiments were designed by Dr. Karl-Friedrich Ratzsch. Pulsing, data acquisition, and processing were per-formed by a Bruker "the minispec" electronic unit.

D (3 : 1)

2,00 X 45°

Ø5,00
Ø8,00
Ø12,00

11,00
13,00

2,10
2,10
R1,50
R4,00
(1,20)

18,00
88,30

Ø14,00
1,30
Ø9,00
Ø13,00

83,50
3,50

D

R2,00
R10,20
Ø20

		Name	Date			
			27.03.2019	ratzsch		
	Drawn					
	Checked					
	Standard					

Rheo-Geo-Vane

1
A4

Name | Date | Changes | State

A–A (1 : 1)

74,40

Ø8,00

13,00

12,00

11,00

14,00

15,50

54,00

15,00

1,30

R2,00

R10,20

14,00

Ø14,00 $^{+0,00}_{-0,01}$

Ø20

A

A

84,50

3,50

89,30

PCTFE

Name

Date

Drawn

Checked

Standard

ratzsch

07.03.2019

Rheo-Geo-Cup

Name

Date

Changes

State

1

A4

11.4 Synthesis

Used chemicals

Argon (Air Liquide, N5=99.999 %), isoprene (Acros Organics, 98 %-stabilized), *n*-BuLi (2.5 mol/L in hexane, Sigma-Aldrich), *sec*-BuLi (1.4 mol/L in cyclohexane, Sigma Aldrich), 2,6-Di-*tert*-butyl-4-methylphenol (BHT) (99 %, VWR Chemicals), cyclohexane (99 %, ACROS Organics), styrene (99.5 %, Acros Organics), Calciumhydride (92 %, Akfa Aesar), di-*n*-butylmagnesium (1 mol/L in heptane, Aldrich), THF (ExtraPure, SLR, 0.025 % BHT, Fisher Chemical), sodium (Aldrich, dry), benzophenone (99 %, Aldrich), potassium (98 %, Acros Organics), methanol (99.8 %, VWR Chemicals), toluene (VWR Chemicalsm, 98 %), hydrogenperoxide (30 % in water, Acros Organics), formic acid (98 %, Fisher Chemical), lithiumchloride (98 %, wasserfrei, Alfa Aesar), potassium *tert*-butoxide (98 %, Aldrich), deuterium oxide (99.9 d%, Aldrich), diglyme (diethylene glycol dimethyl ether, anhydrous,99.5 %, Aldrich), calcium carbide (80 %, Aldrich), $CaCl_2$ (anhydrous, 93.0 %, Aldrich), α, α'-dibromo-*p*-xylene (97 %, Aldrich), 2,2'-Azobis[2-(2-imidazolin-2-yl)propane]dihydrochloride (VA-044, 95 %, FUJIFILM Wako Pure Chemical).

Preparations for anionic synthesis and baking out the glassware

A Schlenk-line was used with argon and a vacuum down to 10^{-3} mbar for all steps related to anionic synthesis. All glassware was boro-silica glass and the joints were greased with PTFE-paste. All glassware in water/oxygen-sensitive steps was baked out (German: *ausheizen*) by heating, evacuating and flushing with argon for a total of three times. All water and oxygen sensitive steps were done in closes glass environments and by glassware that is connected through glass joints, unless noted otherwise.

Drying of isoprene

Isoprene was dried over *n*-BuLi twice according to the following procedure. The *n*-BuLi solutions were added into two respective flasks (first flask 0.25 mmol *n*-BuLi/1 mL isoprene, seconds flask 0.125 mmol *n*-BuLi/1 mL isoprene), and then the solvent was removed under reduced pressure. Afterwards, isoprene was added into the first flask and stirred for 30 min at 0 °C. Subsequently, the isoprene was distilled into the second flask, while keeping the distillation sump below 0 °C *via* cooling the second flask with liquid nitrogen. The solution was stirred for 30 min at 0 °C as well. The dry isoprene was distilled, in the same way as reported, into an empty flask for storage. The isoprene was always freshly prepared prior to any further synthesis.

Drying of styrene

Styrene was dried over CaH_2 and di-*n*-butylmagnesium according to the following procedure. The CaH_2 and di-*n*-butylmagnesium were added into two respective flasks (first flask 5 g CaH_2, seconds flask 0.125 mmol di-*n*-butylmagnesium/1 mL isoprene), and then the solvent was removed under reduced pressure. Afterwards, styrene was added into the first flask and stirred for 1 d at ambient temperatures.

Subsequently, the styrene was distilled into the second flask, while heating the distillation sump to 70 °C *via* cooling the second flask with liquid nitrogen. The solution was stirred for 30 min at 0 °C. The dry styrene was distilled, in the same way as reported, into an empty flask for storage. The styrene was always freshly prepared prior to any further synthesis. After multiple weeks the destabilized and dry styrene turns in to a high viscous liquid, cooling in a freezer does not significantly inhibit this process.

Drying and storing of cyclohexane

Cyclohexane, as received, was put into the storage flask. To that, short chained polystyrene $M_n \approx$ 10 kg/mol and *sec*-BuLi solution (1.4 M, 1 mL/50 mL cyclohexane) was added and stirred over night. A orange color indicates dryness.

Drying and storing of THF

THF was stored in a distill over an excess of CaH_2 and stirred under reflux for 5 h. Then the THF was distilled and added into a Schlenk-flask over sodium (1 g/50 mL THF) and an excess of benzophenone for storage. The mixture was sirred under static vacuum over night, until a violet color indicates dryness. For cleaning the distill, the CaH_2 or sodium is quenched under inert gas, while having an excess of THF (50 mL per gram of the to be quenched substance) by adding very slowly a mixture of 9 parts THF and 1 part water. Adding MeOH to CaH_2 is dangerous, since it might retard the reaction.

Potassium naphthalenide

Approx. 3 g of potassium is cut under cyclohexane and added into a backed-out flask. Into this flask, dry THF is distilled and stirred over night. To the very light blueish mixture, naphthalene (1. equiv., *e.g.,* 0.5 g (3.90 mmol) per 50 mL THF) is added. The generation of a blackish green color indicates conversion. The mixture is stirred overnight, filtered by employing glass frittes and used up within one week.

Polymerization of isoprene to PI

About 150 mL dry cyclohexane was distilled into a round bottom flask. 14.8 mL (10.0 g, 0.147 mol) dry isoprene was added with a flushed syringe. *sec*-BuLi solution was added (1 equiv. per polymer chain *e.g.,* 0.71 mL of a 1.4 mol/L *sec*-BuLi solution for a molecular weight of 10 kg/mol). The mixture was stirred at ambient temperatures over night, where the viscosity sharply increased. For molecular weights above 100 kg/mol, the mixture was stirred for a total of two days. The polymerization was terminated by adding about 0.1 mL of degassed methanol. For the backbone of the sample PI-H68k-9-H14k and PI-D72k-9-H14k, the methanol was distilled onto the polymerization mixture.
If the polymer is prepared for storage 1 wt% 2,6-Di-*tert*-butyl-4-methylphenol (BHT) per PI is added.
The solvent of polymer solution is evaporated under reduced pressure until a pressure of 10 mbar. Then it is further dried under reduced pressure (10 mbar) and a small nitrogen flux (1 mmol/s) for two days at 60 °C. The PI is received as a high viscous and transparent polymer melt.

The PI is characterized by SEC and NMR.

[1]H δ(CDCl$_3$): 5.05 (0.93 H [93 % 1,4-*cis* and *trans*], **C=CH**), 4.69+4.61 (0.14 H [7 % 3,4], vinyl-group), 1.97-1.18 (7 H, aliphatic protons).

Removing the stabilizer from PI

The stabilized PI is dissolved in cyclohexane, then the cyclohexane is removed under reduced pressure, while rotating the flask to receive a thin film of PI in the glass surface. Distilled methanol is added and then waited for 1 day, then the methanol is removed by decantation. Distilled methanol is added and then waited for 1 day, then the methanol is removed by decantation. The PI is dissolved in cyclohexane, then the cyclohexane is removed under reduced pressure. Since the destabilized PI is used immediately, no further drying is required.

Epoxidation of PI

About 5 g of PI without stabilizer is put into a round bottom flask and dissolved in 50 mL toluene. 1 equiv. in this synthesis refers to 1 resulting epoxy group. Hydrogenperoxide (3 equiv.) and formic acid (3 equiv.) are added and stirred violently over night. The emulsion is washed with water until being pH neutral (for the samples PI-H68k-9-H14k and PI-D72k-9-H14k this step is skipped). The toluene is evaporated under reduced pressure (the resulting polymer is milky), and the sample is dried further by dissolving in THF and removing the THF by reduced pressure until the sample is no longer milky. A sample is taken and characterized by NMR (400 MHz). Then the sample is dissolved in about 100 mL THF. The polymer solution is received as a viscous colorless solution.

Fractioned proton integrals are a result of the micro-structure distribution - [1]H δ(CDCl$_3$): 5.05 (0.89 H [89 % 1,4-*cis* and *trans*], **C=CH**), 4.69+4.61 (0.10 H [5 % 3,4], vinyl-group), 2.62 (0.06 H [6 % epoxidized **C=CH**]), 1.97-1.18 (7 H, aliphatic protons).

Preparation of a LiCl solution

4 g (94.3 mmol) is added into a storage flask and backed out for 1 h under vacuum. About 95 mL of dry THF is distilled into the flask and stored. A milky dispersion is received with a LiCl concentration of 0.89 mol/L that has to be shaken up prior usage.

Comb grafting of PI - contaminated with small polymers

Prior any further steps living anions are prepared in the same way as in *Polymerization of isoprene to PI* (until [and excluding] the step of adding methanol) and a functionalized linear PI is provided in a solution of THF. To the solution of epoxidized PI 2 equiv. LiCl as a solution in THF is added and the mixture is cooled to 0 °C. Living PI anions are successively added until the desired decree of conversion is reached. To determine the degree of conversion the mixture is stirred for 1 h and then characterized by

SEC-MALLS. After the full conversion the sample is quenched by 0.1 mL of degassed methanol. The polymer mixture is received as a solution of comb polymers and residual side chains.

Purification of combs in bulk

The raw contaminated comb solution, *e.g.,* as in *Comb grafting of PI - contaminated with small polymers* is dissolved in a total of 500 mL THF in a beaker. To this, methanol is added until the precipitated polymer does not dissolve anymore under stirring. The mixture is heated to about 35 °C until the precipitated polymer is dissolved again and then cooled down to ambient temperatures over night, while being covered by aluminum foil. Hereby, phase separation occurs, with an upper low viscous phase that makes of to the majority and a bottom viscous phase that is typically in the range of less than 10 mL. Both phases are characterized by SEC and the fractions of the comb is calculated. In the upper phase the residual side arms are enriched, and in the bottom phase the comb is enriched. The upper phase is discard (after being stored until the purification had been finished) and for the bottom phase this purification step is repeated until the amount of residual side arms is less than 5 %. The sample is dried under reduced pressure, dissolved in cyclohexane and stabilized with 1 wt% 2,6-di-*tert*-butyl-4-methylphenol (BHT). The solvent of polymer solution is evaporated under reduced pressure until a pressure of 10 mbar. Then it is further dried under reduced pressure (10 mbar) and a small nitrogen flux (1 mmol/s) for two days at 60 °C. The PI is received as a high viscous and transparent polymer melt.
The PI is characterized by SEC and NMR.

Purification of combs by SEC

The raw contaminated comb (or pom-pom) solution, *e.g.,* as in *Comb grafting of PI - contaminated with small polymers* employed by fist evaporating the solvent and dissolving in THF (SEC grade) for a 1 wt% solution. The solution is put into SEC vials and the seperated by SEC with a fraction collector by employing 30 μL injections. After a sufficient amount was collected, the solvent is removed under reduced pressure ($T = 40$ °C), the BHT is removed as in *Removing the stabilizer from PI* and then stabilized with 1 wt% BHT as in *Polymerization of isoprene to PI*.
The PI is characterized by SEC and NMR.

PI-PS-PI triblock-co-polymers

The polymerization procedure is the same as in *Polymerization of isoprene to PI*, except that instead of terminating the PI, styrene is added to form the second block and is stirred for 1 d, then isoprene is added to form the third block and stirred for 1 d, and finally it is terminated with methanol. Since the products in this work are primary PS with little PI on the chain ends, the polymer is characterized with SEC and a PS standard.

PS pom-pom grafting

First a PI-PS-PI triblock is synthesized as in *PI-PS-PI triblock-co-polymers*, then the triblock is fully epoxidized as in *Epoxidation of PI*- a meaningful NMR is not applicable, since the epoxidized groups overlap with the PS.

Then a linear living PS is synthezied in the same was as in *Polymerization of isoprene to PI*, except that the monomer is styrene and the living anion is not terminated.

To the epoxidized PI-PS-PI in a solution in THF LiCl-solution is added (1 equiv. per isoprene unit) and then mixed with the living PS anions.

The resulting pom-poms are purified as in *Purification of combs by SEC*, then characterized using SEC-MALLS.

PS ring grafting

Potassium naphthalenide (4 mmol) was added into 400 mL of dry THF that is cooled to −70 °C. 20 g of styrene, diluted with a four-fold excess of THF, is added over a time of 1 h, turning the green solution red within 5 drops to 10 drops. Then the solution is stirred at −70 °C for a 1 h.

A 1 L round bottom flask is prepared with 300 mL of dry THF, moreover a solution of α, α'-dibromo-*p*-xylene in THF is prepared and attached to the flask. The living anions of the polymerization mixture and the α, α'-dibromo-*p*-xylene solution is added alternating into the flask in small quantities until a color change is observed. Up to 100 alternations were performed. The residual living anion solution in the polymerization flask is quenched with methanol and the sample is taken as the linear reference. The sample is characterized by SEC, with a ring content of up to 40 % of the sample PS-ring10k (PS ring, monodisperse 10 kg/mol). The apparent ring molecular weight shows up 10 % decrease in molecular weight compared to the molecular weight of the linear reference.

PS ring purification

The samples received in *PS ring grafting* are a combination of rings and extended condensation products. To purify the ring the sample is dissolved in toluene and methanol is added until the sample starts to precipitate (to total volume is aimed to be 1 L). The mixture is heated until it is dissolved again and then put into a preheated separating funnel. After 1 d two phases have formed, the lower phase being yellow-greenish shiny, the lower phase is separated and stored until the purification is finished, then discarded. The upper phase has an enriched ring content. The upper and the lower phase are characterized. The contamination content is calculated as the fraction of the shoulder towards higher molecular weights. The entire purification circle is repeated until the contamination content does not change significantly anymore, for a total of up to 27 times.

Deuterated 2-methyl-3-butin-2-ol

Adapted from literature.[60] 256 g potassium *tert*-butoxide (2.29 mol, 1 equiv.) was put into a 1 L round bottom flask under inert atmosphere and mixed with 250 g deuterium oxide under constant cooling. The mixture was partially evaporated under reduced pressure and elevated temperatures (80 °C, 10 mbar), while rotating until the mixture crystallized. The mixture was further reduced at elevated temperatures and reduced pressure (140 °C, 10^{-3} mbar) until the mixture turned solid again. After weighting, a purity of 91.2 wt% (with the rest residual heavy water) was calculated.

To the KOD about 300 mL diglyme was added under inert atmosphere and mixed at 180 °C under inert atmosphere, until two liquid phases appeared. Multiple batches of mixtures of KOD and diglyme were combined in a three neck round bottom flask. The mixture was heated to 160 °C and then gradually cooled to −5 °C under inter atmosphere, to form a brownish slurry of KOD in diglyme (the color is a residue of impurities of the potassium *tert*-butoxide).

450 g of calcium carbide (360 g pure calcium carbide, 5.61 mol) was mixed in a three necked round bottom flask with 400 mL diglyme and stirred constantly. 150 g deuterium oxide was added in the time range of 1 h, while the reaction mixture was cooled with ice to keep the reaction temperature below approx. 60 °C. The freshly generated acytelene was first dried with $CaCl_2$ and then transferred into the KOD slurry with a minor argon flux.

To the KOD slurry and the disolved acetlyene 97.7 g acetone-d6 (113 mL, 1.53 mol, 1.76 equiv.) was added in 2 h. The mixture was quenched with 375 g of deuterium oxide until two clear, yet dirty phases became visible. The organic phase was separated and the aqueous phase was extracted with ether twice. The organic phase was neutralized with dry ice. The organic phase was distilled (98 °C) to receive 60.0 g (0.652 mol) of the colorless liquid 2-methyl-3-butin-2-ol.

^{2}H δ(CDCl$_3$): 2.41 (s, 1 D, D-C≡C), 1.48 (m, 6 D, D$_3$-C).

Deuterated 2-methyl-3-buten-2-ol

Adapted from literature.[60] 1 g Lindlar catalyst (Pd/C/Pb) was added in the reactor with 60 g the 2-methyl-3-butin-2-ol (0.652 mol). The sample was degassed at −50 °C and reduced pressure. Then the sample was hydrated with D$_2$, while tracking the pressure in the reactor. D$_2$ was added until its conversion speed significantly dropped. The sample was filtered and characterized. The sample (41 g, 0.476 mol) was received as a brownish liquid.

^{2}H δ(CDCl$_3$): 3.58 (m, 1 D, **D$_2$**-C=**CD**-C), 3.50 (m, 1 D, **D$_2$**-C=**CD**-C), 3.42 (m, 1 D, **D$_2$**-C=**CD**-C), 1.44 (m, 6 D, D$_3$-C).

Deuterated isoprene

Adapted from literature.[60] A dropping funnel was prepared with 41 g deuterated 2-methyl-3-buten-2-ol (0.476 mol), a glass pipe filled with Al$_2$O$_3$ beads was prepared and heated to 300 °C and flushed with argon 600 mL/min. The deuterated 2-methyl-3-buten-2-ol was slowly dripped into a round bottom flask, which is heated to 160 °C, and therefore transported through the Al$_2$O$_3$. The product is received in a

flask that is cooled to −70 °C. The raw product is purified in a distillation to remove excess water, then characterized and stored with 1 wt% BHT. The deuterated isoprene is received as 29 g (0.382 mol, total yield in reference to the potassium *tert*-butoxide of 4 %) a a clear characteristically smelling liquid.

^{2}H δ(CDCl$_3$): 6.52 (m, 1 D, D$_2$-C=**CD**-**CD**(CD$_3$)=CD$_2$), 5.18 (m, 4 D, **D$_2$**-C=**CD**-CD(**CD$_3$**)=**CD$_2$**), 1.87 (m, 3 D, D$_3$-C).

11.5 Dispersity distribution prediction for polymer combs

The following code allows the Gaussian propagation of uncertainty, which was applied to the grafting of the polymer combs. The M_n and the backbone are essentially the expectation value for a random draw and standard deviation is given by $Đ = (\sigma/\mu + 1)$. The number o sidearms is assumed to be a statistical event, resulting in Poisson distribution. The Poisson distribution (of k events) is simplified to a normal distribution with $n_{sc} = k$ and $\Delta n_{sc} = \sqrt{k}$). The script is written with maple© and tested in version 15 and 2020.

```
1  >>
2  Fehler := proc(name::name,term,var::set)
3  local liste,i,t1,t2,o1,o2;
4  description 'ein Programm zum Berechnen der partiellen Ableitungen und zur Berechnung des
       fortgepflanzten Fehlers. Geschrieben und getestet in Maple 15; author: Jonas Keller';
5  liste:={};
6  for i from 1 to nops(var) do
7  if type(var[i][1],protected) or var[i][1]=I then print(var[i][1],"ist eine geschuetzter
       Variablenname, bitte einen anderen benutzten");fi;
8
9  #ableiten
10 t1:=diff(term, var[i][1]);
11 #in die partielle Ableitung einsetzten und mal Delta<Name>
12 t2:= var[i][3]*eval(t1,{seq(var[x][1] = var[x][2],x=1..nops(var))});
13 #Erstellen erweiterter Liste aus Segmenten mit folgendem aufbau: [Name, Wert, Fehler,
       partielle Ableitung, Ergebnis der partiellen Ableitung mal Fehler]
14 liste:= liste union {[var[i][1] ,var[i][2],var[i][3], t1,t2]};
15 od;
16 #Visuelle Darstellung der Fehlerquadrate, die Wurzel wird spaeter hinzugefuegt das &*
       verhindert, dass die Zahlen "echt" multipliziert werden und sich in irgendeiner weise so
       umformen, dass es nicht mehr schoen aussieht
17 #ist der Fehler 0 so wird das Segment ignoriert
18 o1:=add( 'if'(evalb(liste[x][3]=0),0,
19 (liste[x][4]&*(Delta*liste[x][1]))^2),x=1..nops(liste));
20 #Berechnung des Fehlers aus den Fehlerquadraten
21 o2:=evalf(sqrt(add( (liste[x][5])^2,x=1..nops(liste)  )));
22 #Begin der Ausgabe
23 #Zuerst eine zusammenfassung der Eingabe
24 print('Gegeben:' , Array([['Gleichung:'],[name = term]]),
25 Array([['Wert','Fehler'], seq([liste[x][1]=liste[x][2],
26 Delta*liste[x][1]=liste[x][3]],x=1..nops(liste))]) );
27
28 #Ausgabe der "Visuellen Darstellung der Fehlerquadrate"
29 print(Array([Delta*name = sqrt(o1)]));
30 #Ausgabe des Erwartungswertes und dessen Fehler
31 print(Array([['Zusammenfassung:'],
32 [name=evalf(eval(term,{seq(var[x][1] = var[x][2],x=1..nops(var))}))
33 ],[Delta*name=o2]]));
34 end proc;
35 >>
36 Fehler(Mn,Mnbb+nsc*Mnsc,{[Mnbb,66000,66000*sqrt(1.02-1)],[nsc,(8.5),
37 sqrt(8.5)],[Mnsc,13400,13400*sqrt(1.02-1)]});
```

List of Figures

XI

List of Tables

Acknowledgments

The PhD thesis, although being written by me, would not have been possible, if not for the scientific, structural, financial and emotional support. Therefore, I acknowledge the contribution of several people:

Prof. Dr. M. Wilhelm

As my supervisor, the entire research is based on his ideas, and therefore, not possible without him. I am thankful for the scientific support, the encouragements, the travel opportunities (for the months abroad at Caltech-university and the conferences), for all the insightful discussions and the freedom to try out my own ideas.

Deutsche Forschungs Gesellschaft

For partially funding my position. (Project 265358506, Geschäftszeichen(KIT): WI 1911/23-1)

Prof. Dr. K. Saalwächter

As the collaboration partner, of the DFG-project that my thesis is based on. For the insightful discussion and experiments, especially when I visited his group in Halle.

Prof. Dr. J. Kornfield

For the possibility to stay in her group at Caltech for three months. In this time, I have learned a lot and I have developed further. I have able to learn plenty from her and her group.

C. K. Georgantopoulos, C. Fengler, Dr. M. Cziep, L. Fischer, M. Schäfer, Dr. V. Hirschberg, C. Botha, Dr. S. Nie, M. Hoffman and M. C. Röpert

As members of our group that have contributed to our joint research projects, all the discussions and corrections.

Our WiDo group

I thank everyone, in the group for the pleasant atmosphere. For all the help, and keeping the work live balance in check with the coffee breaks and the bbqs.

Dr. K.-F. Ratzsch

As a member of our group and later as part of Bruker for answering all my annoying questions related to NMR.

Dr. A. Mordvinkin and F. Shahsavan

As members of K. Saalwächters group, for the training in NMR and the fruitful collaboration.

Dr. J. Allgaier and A. Raba

From the Jülich center for neutron scattering, for the joint synthesis and discussions around deuterated monomers.

Dr. T. Di Luccio

For the joint research at Caltech and her hospitality during my time in the USA.

Eyleen, Fabian, Johannes, Maxi and Michael

We share a long way, thank you!

Aaron, Christoph, Christoph2 and Tobias

Our joint times, studying and our card group, you are awesome!

Inge, Peter, Charlotte and Johanna

Thank you for all the support and encouragements, not only during my PhD, but through my entire studies.

Janin

For your time, love and support, especially in lenient times, you know I am not good with words, therefore: THANK YOU!

Bibliography

[1] M. A. Cziep, M. Abbasi, M. Heck, L. Arens, M. Wilhelm, *Macromolecules* **2016**, *49*, 3566.

[2] plasticseurope, Plastics - the Facts 2019, https://www.plasticseurope.org/de/resources/publications/2154-plastics-facts-2019 [Online; accessed 29. Apr. 2020].

[3] H. Staudinger, *Ber. dtsch. Chem. Ges. A./B* **1920**, *53*, 1073.

[4] H. Staudinger, J. Fritschi, *Helv. Chim. Acta* **1922**, *5*, 785.

[5] Š. Podzimek, *Light scattering, size exclusion chromatography and asymmetric flow field flow fractionation: powerful tools for the characterization of polymers, proteins and nanoparticles*, Wiley, Hoboken, NJ, **2011**.

[6] W. Lee, H. Lee, J. Cha, T. Chang, K. J. Hanley, T. P. Lodge, *Macromolecules* **2000**, *33*, 5111.

[7] M. Szwarc, *Nature* **1956**, *178*, 1168.

[8] P. J. Flory, *J. Am. Chem. Soc.* **1940**, *62*, 1561.

[9] H. Frey, T. Ishizone, *Macromol. Chem. Phys.* **2017**, *218*, 1700217.

[10] H.-D. Brandt, W. Nentwig, N. Rooney, R. T. LaFlair, U. U. Wolf, J. Duffy, J. E. Puskas, G. Kaszas, M. Drewitt, S. Glander in *Ullmann's Encyclopedia of Industrial Chemistry*, American Cancer Society, **2011**.

[11] D. Braun, H. Cherdron, M. Rehahn, H. Ritter, B. Voit, *Polymer Synthesis: Theory and Practice*, Springer, Berlin, **2013**.

[12] N. Hadjichristidis, A. Hirao, *Anionic Polymerization*, Springer, Tokyo, **2015**.

[13] D. Baskaran, A. H. E. Müller, *Prog. Polym. Sci.* **2007**, *32*, 173.

[14] A. Takano, O. Kadoi, K. Hirahara, S. Kawahara, Y. Isono, J. Suzuki, Y. Matsushita, *Macromolecules* **2003**, *36*, 3045.

[15] B. Vollmert, J. X. Huang, *Makromol. Chem. Rapid Commun.* **1981**, *2*, 467.

[16] W. Gebert, J. Hinz, H. Sinn, *Makromol. Chem.* **1971**, *144*, 97.

[17] V. H. Sinn, C. Lundborg, O. T. Onsager, *Makromol. Chem.* **1964**, *70*, 222.

[18] R. S. Stearns, L. E. Forman, *J. Polym. Sci.* **1959**, *41*, 381.

[19] R. P. Quirk, W.-C. Chen, *J. Polym. Sci. Polym. Chem. Ed.* **1984**, *22*, 2993.

[20] M. Szwarc, M. Levy, R. Milkovich, *J. Am. Chem. Soc.* **1956**, *78*, 2656.

[21] M. Abbasi, L. Faust, K. Riazi, M. Wilhelm, *Macromolecules* **2017**, *50*, 5964.

[22] G. Koutalas, H. Iatrou, D. J. Lohse, N. Hadjichristidis, *Macromolecules* **2005**, *38*, 4996.

[23] J. Zhao, G. Zhang, S. Pispas, *J. Polym. Sci. Part A: Polym. Chem.* **2010**, *48*, 2320.

[24] H. Tobita, *Polymer* **1997**, *38*, 1705.

[25] T. Higashihara, R. Faust, K. Inoue, A. Hirao, *Macromolecules* **2008**, *41*, 5616.

[26] J. M. Dealy, D. J. Read, R. G. Larson, *Structure and Rheology of Molten Polymers*, Hanser, **2018**.

[27] H. A. Barnes, *A Handbook of Elementary Rheology*, University of Wales, **2000**.

[28] C. W. Macosko, *Rheology Principles*, VCH Publishes, **1994**.

[29] A. Malkin, A. Y. Malkin, *Rheology fundamentals*, ChemTec publishing, **1994**.

[30] T. Mezger, *Vincentz Network Hannover Germany* **2006**, 299.

[31] R. H. Ewoldt, G. H. McKinley, *Rheol. Acta* **2010**, *49*, 213.

[32] M. L. Williams, R. F. Landel, J. D. Ferry, *J. Am. Chem. Soc.* **1955**, *77*, 3701.

[33] R. H. Ewoldt, N. A. Bharadwaj, *Rheol. Acta* **2013**, *52*, 201.

[34] K. Hyun, M. Wilhelm, *Macromolecules* **2009**, *42*, 411.

[35] P. Poungthong, A. J. Giacomin, C. Saengow, C. Kolitawong, *J. Non-Newtonian Fluid Mech.* **2019**, *265*, 53.

[36] R. Kimmich, *Principles of Soft-Matter Dynamics - Basic Theories, Non-invasive Methods, Mesoscopic Aspects*, Springer Netherlands, **2012**.

[37] P. E. Rouse, *J. Chem. Phys.* **1953**, *21*, 1272.

[38] M. Doi, S. F. Edwards, S. F. Edwards, *The theory of polymer dynamics*, *Vol. 73*, Oxford university press, **1988**.

[39] A. Y. Grosberg, A. R. Khokhlov, H. E. Stanley, A. J. Mallinckrodt, S. McKay, *Statistical physics of macromolecules*, *Vol. 9*, American Institute of Physics, **1995**, p. 171.

[40] B. Blümich, *Essential NMR*, Springer, **2019**.

[41] K. Schmidt-Rohr, H. W. Spiess, *Multidimensional solid-state NMR and polymers*, Elsevier, **2012**.

[42] CODATA Value: electron gyromagnetic ratio, https://physics.nist.gov/cgi-bin/cuu/Value?gammae [Online; accessed 30. May 2020].

[43] B. Blümich, *NMR imaging of materials*, Clarendon Press, Oxford, **2000**.

[44] N. Bloembergen, E. M. Purcell, R. V. Pound, *Phys. Rev.* **1948**, *73*, 679.

[45] H. Y. Carr, E. M. Purcell, *Phys. Rev.* **1954**, *94*, 630.

[46] S. Meiboom, D. Gill, *Rev. Sci. Instrum.* **1958**, *29*, 688.

[47] P. Giraudeau, *Magn. Reson. Chem.* **2014**, *52*, 259.

[48] L. Braunschweiler, G. Bodenhausen, R. R. Ernst, *Mol. Phys.* **1983**, *48*, 535.

[49] D. Shykind, J. Baum, S.-B. Liu, A. Pines, A. Garroway, *J. Magn. Reson.* **1988**, *76*, 149.

[50] K. Saalwächter, *Progr. NMR Spectrosc.* **2007**, *51*, 1.

[51] K. Saalwächter, P. Ziegler, O. Spyckerelle, B. Haidar, A. Vidal, J.-U. Sommer, *J. Chem. Phys.* **2003**, *119*, 3468.

[52] D. Suter, S. B. Liu, J. Baum, A. Pines, *Chem. Phys.* **1987**, *114*, 103.

[53] D. Besghini, M. Mauri, R. Simonutti, *Applied Sciences* **2019**, *9*, 1801.

[54] J. Baum, M. Munowitz, A. Garroway, A. Pines, *J. Chem. Phys.* **1985**, *83*, 2015.

[55] M. Kikuchi, M. Azumi, *Frontiers in Fusion Research II*, Springer International Publishing, Cham, Switzerland, **2015**.

[56] J. D. Londono, A. H. Narten, G. D. Wignall, K. G. Honnell, E. T. Hsieh, T. W. Johnson, F. S. Bates, *Macromolecules* **1994**, *27*, 2864.

[57] R. Brückner, *Reaktionsmechanismen*, 3. Aufl., aktualisiert und überarb., Elsevier, Spektrum Akad.-Verl., Heidelberg, **2004**.

[58] Z. Yuan, M. Gauthier, *Macromolecules* **2005**, *38*, 4124.

[59] M. A. Cziep, PhD thesis, Karlsruher Institut für Technologie (KIT), Karlsruhe, Germany, **2019**.

[60] D. Craig, F. A. Regenass, R. B. Fowler, *J. Org. Chem.* **1959**, *24*, 240.

[61] G. Bishko, T. C. B. McLeish, O. G. Harlen, R. G. Larson, *Phys. Rev. Lett.* **1997**, *79*, 2352.

[62] J. S. Keller, C. K. Georgantopoulos, M. Wilhelm, *Rheol. Acta* **in perparation**.

[63] M. H. Wagner, V. H. Rolón-Garrido, K. Hyun, M. Wilhelm, *J. Rheol.* **2011**, *55*, 495.

[64] J. G. Nam, K. Hyun, K. H. Ahn, S. J. Lee, *J. Non-Newtonian Fluid Mech.* **2008**, *150*, 1.

[65] J. G. Nam, K. H. Ahn, S. J. Lee, K. Hyun, *J. Rheol.* **2010**, *54*, 1243.

[66] H. Y. Song, K. Hyun, *Korea-Aust. Rheol. J.* **2019**, *31*, 1.

[67] D. M. Hoyle, D. Auhl, O. G. Harlen, V. C. Barroso, M. Wilhelm, T. C. B. McLeish, *J. Rheol.* **2014**, *58*, 969.

[68] H. Y. Song, O. S. Nnyigide, R. Salehiyan, K. Hyun, *Polymer* **2016**, *104*, 268.

[69] C. Hershey, K. Jayaraman, *J. Polym. Sci. Part B: Polym. Phys.* **2019**, *57*, 62.

[70] R. Kádár, M. Abbasi, R. Figuli, M. Rigdahl, M. Wilhelm, *Nanomaterials* **2017**, *7*, 23.

[71] R. Kádár, K. Gaska, T. Gkourmpis, *Rheol. Acta* **2020**, *59*, 333.

[72] S. Nie, J. Lacayo-Pineda, M. Wilhelm, *Soft Mater.* **2019**, *17*, 269.

[73] O. Carey-De La Torre, R. H. Ewoldt, *Korea-Aust. Rheol. J.* **2018**, *30*, 1.

[74] V. Hirschberg, F. Lacroix, M. Wilhelm, D. Rodrigue, *Mech. Mater.* **2019**, *137*, 103100.

[75]   V. Hirschberg, L. Schwab, M. Cziep, M. Wilhelm, D. Rodrigue, *Polymer* **2018**, *138*, 1.

[76]   V. Hirschberg, M. Wilhelm, D. Rodrigue, *Polym. Test.* **2017**, *60*, 343.

[77]   S. Filipe, I. Vittorias, M. Wilhelm, *Macromol. Mater. Eng.* **2008**, *293*, 57.

[78]   D. J. Read, D. Auhl, C. Das, J. Den Doelder, M. Kapnistos, I. Vittorias, T. C. B. McLeish, *Science* **2011**, *333*, 1871.

[79]   I. Vittorias, M. Wilhelm, *Macromol. Mater. Eng.* **2007**, *292*, 935.

[80]   R. J. Blackwell, T. C. B. McLeish, O. G. Harlen, *J. Rheol.* **1999**, *44*, 121.

[81]   M. H. Wagner, J. Schaeffer, *Rheol. Acta* **1994**, *33*, 506.

[82]   M. H. Wagner, J. Schaeffer, *J. Rheol.* **1998**, *37*, 643.

[83]   M. H. Wagner, J. Schaeffer, *Rheol. Acta* **1992**, *31*, 22.

[84]   C. Iacob, T. Yoo, J. Runt, *Macromolecules* **2018**, *51*, 4917.

[85]   V. A. H. Boudara, J. D. Peterson, L. G. Leal, D. J. Read, *J. Rheol.* **2019**, *63*, 71.

[86]   A. E. Likhtman, R. S. Graham, *J. Non-Newtonian Fluid Mech.* **2003**, *114*, 1.

[87]   B. Robertson, R. L. Thompson, T. C. B. McLeish, I. Robinson, *J. Rheol.* **2019**, *63*, 319.

[88]   S. H. Tabatabaei, P. J. Carreau, A. Ajji, *Polym. Eng. Sci.* **2021**, *50*, 191.

[89]   V. A. H. Boudara, J. D. Peterson, L. G. Leal, D. J. Read, *J. Rheol.* **2018**, *63*, 71.

[90]   V. A. H. Boudara, D. J. Read, J. Ramírez, *J. Rheol.* **2020**, *64*, 709.

[91]   D. J. Read, K. Jagannathan, S. K. Sukumaran, D. Auhl, *J. Rheol.* **2012**, *56*, 823.

[92]   H. Watanabe, S. Ishida, Y. Matsumiya, T. Inoue, *Macromolecules* **2004**, *37*, 6619.

[93]   E. van Ruymbeke, Y. Masubuchi, H. Watanabe, *Macromolecules* **2012**, *45*, 2085.

[94]   R. H. Colby, M. Rubinstein, *Macromolecules* **1990**, *23*, 2753.

[95]   S. Zhu, D. Li, W. Zhou, C. M. Crowe, *Polymer* **1998**, *39*, 5203.

[96]   H. Tobita, *Macromol. Theory Simul.* **1996**, *5*, 1167.

[97]   H. Watanabe, *Prog. Polym. Sci.* **1999**, *24*, 1253.

[98]   T. C. B. McLeish, *Adv. Phys.* **2002**, *51*, 1379.

[99]   N. Rudolph, T. A. Osswald, *Polymer Rheology - Fundamentals and Applications*, Carl Hanser Verlag GmbH Co KG, M, **2014**.

[100] W. H. Stockmayer, *Pure Appl. Chem* **1967**, *15*, 539.

[101] R. F. Tuckett, *Trans. Faraday Soc.* **1944**, *40*, 448.

[102] J. D. Hoffman, *J. Appl. Polym. Sci.* **1969**, *13*, 397.

[103] F. Kremer, A. Schönhals, *Broadband Dielectric Spectroscopy*, Springer-Verlag, Berlin, Germany, **2003**.

[104] H. Watanabe, *Macromol. Rapid Commun.* **2001**, *22*, 127–175.

[105] M. Wübbenhorst, J. van Turnhout, *J. Non-Cryst. Solids* **2002**, *305*, 40.

[106] A. Mordvinkin, K. Saalwächter, *J. Chem. Phys.* **2017**, *146*, 094902.

[107] F. Vaca Chávez, K. Saalwächter, *Macromolecules* **2011**, *44*, 1549.

[108] F. Vaca Chávez, K. Saalwächter, *Macromolecules* **2011**, *44*, 1560.

[109] M. F. Brown, J. Seelig, U. Häberlen, *J. Chem. Phys.* **1979**, *70*, 5045.

[110] C. Fengler, J. Keller, K.-F. Ratzsch, G. Guthausen, M. Wilhelm, *Soft matter* **in preparation**.

[111] K.-F. Ratzsch, C. Friedrich, M. Wilhelm, *J. Rheol.* **2017**, *61*, 905.

[112] S. Nie, PhD thesis, Karlsruher Institut für Technologie (KIT), Karlsruhe, Germany, **2020**.

[113] V. Räntzsch, M. B. Özen, K.-F. Ratzsch, E. Stellamanns, M. Sprung, G. Guthausen, M. Wilhelm, *Macromol. Mater. Eng.* **2019**, *304*, 1800586.

[114] E. N. Brown, P. J. Rae, E. B. Orler, *Polymer* **2006**, *47*, 7506.

[115] J. E. Elliott, C. N. Bowman, *Macromolecules* **2002**, *35*, 7125.

[116] J. E. Elliott, M. Macdonald, J. Nie, C. N. Bowman, *Polymer* **2004**, *45*, 1503.

[117] N. Orakdogen, M. Y. Kizilay, O. Okay, *Polymer* **2005**, *46*, 11407.

[118] O. Okay, *Polymer* **1994**, *35*, 2613.

[119] V. M. Litvinov, A. A. Dias, *Macromolecules* **2001**, *34*, 4051.

[120] H. Luo, M. Klüppel, H. Schneider, *Macromolecules* **2004**, *37*, 8000.

[121] X. Guo, S. Theissen, J. Claussen, V. Hildebrand, J. Kamphus, M. Wilhelm, B. Luy, G. Guthausen, *Macromol. Chem. Phys.* **2019**, *220*, 1800350.

[122] J. Höpfner, G. Guthausen, K. Saalwächter, M. Wilhelm, *Macromolecules* **2014**, *47*, 4251.

[123] K. Saalwächter, S. Seiffert, *Soft Matter* **2018**, *14*, 1976.

[124] K. Saalwächter, *Rubber Chem. Technol.* **2012**, *85*, 350.

[125] M. Andreis, J. Liu, J. L. Koenig, *J. Polym. Sci. Part B: Polym. Phys.* **1989**, *27*, 1389.

[126] J. W. ten Brinke, V. M. Litvinov, J. E. G. J. Wijnhoven, J. W. M. Noordermeer, *Macromolecules* **2002**, *2002*, 10026.

[127] D. Moldovan, R. Fechete, D. E. Demco, E. Culea, B. Blümich, V. Herrmann, M. Heinz, *J. Magn. Reson.* **2011**, *208*, 156.

[128] M. Kelley, N. Abdol, P. Soroushian, K. Keating, A. M. Balachandra, T. Meldrum, *J. Polym. Sci.* **2020**, *58*, 616.

[129] L. A. Currie, *Anal. Chim. Acta* **1999**, *391*, 127.

[130] P. G. De Gennes, *Macromolecules* **1976**, *9*, 587.

[131] R. H. Colby, *Rheol. Acta* **2010**, *49*, 425.

[132] D. D. Jiang, G. F. Levchik, S. V. Levchik, C. Dick, J. J. Liggat, C. E. Snape, C. A. Wilkie, *Polym. Degrad. Stab.* **2000**, *68*, 75.

[133] Q. Yao, C. A. Wilkie, *Polym. Degrad. Stab.* **2000**, *69*, 287.

[134] S. Jovanović, S. Samaržija-Jovanović, G. Marković, V. Jovanović, T. Adamović, M. Marinović-Cincović, *Composites Part B* **2016**, *98*, 126.

[135] S. Habibu, N. M. Sarih, N. A. Sairi, M. Zulkifli, *R. Soc. Open Sci.* **2019**, *6*.

[136] J. M. Widmaier, G. C. Meyer, *Macromolecules* **1981**, *14*, 450.

[137] T. G. Fox, P. J. Flory, *J. Polym. Sci.* **1954**, *14*, 315.

[138] R. Bakule, J. Fähnrich, *Colloid Polym. Sci.* **1989**, *267*, 786.

[139] S. Habershon, D. E. Manolopoulos, T. E. Markland, T. F. Miller, *Annu. Rev. Phys. Chem.* **2013**, *64*, 387.

[140] R. Pasquino, T. C. Vasilakopoulos, Y. C. Jeong, H. Lee, S. Rogers, G. Sakellariou, J. Allgaier, A. Takano, A. R. Brás, T. Chang, S. Gooßen, W. Pyckhout-Hintzen, A. Wischnewski, N. Hadjichristidis, D. Richter, M. Rubinstein, D. Vlassopoulos, *ACS Macro Lett.* **2013**, *2*, 874.

[141] M. Kapnistos, M. Lang, D. Vlassopoulos, W. Pyckhout-Hintzen, D. Richter, D. Cho, T. Chang, M. Rubinstein, *Nat. Mater.* **2008**, *7*, 997.

[142] Q. Huang, J. Ahn, D. Parisi, T. Chang, O. Hassager, S. Panyukov, M. Rubinstein, D. Vlassopoulos, *Phys. Rev. Lett.* **2019**, *122*, 208001.

[143] S. P. Obukhov, M. Rubinstein, T. Duke, *Phys. Rev. Lett.* **1994**, *73*, 1263.

[144] D. Tsalikis, P. V. Alatas, L. D. Peristeras, V. G. Mavrantzas, *ACS Macro Lett.* **2018**, *7*, 916.

[145] J. D. Halverson, W. B. Lee, G. S. Grest, A. Y. Grosberg, K. Kremer, *J. Chem. Phys.* **2011**, *134*, 204904.

[146] J. D. Halverson, G. S. Grest, A. Y. Grosberg, K. Kremer, *Phys. Rev. Lett.* **2012**, *108*, 038301.

[147] J. D. Halverson, W. B. Lee, G. S. Grest, A. Y. Grosberg, K. Kremer, *J. Chem. Phys.* **2011**, *134*, 204905.

[148] M. E. Cates, J. M. Deutsch, *J. Phys.* **1986**, *47*, 2121.

[149] J. Von Seggern, S. Klotz, H. J. Cantow, *Macromolecules* **1989**, *22*, 3328.

[150] Y. Doi, K. Matsubara, Y. Ohta, T. Nakano, D. Kawaguchi, Y. Takahashi, A. Takano, Y. Matsushita, *Macromolecules* **2015**, *48*, 3140.